Hydrogen Plasma Etched Graphene Nanoribbons

Inauguraldissertation

zur

Erlangung der Würde eines Doktors der Philosophie

vorgelegt der

Philosophisch-Naturwissenschaftlichen Fakultät

der Universität Basel

von

Yemliha Bilal Kalyoncu

aus der Türkei

Basel, 2018

Genehmigt von der Philosophisch-Naturwissenschaftlichen Fakultät auf Antrag von

Prof. Dr. D. M. Zumbühl

Dr. J. Prance

Basel, den 11. December 2018

Prof. Dr. Martin Spiess

Dekan

* * *

Bu dünya soğuyacak,
Yıldızların arasında bir yıldız,
Hem de en ufacıklarından,
Mavi kadifede bir yaldız zerresi yani,
Yani, bu koskocaman dünyamız.

Bu dünya soğuyacak günün birinde,
Hatta bir buz yığını
Yahut ölü bir bulut gibi de değil,
Boş bir ceviz gibi yuvarlanacak
Zifiri karanlıkta uçsuz bucaksız.

Nazım Hikmet

* * *

This thesis is a drop in the ocean,
and every drop serves the ocean.

* * *

Abstract

Magnetic ordering in low dimensional semiconducting structures is an important element for spin-based electronics. Zigzag graphene nanoribbons which sustain ferromagnetic edge states and ordered nuclear magnetic states in GaAs 2DEGs are two such examples which represent potentials for spintronics applications. In order to be realized, both of these phenomena require certain conditions. For the magnetic ordering at the zigzag edges of graphene nanoribbons, fabrication of high quality edges is a prerequisite. Additionally, for the nuclear magnetic ordering in GaAs, the 2D system needs to reach below miliKelvin temperatures.

Here, we study hydrogen plasma etching in graphite and graphene flakes in order to fabricate graphene nanoribbons with zigzag edges. We study the distance and pressure dependence of the etching process in graphite flakes, and define two distinct plasma regimes. The *direct* plasma regime contains high density of H radicals and energetic ions, which continuously induce defects on the surface, and results in perforated surfaces. On the other hand, the *remote* plasma regime includes only H radicals, giving the opportunity to take the etching process under control to fabricate graphene structures.

The underlying substrate plays an important role in the etching process. For single layer flakes on hBN, the etching is highly anisotropic and creates hexagonal etch-pits, whereas on SiO_2, the etching is isotropic. For bilayer flakes, the process is anisotropic on both subtrates.

Atomic resolution atomic force microscopy reveals that the edges of the etched hexagons on graphite are parallel with the zigzag crystallographic direction and the absence of D-peak intensity in Raman spectra represents the high quality of the edges, since only armchair and disordered edges can result in D-peak intensity. However, for single layer samples on hBN, the high D-peak intensity shows that even tough the edges are along the zigzag direction, they are interrupted by symmetric armchair segments. Analysis on the polarization dependent Raman measurements result in the ratio of 40 % for

armchair segments along a zigzag edge.

The picture of poor quality graphene edges is further confirmed by the low temperature transport measurements. None of the features predicted for electronic band structure of zigzag graphene nanoribbons are observed in the experiments. The findings are also supported by the tight-binding simulations for a disordered zigzag edge.

In the second part of the thesis, we applied the well-established adiabatic nuclear demagnetization technique on a coulomb blockade thermometer in order to reach electron temperatures of below 1 mK. In this experiment, each measurement lead is cooled by its own nuclear refrigerator made of 2 mols of copper. The nuclei and charge carriers inside the coulomb blockade thermometer are cooled by large copper fins deposited on the chip. In order to investigate the efficiency of the process, we tested two different ramp-rates and precooling durations. Electron temperatures of 1.8 mK and 2.7 mK in the coulomb blockade thermometer are measured in two cool-downs, resulting in efficiencies of about 10 %. A simple thermal model is given in the context of the measurements considering the heat leaks and thermal dynamics within the system, also comparing the results with previous experiments.

Acknowledgement

First and foremost, I would like to thank Prof. Dominik Zumbühl for his supervision on my formidable path to obtain a PhD degree. Many thanks for giving me the opportunity and leading me through the steps of experimental physics for more than four years, resulting in this thesis at hand. His vast knowledge in physics and in experimental details, his efforts on teaching and his motivating words to solve problems in the lab had always pushed me further and are very much appreciated.

I would like to thank Dr. Jonathan Prance for joining my thesis defense committee. We are happy to have him also as our collaborator in microKelvin project. Together with Prof. Richard Haley and Alex Jones from Lancaster University, we enjoyed the scientific discussions during our visits.

It is a must to thank other scientists for helping me out at many times when I struggled in the lab. I would like to thank Dr. Christian Scheller for sharing his experience on measurements techniques, his knowledge in condensed matter systems and his time in cigarette breaks. I want to thank Dr. Mario Palma for introducing me to the project and Anssi Salmela from Bluefors for his valuable help on technical problems I have encountered working in a low temperature system.

I would like to thank Mirko Rehmann, my partner in crime in graphene project. It was a pleasure to work and find the way out together in the labyrinth of graphene nanoribbon fabrication. I am also thankful to many other PhD students from Schönenberg's group for sharing their experience with us on sample fabrication matters.

In an experimental physics lab, technical problems are part of the daily routine. I appreciate the valuable help from Sascha Martin, Patrick Stöcklin, Dominik Sifrig, Dr. Laurent Marot, Daniel Sacher, Michael Steinacher and all other personal in mechanics and electronics workshop. I am thankful to Barbara Kammermann and Astrid Kalt for their support in administrative issues.

I am happy to get to know many young scientists in the quantum coherence lab, while we enjoy and suffer from more or less the same. Lucas, Larissa, Dorothée, Pirmin, Dario, Mirko, Florian, Leon, Taras, Luiqi, Kris, Tim, Fabian Müller and many others who pass by the lab for a short while, I enjoyed the time we spent in and outside of the lab. I also want to thank Alice and Bob, for supplying the necessary green environment around my desk to make it a liveable corner in the office.

Thank you very much to the other young physicists, with whom I enjoyed to spend time on non-physics matters. It was a pleasure to enjoy the life in Switzerland together with Ehud Amitai, Tibor Sekara, Marcel Serina, Christoph Orth and Zakaria Azdad. I wish you the best of all for the rest of your lives.

In life, there are certain kinds of couplings and interactions, the strengths of which are independent of the distance. No words are enough to thank my family for their endless support and trust. Last but not least, I have to thank my ex-girlfriend, now my wife, for supervising me on emotional matters of this universe. Thank you Irem, for enjoying and fighting the life together with me.

Contents

1 Introduction

1.1 From compasses to spintronics: *From lodestones to spin-qubits*

Magnetism is a phenomenon which is known to mankind since ancient times. It was discovered when people noticed that iron is attracted by *lodestone*, which was actually Fe_3O_4, magnetite, a naturally occurring magnet. Around the third century BC, this knowledge was utilized to develop a device called the *compass*, where it was realized that a magnetic needle would *magically* point North. Only after the 10^{th} century, was it described with a scientific attitude, and it was concluded that the Earth itself must also be a magnet [1] .

In the beginning of 19^{th} century, the great scientists Ampère, Gauss, Faraday et al. have investigated this phenomenon and described the laws governing its dynamics and natural link to electricity. Then Maxwell compiled all these laws into one complete theory and therein explained a detailed mathematical formalism which are known as Maxwell's equations today [2].

Maxwell's equations described the nature of electromagnetism completely and even extended further to say that light is an electromagnetic wave. Moreover, the equations implicitly included the constancy of the speed of light. Soon after that, the science had a paradigm shift with the introduction of Einstein's special relativity [3]. Together with quantum mechanics, these two theories were highly influential for the understanding of the fundamental nature of *things*.

While it is beyond these introductory pages to explain their tremendous effects, one important aspect we learned from quantum mechanics is that *things* behave differently if we look at them at the level of elementary particles. This naturally imposed a distinction between microscopic and macroscopic worlds and motivated the research to understand the link between. Thus, we learned that some observable phenomena that

we know from the macroscopic world stem from the collective behaviour of particles belonging to -and ruled by- the microscopic world, such as the relation of bulk magnetism to magnetic moments of elementary particles.

The magnetic moment of an elementary particle is related to its intrinsic angular momentum. Just like a charged object which spins around its own axis has an angular momentum and behaves like a magnetic dipole, the elementary particles also show the same magnetic behaviour even tough they do not physically spin. This intrinsic angular momentum is called *spin* and it plays a key role in the interaction of particles with each other and with external electromagnetic fields. These interactions determine the conditions for magnetically ordered states in condensed matter systems.

Just like ancient people who utilized a magnetic needle as a compass, the same mindset still persists today in order to transfer knowledge to practical purposes. One of the exciting fields of condensed matter physics today is called *spintronics*, which studies and aims to exploit spin properties of electrons in order to improve the efficiency of technological devices and/or develop new functionalities, which are otherwise not possible if only the charge property of electrons is made use of [4].

Spintronics is a very wide area of research. At one end it intends to control and manipulate a single spin for, for example, *spin-based quantum computing* and, on the other, extends to development of nanoscale and microscale components such as a *spin transistor* to be used in spintronic devices, which, in the near future, would possibly replace the current electronics technology [5].

The current commercial semiconductor industry is based on the charge of the electron where, charge current and its interaction with electromagnetic fields are employed in sourcing, detecting, transporting and manipulating the state of a device. As a landmark, transistors are the basis of today's modern technology leading to smart devices in everybody's pocket with tremendous capabilities. The field of spintronics is now in search for the most efficient materials and methods to replace the above mentioned electronic components with their spintronic counterparts. Spin injection

and detection, spin transport, spin valves and spin filters can be counted as some example concepts to be used in a macroscopic spin system [4].

1.2 Zigzag-edged graphene nanoribbons

In the quest of finding materials for future technological devices, graphene, the two dimensional form of carbon atoms, has attracted much interest since it was first exfoliated as a single layer on top of a substrate and quantum transport measurements were performed on it [6].

It is a one of a kind material not only for applications in technology but also for the observation of some phenomena, which can not be observed in conventional semiconductors. Gate tunability of charge carriers and charge carriers behaving as massless Dirac fermions are two attractive properties [7]. Additionally, it is one of the strongest materials, while still being flexible and light, and it has been shown that it can have very high mobilities at room temperature [8]. Recent research carried out has demonstrated that superconductivity occurs at twisted bilayer graphene and this has further marked the interest in graphene due to its peculiarities [9].

Still, some issues are present when it comes to applicability. Even though it is a device in which you can tune the charge carrier density by gating, it is a zero-gap semiconductor, which means that it does not have a band-gap. Moreover, Klein tunnelling allows charge carriers to tunnel through potential barriers with an amplitude proportional to barrier height [10]. So it is impossible to use it as a transistor or form quantum dots and constrictions via methods applied in conventional semiconductors.

Nevertheless, graphene proves itself to be interesting again. Forming nanoribbons in a single graphene sheet alters its electronic band structure and opens a band gap inversely proportional to the ribbon's width due to lateral confinement [11]. Further alteration of electronic band structure occurs if the edges of a ribbon can be made along particular crystallographic directions, namely zigzag and armchair. For the zigzag case, the low

temperature ground state of the electronic structure supports magnetically ordered localized edge states, which are in antiferromagnetic orientation at opposite edges [12]. Combined with a band-gap, high mobility and external electromagnetic fields, zigzag edged graphene nanoribbons are strong candidates for spintronic devices [13].

The drawback to this scheme is that the band structure is highly vulnerable to disorder, which enforces the need to fabricate graphene nanoribbons with perfect zigzag edges. Numerous methods have been proposed and investigated in the last 10 years and fabrication of such nanostructures have been proven to be a great challenge [14]. In the first part of this thesis, a remote hydrogen plasma etching method is investigated. The interaction of hydrogen plasma particles on graphite surfaces has been known to create hexagonal etch-pits since 1970 [15]. After single layer graphene came into play in quantum transport experiments, and the necessity of producing high quality zigzag edge graphene ribbons appeared, anisotropic etching methods have drawn interest again, since the process naturally selects a crystallographic direction. This is highly beneficial because it allows control of the edges of a ribbon on nanometer scale depending only on a few parameters of the plasma which are convenient to control, such as power, pressure and temperature. Chapter 3 explains a study where optimum etching parameters are determined in single layer graphene flakes on insulating substrates. In Chapter 4, the quality of the etched edges and nanoribbons created with hydrogen plasma are examined via Raman microscopy and quantum transport measurements.

1.3 Adiabatic nuclear demagnetization

The other extreme of spintronics deals with manipulating a single spin for the ultimate goal of realizing *spin-based quantum computing*; an invention which holds the promise to reshape the future of mankind [16]. An incredible amount of effort and resources are being invested in this research since *a quantum computer* will consist of many units, each of which require high expertise to be designed, developed and operated. Owing to the ability of fast operation, high fidelity and the level of development of

the semiconductor industry, one of the most promising schemes is to utilize spins of electrons in semiconductor quantum dots to form the basic operational unit called a quantum bit - qubit [17–19].

In this scheme, one needs to form, manipulate and conserve the state of the spin in a quantum dot for a finite amount of time, called the coherence time. In a semiconductor where a quantum dot resides, there exist certain mechanisms, which relax the electron spin, such as scattering, spin-orbit interaction and hyperfine interaction. For longer coherence times, these interactions must be suppressed to a certain degree.

One way to increase the coherence is to weaken the coupling of nuclear spins to the electron spin via nuclear spin polarization, provided that a quantum dot can be formed in such a system where more than 99% of nuclear spins are polarized. An intrinsic polarization of nuclear spins in a GaAs 2DEG can be hosted due to a magnetic phase transition which occurs at ultra low temperatures [20]. This nuclear spin temperature which imposes a nuclear ferromagnetism is predicted to be around 1 mK [21]. Even though not yet achieved in a 2D electron system, evidence for a helical nuclear spin order in a 1D system has been shown around 100 mK, due to that in a one-dimensional system, the electron-electron interaction effects are much more pronounced, leading to a much higher ordering temperature compared to two dimensional systems. [22, 23].

Reaching down to -and below- the mK regime in a nanoscale condensed matter system requires many obstacles to be overcome, due to several reasons regarding the weakening of heat transport at low temperatures, heat leaks from the environment and the sources of cooling power. Today, it is easily possible to reach 5 mK, and even slightly lower temperatures with commercially available dilution refrigerators (DR) [24]. However, it is another issue for a nanoelectronic device to be well-thermalized with a DR in a cryostat, leading to warmer electron temperatures in the device to be measured.

Another well established method is called magnetic refrigeration which uses magnetic disorder entropy of magnetic moments for cooling [25]. More specifically, it is possible to cool nuclei and, in turn, conduction electrons in a metal by adiabatically demagnetizing

the nuclear spin bath. This method, which is called *adiabatic nuclear demagnetization* (AND), was first applied in 1956 by Kurti et al., and nuclear temperatures of 20 μK were reached [26, 27]. A milestone in the history of adibatic nuclear demagnetization is the work by Berglund et al. where the nuclear refrigeration technique is combined with a dilution refrigerator and a superconducting magnet [28]. As a result, conduction electron temperatures of 0.37 mK were reached in a copper nuclear refrigerant.

An advantage of this technique is the possibility of incorporating the nuclear refrigerant on the same chip of a nanoelectronic device, where the quantum transport measurements are performed, which is much more efficient than a dilution refrigerator can manage. Still, the question arises about how to measure the temperature of electrons accurately without using an external thermometer. This can be achieved with a Coulomb blockade thermometer (CBT) where the transport characteristics of the normal metal-insulator-normal metal tunnel junctions are temperature dependent [29, 30].

The lowest electron temperature in a condensed matter system was achieved in this way by on-and-off chip magnetic refrigeration of a CBT in a dry crysotat. The recorded temperature by M. Palma and C. Scheller et al. was 2.8 mK and stands as the currently reported world record [31]. In Chapter 5, CBT experiments will be discussed in a similar fashion where the effect of different experimental parameters and possible limitations are investigated and electron temperatures of 1.8 mK are reached.

1.4 Thesis Outline

This thesis is comprised of two branches of experiments for the purpose of achieving magnetically ordered states in condensed matter systems. The first part is about fabrication and characterization of zigzag-edged graphene nanoribbons. In the second part, adiabatic nuclear demagnetization experiments will be carried out in order to obtain ultra-low electron temperatures in a nanoelectronic device.

Chapter 2 introduces the necessary background information for the experiments carried

out in the main chapters. General properties of graphene nanoribbons, their fabrication methods, corresponding characteristics and Raman spectroscopy in graphene will be explained. Then, the principle of adiabatic nuclear demagnetization and possible heat sources will be given.

Chapter 3 presents a hydrogen plasma etching technique in graphene and graphite, which creates hexagonal-shaped etch pits with edges along the zigzag direction. Two distinct plasma regimes are defined and the subtrate dependence of the etching process will be examined.

Chapter 4 is the exploration of the quality of graphene edges defined with hydrogen plasma etching via atomic resolution atomic force microscopy, raman microscopy, and low temperature transport measurements.

Chapter 5 deals with adiabatic nuclear demagnetization experiments in a CBT. The cryo-free refrigerator and the working principle of the CBTs will be briefly explained. Comparison of three cool-downs with different ramp-rates and precooling durations will be presented in order to understand the effect of these experimental parameters on the efficiency of the AND process. Also, possible limitations that prevent reaching lower temperatures will be discussed.

Chapter 6 is the conclusion of this thesis, where the main results are recapped and an outlook on future experiments will be given.

2 Theoretical and Experimental Background

The general physics behind the experiments conducted for this thesis have been well known to the scientific community and also explained in many books and review papers[11, 12, 14, 25, 32] . In this chapter, the phenomena related to our specific experiments will be explained and laying the basis for understanding further experiments in the later chapters. First, graphene nanoribbons, their edge-related electronic properties and fabrication methods will be briefly explained. Since Raman microscopy is an important tool for our experiments, it is also necessary to describe the Raman spectrum of Graphene and its interaction with the edges. Finally, basic physical principles of ultra-low temperature experiments will be summarized.

2.1 Graphene: *Theoretical Perspective*

In graphene, carbon atoms are arranged in a hexagonal lattice structure which can also be seen as two triangular lattices interpenetrating each other, see Figure 2.1. These triangular lattices make up two sublattices A and B and they are responsible for peculiar phenomena [11].

In monolayer graphene, three of the electrons hybridize as sp^2 and create covalent σ

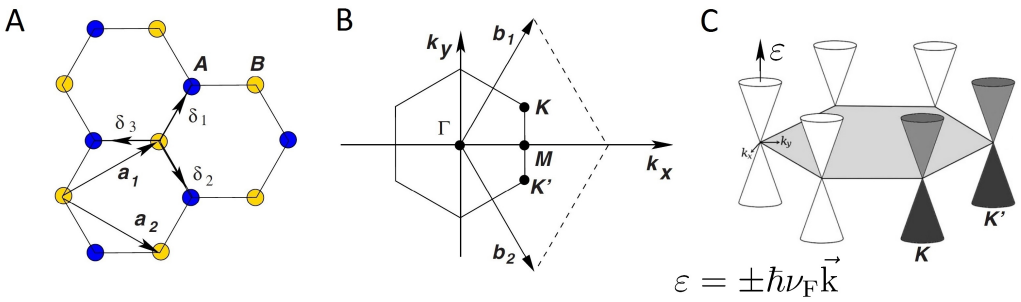

Figure 2.1: A) Hexagonal real lattice structure of graphene, consisting of two sublattices with atoms A and B, as coloured blue and yellow. This hexagonal lattice structure can be viewed as a combination of two triangular lattices. a_i show the unit lattice vectors and δ_i are nearest neighbour vectors. B) Brillouin zone of graphene is depicted with **K** and **K′** as being two unequal valleys. b_i are the unit reciprocal lattice vectors. C) Low energy linear dispersion relation is shown at six Dirac points. Figure adapted from [33].

bonds, making graphene mechanically a very strong 2D material [8]. The fourth electron forms the $2p_z$ orbital perpendicular to the graphene plane. This orbital creates the so called π bands and is in charge of the electrical conductivity of graphene. The electronic dispersion relation of graphene is calculated with tight-binding approximations based on these π-states. The conduction and valence bands touch each other at six Dirac points, corresponding to the six corners of the Brillouin Zone. Out of six, two inequivalent sets of three Dirac points are labelled as $\mathbf{K}$ and $\mathbf{K}'$, giving rise to valley degeneracy of 2. For small energies, the dispersion relation is linear in momentum, $\varepsilon = \pm\hbar\nu_F\vec{k}$, meaning that charge carriers move at constant speed around these points, given by the Fermi velocity $\nu_F \approx c/300$. The electron dynamics in graphene is thus effectively relativistic such that the linear dispersion relation can well be described by Dirac equation for massless Dirac fermions. This implies that the effective mass of the charge carriers in this region is zero.

In undoped graphene, the Fermi energy lies at the Dirac point, namely at the charge neutrality point (CNP). This makes graphene known as a zero-gap semiconductor. A novel property of graphene stemming from two equal sublattices A and B is a pseudo-spin number in addition to spin and orbital quantum numbers. Due to this pseudo-spin number, the charge carriers at two linear branches of energy dispersion (right-moving and left-moving particles) acquire a different chirality and become independent of each other.

2.1.1 Graphene Nanoribbons

The graphene hexagonal lattice has two crystallographic directions, known as armchair (AC) and zigzag (ZZ). Graphene Nanoribbons (GNRs) created with armchair and zigzag edge termination have different characteristics in their electronic structure depending on the edge type and width of the ribbon. Tight-binding calculations show that ribbons with armchair termination have gapped semiconducting or gapless metallic behaviour, alternating with increasing width [34–38]. Within the same model, metallic

behaviour is predicted for all zigzag ribbons with almost flat bands extending over one third of the 1D Brillouin zone at the Fermi energy, see Figure 2.2. These bands get flatter and flatter as the width of the ribbon increases. These dispersionless states are localized at the zigzag edges and decay very quickly into the bulk of the ribbon.

The origin of this difference in band structure is related to two sublattices forming the graphene lattice. For armchair ribbons, the atoms sitting at one edge belong to both sublattices A and B, whereas in zigzag ribbons one edge consists of atoms belonging to only one sublattice and the opposite edge atoms belong to the other. This means that wavefunctions for both sublattices must vanish at both edges for armchair ribbon. On the other hand, at opposite edges of the zigzag ribbon sublattice A and B have non-vanishing solutions.

As discussed previously, a band-gap is a key element for graphene nanoribbon based electronics and spintronics. For semiconducting AC-GNRs, a gap opens due to the con-

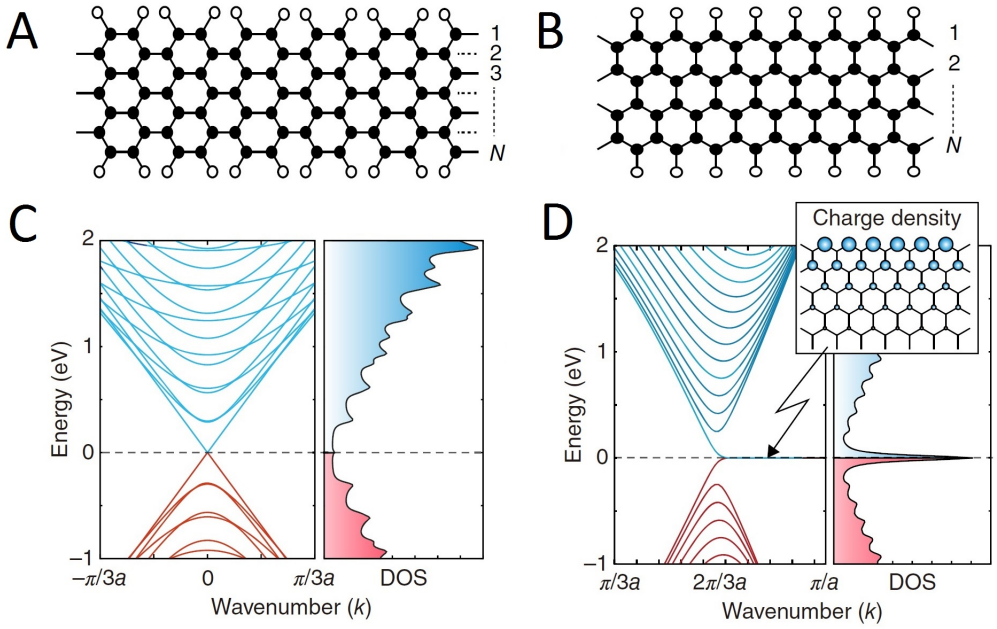

Figure 2.2: Structure of a A) metallic armchair and B) zigzag nanoribbon with N, defining the number of atoms across the ribbon. Black atoms are carbon and white are neutral hydrogen atoms terminating the dangling bonds. Energy band structure and corresponding density of states for a metallic armchair ribbon and for a zigzag ribbon is shown in C) and D), respectively. The high density of states at the Fermi energy corresponds to localized charge density at the edges of the zigzag ribbon in real space, as depicted in the inset. Here, blue and red regions correspond to conduction and valence electrons. Figure adapted from [39].

finement potential where the energy of the splitting decreases with increasing width [13, 34–38, 40]. In ZZ-GNRs, band gap originates from staggered sublattice potential due to spin ordered states at the edges [40]. Besides, as a result of the one dimensional confinement, the transverse modes of the ribbon are quantized and conductance quantization is expected for GNRs with crystallographic edges [41]. For AC-GNRs, valley degeneracy is lifted due to the intervalley mixing at the edges and steps of $2\,e^2/h$ are predicted. For ZZ-GNRs, both spin and valley degeneracy is maintained and steps of $4\,e^2/h$ are anticipated [36, 42].

The peculiar property of ZZ-GNRs is the magnetic ordering at the edges. The flat bands at the fermi energy give rise to a high density of states. Upon inclusion of spin degrees of freedom in the mean-field Hubbard model, ferromagnetic ordering of electron spins at opposite edges of the zigzag ribbon with anti-parallel orientation is predicted [13, 40, 43, 44]. The magnitude of the antiferromagnetic ordering scales inversely with the square of the ribbon width [45]. When electron-electron interactions are also introduced, a band gap opens at the flat-band region as shown in Figure 2.3. For high doping levels, magnetism is no longer maintained since the Fermi level is tuned away from the flat band region [12, 45].

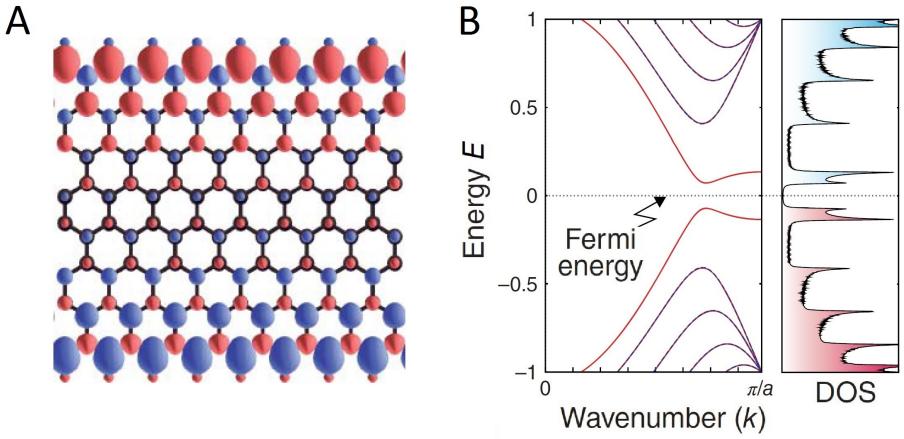

Figure 2.3: A) Schematic magnetic structure of a zigzag ribbon showing two opposite magnetic moments, red and blue, at pooposite edges. B) Electronic band structure and corresponding density of states of a zigzag ribbon calculated in mean-field Hubbard model with certain on-site Coulomb repulsion potential. The gap opening at Fermi level is due to the electron-electron interactions. Figure adapted from [39].

2.1.2 Graphene Nanoribbons with Edge Disorder

All the above theoretical predictions are based on perfect crystallographic edges with no disorder and the dangling bonds of the edge atoms being terminated by neutral hydrogen atoms. To date, only few experiments have given hints of perfect ZZ or AC-GNR features since fabricating ribbons with perfect edges proved to be highly challenging, as will be explained in detail in the next section.

Theoretical studies show that edge roughness has a significant effect on the edge states of nanoribbons, resulting in the collapse of the above-mentioned electronic properties predicted for perfect-edge ribbons. Conductance for non-perfect edges is suppressed due to several reasons and quantization of conductance disappears due to loss of ballisticity [46, 48–50].

The edge roughness decreases the number of conductance channels at the edge and localizes charge carriers at the edge [50]. Depending on the total width and penetration of roughness into the bulk of the ribbon, this can lead to formation of quantum dots and observation of coulomb blockade, as illustrated in Figure 2.4 [46]. Also, edge defects act as random scatterers and enhance the backscattering at the edges, leading to Anderson

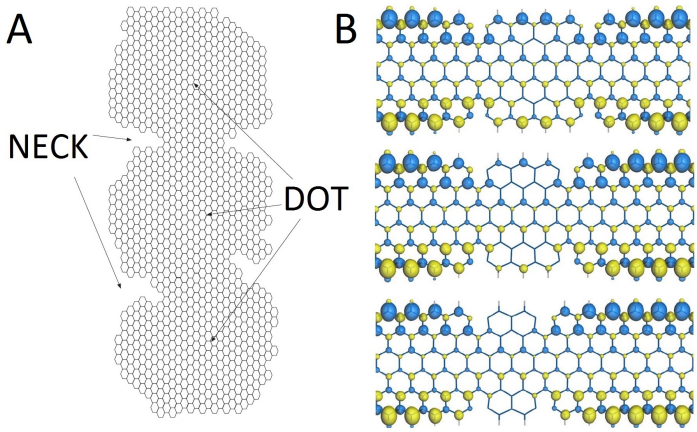

Figure 2.4: A) Sketch of a GNR with deep vacant edge sites, leading to necks and formation of dots along the ribbon, taken from [46] B) DFT simulation of the suppression of magnetic moments localized at the edges of a zigzag ribbon with vacant sites. From top to bottom, vacant sites get closer to each other, similar to increasing edge disorder. Figure taken from [47].

localization if the nanoribbon is longer than the localization length [50]. Moreover, the disordered edges will lead to loss of localized magnetic moments at the edges of a zigzag ribbon because vacancies and impurities at the edge would not contribute to the density of states at Fermi energy [47]. It should be noted that the effect of edge roughness in conductance is edge-type and width dependent as well as being correlated with the existence of a intrinsic band gap or a transport gap. For example, conductance suppression should be weaker in wider ribbons for the same edge disorder density [50].

There are several studies where edge states are predicted to be robust under some specific conditions. For example, ballisticity could be maintained for low edge disorder [48]. In case of a ZZ-GNR, edge states can survive when the width changes slowly with step-edges where zigzag edge is interrupted with armchair segments [34]. For semiconducting AC ribbons, electronic states are predicted to be robust against edge-disorder for low energies [51].

Other than edge disorder, bulk disorder, substrate dependent varying potentials (electron-hole puddles) and edge passivation can suppress the conductance in edge channels [48, 52]. The dangling bonds of the Carbon atoms located at the edge can be passivated with atoms or molecules other than Hydrogen (especially due to the chemicals involved in the sample fabrication environment). Any non-neutral edge passivation, again, results in modification of electronic structure at the edge [49].

2.2 GNRs in Experiment: *Fabrication, Edge Character and Electronic Structure*

Since single layer graphene became available for physics experiments, many physical phenomena have been tested and graphene nanoribbon devices in various structures have been proposed. Alas, the fabrication of graphene nanoribbons with atomic scale ordered edges has been proven to be extremely challenging. Throughout the years many different approaches have been presented and investigated.

There are two distinct groups of GNR fabrication, top-down and bottom-up approaches. In a top-down approach, the GNR device is simply cut or shaped in a larger graphene sheet via etching. Oppositely, in bottom-up approaches, GNRs or nanostructures are grown atom by atom via deposition or molecular assembly. Each group has various different methods to produce such ribbons. As a result, GNRs produced with different methods resulted with qualitative differences in their electronic properties and edge configuration. While some of them are successful in producing highly ordered edges but poor in electronic quality and practicality, some others are much more practical to implement as nano devices but poor in producing atomically perfect edges. This section summarizes major methods of GNR fabrication, their characteristics and performance so far. It is important to see the state of the art, so we can place our H-plasma method in full picture and compare its advantages and disadvantages.

2.2.1 Lithographical Methods

The most used top-down approach to fabricate graphene nanoribbons is to use an etch-mask to define the geometry of the device and expose the sample to Ar/O_2 plasma to etch away the unprotected graphene regions. The easiest etch-mask is by using a PMMA polymer and then shape the mask with e-beam lithography. This method allows precise control of geometrical shapes down to about 20 nm. Some other methods that have been used as an etch-mask are silicon nanowires [53], PS-PDMS copolymer films [54], meniscus-mask [55], etc. Since all these methods have their own limitations, PMMA masks are the most accepted method for top-down processes.

The biggest drawbacks of Ar/O_2 plasma etching are the poor edge-quality and the fact that the process is not anisotropic. During the etching process, the bombardment of energetic particles from the plasma breaks the chemical bonds, dissociates atoms in any direction and creates rough edges. Graphene nanoribbons created with disordered edges with this method have been investigated and laid the basis for understanding

the transport properties of such devices.

As explained by theory, the nanoribbons are supposed to show intrinsic energy gaps around the charge neutrality point which scales inversely with the width due to confinement (namely, confinement gap). However in reality, the observed suppressed conductance (transport gap) was usually larger than anticipated intrinsic confinement gap and included sharp conductance resonances, as shown in Figure 2.5 A [56–58]. These resonances occurred at low temperatures due to the charge transport between localized states which dominate the density of states around CNP [59–61]. Moreover, this transport gap was observed to shift or change size after annealing of sample at high temperatures. This pointed out that the localized states are due to the doping of GNR and disorder due to charged impurities [57].

Combined with the confinement gap, the charged impurities which are spread over the graphene sheet create an inhomogeneous potential landscape and in turn form a series of quantum dots (localized states) along the ribbon, as depicted in Figure 2.5 B. The resonances inside the gap can be explained by tunnelling through these quantum

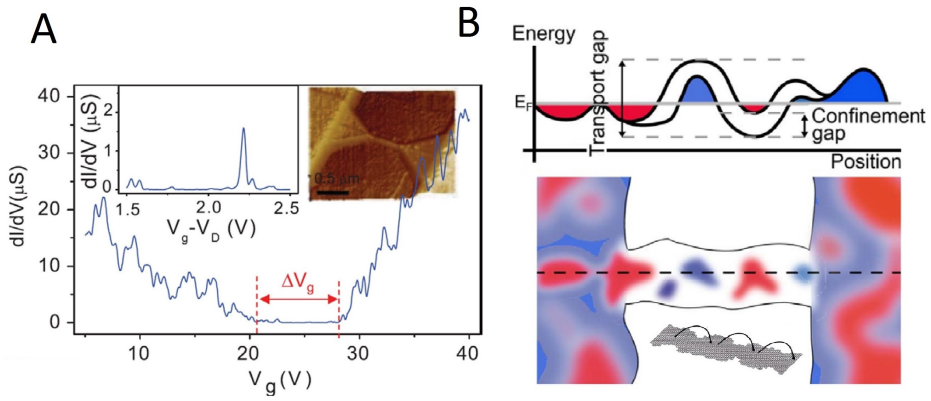

Figure 2.5: A) Conductance mesaurement near the charge neutrality point showing the transport gap region. Left inset is the zoom-in of the gap region, clearly showing the conductance peaks. Right inset is the AFM image of the measured single layer graphene on SiO_2 device. Figure taken from [56]. B) Sketch of the band structure of a graphene nanoribbon with disordered edges with respect to position at the top and corresponding charge map on lateral plane. Here red regions correspond to hole doped and blue regions correspond to electron doped regions. Conduction and valence band edges shift in energy, creating electron and hole doped islands along the ribbon, like multiple quantum dots. Charge carriers can hop from one region to another at certain energies and also due to Klein tunneling. Figure taken from [57].

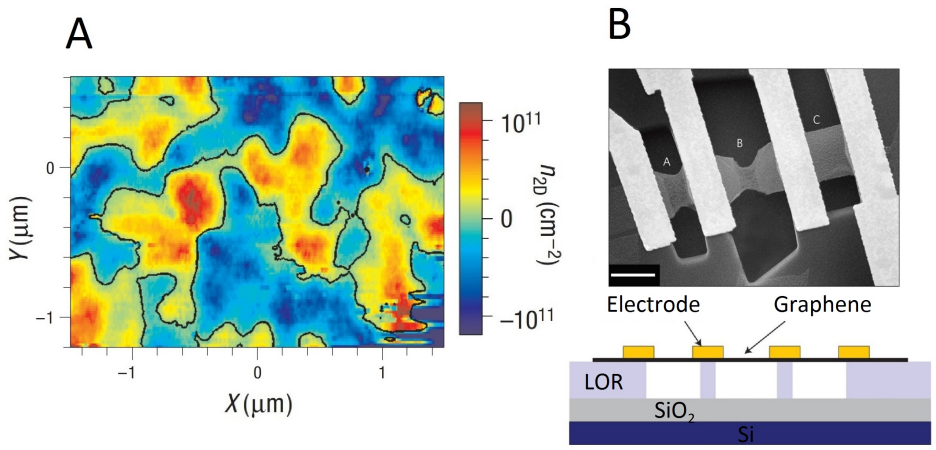

Figure 2.6: A) Colour map of spatial charge density variations in the graphene supported on SiO_2. Red regions correspond to electrons and blue regions to holes. Figure taken from [52]. B) SEM image of suspended graphene ribbons, about 1μm above SiO_2 substrate and the schematic of the suspended structure. As seen, the ribbon is strongly deformed after current annealing, creating a narrow constriction in section B, rather than a long parallel edged ribbon. Scale bar is $2\mu m$. Figure taken from [62].

dots. The same mechanism is also responsible for the observation of Coulomb blockade diamonds of multiple quantum dots [56–58, 63]. An important experiment was done by Martin et al., in which they imaged the charge puddles in graphene on SiO_2 substrate by using a scanning electron transistor, shown in Figure 2.6 A [52]. This experiment pointed out the effect of the substrate on the transport properties of graphene sheets.

One alternative way to overcome the charge inhomogeneities due to the substrate is to suspend the sample, depicted in Figure 2.6 B. After current annealing, this enabled reaching mobilities of $200'000\,\mathrm{cm}^2/(\mathrm{Vs})$ [64] and also observation of quantized conductance [62].

Other than charge-hole puddles, SiO_2 substrates presented other limitations on the electronic quality of graphene due the charged surface states and impurities [65], substrate surface roughness [66, 67] and surface optical phonons [68, 69]. To overcome these issues, Dean et al. proposed to use hexagonal Boron Nitride (hBN) as an underlying dielectric substrate [70]. hBN is an insulating isomorph of graphene lattice structure with a small (1.7 %) lattice mismatch [71]. It is relatively inert and expected to be free of surface charge traps and also has been shown to conform to both corru-

gated and flat substrates [66, 72]. Moreover, the single crystal pieces of hBN can easily be grown and transferred. Since the discovery of its advantages, hBN is the choice of material as an insulating substrate for almost all graphene devices.

hBN can also be easily exfoliated like graphene flakes and it allows patterning of graphene device structures with lithographical methods. Graphene nanoribbons on hBN substrates were fabricated with oxygen plasma and showed mobilities of around $50'000\,\mathrm{cm}^2/(\mathrm{Vs})$ [74]. Lately, hBN has started to be used as a caping layer to protect the graphene layer from fabrication residues of further processes, shown in Figure 2.7 [73], which even improved the device performances, allowing the mobilitiy of $150'000\,\mathrm{cm}^2/(\mathrm{Vs})$ for point-like constriction samples [75] and on the order of $10^6\,\mathrm{cm}^2/(\mathrm{Vs})$ for 2D device structures [76, 77]. Even though one could produce GNRs with various dimensions easily with lithography, the field of research is still seeking to produce ribbons with edges along crystallographic directions and with much less disorder to exploit the peculiar properties of ZZ and AC ribbons.

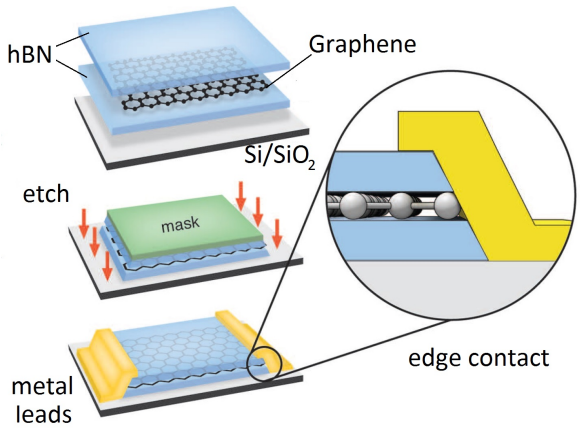

Figure 2.7: Schematic of monolayer graphene encapsulation. As a first step of fabrication, graphene is encapsulated between two thin hBN layers by dry pick-up method. Then the etching mask is employed via e-beam lithography to shape the flake as desired. Plasma etching is also employed to etch trenches to further deposit metal for 1D etch contacts. Figure taken from [73].

2.2.2 Sonication of Intercalated Graphene

One of the first chemical approaches to obtain narrow graphene nanoribbons is based on sonication [78]. In this method, commercial expandable graphite is exfoliated by a rapid temperature increase up to 1000 °C in forming gas. When heated, the intercalation compounds which were synthetically absorbed into graphite layers decompose into gas particles and create an inter-layer pressure to push apart graphite planes in c axis direction. As a result, a huge volume expansion is observed, see Figure 2.8 A. The material is then dispersed in an appropriate solution with specific chemical agents to be sonicated and form into small flakes. After that, bulk graphite pieces are removed by centrifugation. Finally, GNRs are carefully transferred on suitable subtrates such as SiO_2 for further characterization, as shown in Figure 2.8 C. This method produces large amount of graphene flakes including GNRs with often narrow (<10 nm to ∼50 nm and long (up to 1 μm) dimensions.

It turned out that this method produces flakes with one to few layers, determined by atomic force microscopy mesaurements. Even though this method suggests very smooth edges [78], non-perfect edges with mixture of zigzag and armchair segments is evidenced

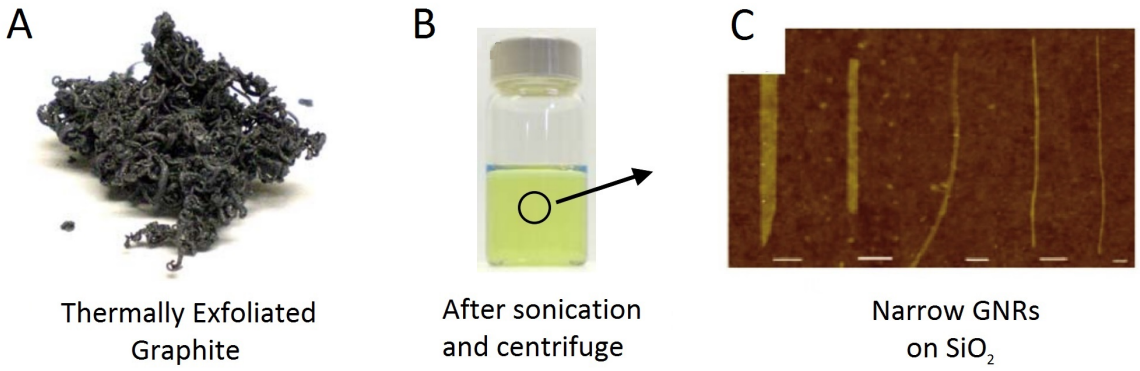

Figure 2.8: Main steps of fabricating GNRs by sonication. A) Commercial expandable graphite is exfolited thermally at 1000 °C and then dispersed in appropriate solution for sonicaiton. Sonication creates a homogenous solution with many graphite and graphene pieces. B) Centrifugion helps to eliminate big graphite pieces and form a solution with thin graphene layers. C) AFM images of sonicated GNRs, transfered on SiO_2 substrate. All scale bars are 100nm. As seen, the ribbons show very smooth edges, however they are shown to be chiral rather than zigzag or amrchair. Figure adapted from [78].

in electronic measurements [79, 80]. The narrow (<10nm) GNRs show semiconducting behaviour at room temperature, whereas wider ribbons showed metallic behaviour without a gap [79]. Even though the quality of these ribbons can be improved by high temperature annealing in inert atmospheres, low mobilities around $100 - 200\,\mathrm{cm}^2/(\mathrm{Vs})$ are measured for narrow ribbons indicating low performance as a field effect transistor, possibly due to the residues of chemicals used in the process of fabrication.

2.2.3 Carbon Nanotube Unzipping

Carbon nanotube unzipping is intensely studied to form one or few layer graphene nanoribbons from unzipping single wall or multiwall carbon nanotubes (CNTs) by solution based oxidation [81], immersing in PMMA with controlled etching [82], sonication [83], using cobalt or nickel particles as precursors [84] and partly unzipping with Zn sputtering [85]. This method can be applied to both single wall and multi CNTs, forming single layer and multilayer GNRs, respectively, depicted in Figure 2.9.

Even though unzipping CNT results in GNRs with very smooth edges, the edges are shown to be chiral rather than perfect ZZ or AC by Raman [82, 83, 85], STM and STS measurements [86]. Electronic transport measurements on substrate [82, 83, 87, 88] and on suspended samples [89, 90] also did not show features of electronic band structures of ZZ or AC edges.

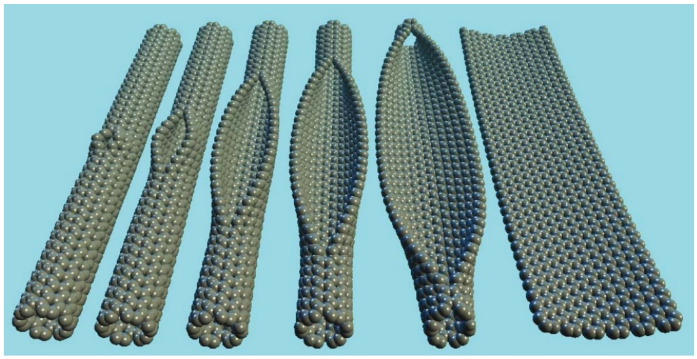

Figure 2.9: Schematic of carbon nanotube unzipping process, forming a perfect zigzag edge graphene nanoribbon from a single-wall carbon nanotube. Figure adapted from [81].

This method showed comparable electronic quality to lithographically fabricated rib-

bons. Quantum dot formation and coulomb blockade have also been observed and mobilities up to $2'000\,\mathrm{cm}^2/(\mathrm{Vs})$ are measured [91, 92]. Experiments also pointed out that unzipping method needs to be improved further for better performance since it includes many chemicals during the process, which would cause surface adsorbtion and edge functionalization, resulting in quality degradation [87, 92].

2.2.4 Bottom up Fabrication from Molecular growth

One important bottom-up fabrication method of producing graphene nanoribbons with atomically precise edge structures is by molecular assembly. This approach is proposed by surface-assisted polymerization and subsequent cyclization of suitably designed molecular precursors [93–96]. In this method, the synthesized GNR structure is atomically well-defined as revealed by STM images and the topology is fully determined by the precursors. It is possible to produce few nanometer straight armchair [93] and zigzag [94, 97] nanoribbons, as shown in Figure 2.10.

STS measurements of these devices report band gaps of 2.3 eV for N=7 AC-GNR [94] and 1.9 eV for the energy splittings of edge states of a N=6 Z-GNR transferred on NaCl substrates [96]. The non-triviality of this process is to produce or transfer GNRs onto

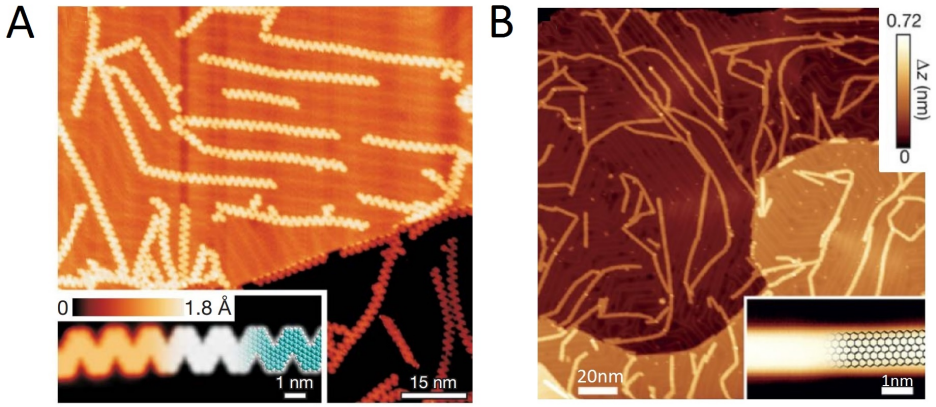

Figure 2.10: A) STM image of chevron-type GNRs fabricated on a Au(111) surface. Inset shows the high-resolution STM image and a DFT-based simulation overlaid with molecular model of the ribbon (blue, carbon; white, hydrogen). Figure adapted from [93]. B) Large-scale STM image of zigzag edged GNRs on Au(111) surface after annealing at 625 K. Inset shows high-resolution STM of a 6-ZGNR, with the superimposed structural model. Figure adapted from [97].

an insulating substrate. The molecular assembly mechanism works only on catalytic surfaces such as Au(111) and Ag(111) and the strong electronic coupling between the ribbons and the metal surface obscures the detection of the electronic edge states. Therefore the technological use of this fabrication method faces some challenges, such as contacting the short ribbons via metal deposition for transport measurements or its extension to substrates that are technologically relevant. Methods to transfer intact GNRs from gold films onto suitable substrates are still under investigation.

Another noteworthy molecular bottom-up chemical synthesis has also been reported to produce GNRs encapsulated in single-walled carbon nanotubes by confined polymerization [98]. Analysis of the HRTEM images showed that the nanoribbons were often nonuniform in the width with a visible variation in the range of few nanometers. The geometrical shape turned out to be complicated such that the ribbons were observed to twist and form helical configurations. If further investigated and improved, perfect edge GNRs encapsulated by single wall nanotubes would be useful for certain spintronics applications.

2.2.5 Epitaxial Growth on SiC Step Edge

Sprinkle et al. developed a patterned growth of GNRs based on both lithography and epitaxial growth on SiC subtrates [99, 100]. When heated in vacuum or in an inert atmosphere, SiC decomposes by silicon sublimation and the remaining carbon atoms rearrange as a graphene layer. By etching trenches on the surface of SiC, one can let graphene layers grow only on those etched facets, which also determines the width of the grown ribbon, see Figure 2.11. One can fabricate GNRs as narrow as 40 nm, determined by trench depth. The first example devices created with this method showed room temperature mobilities up to $2'700\,\mathrm{cm}^2/\mathrm{Vs}$ and demonstrated scalability by fabricating $10'000$ top gated graphene transistors on a SiC chip [100]. Mobilities on the order of $10^6\,\mathrm{cm}^2/(\mathrm{Vs})$ have been reported for 40 nm wide ribbons, which presented this technique as a valuable and promising one to be improved compared to the other

methods [101, 102].

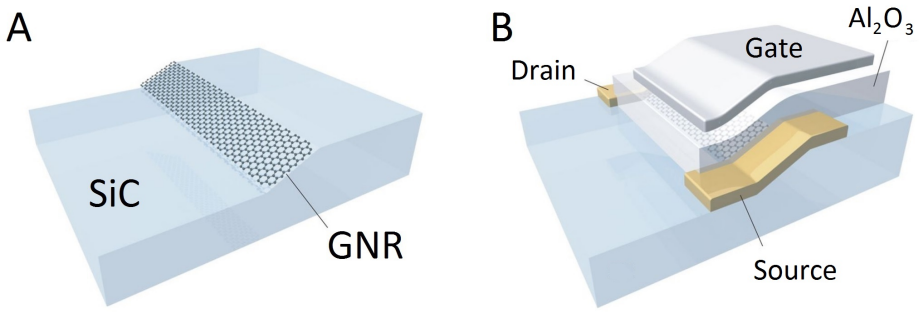

Figure 2.11: A) Self-organized graphene nanoribbon grown on the (110n) facet of SiC. The facet is formed via thermal relaxation of the step-edges of the trench made by lithography. B) Schematic of a full transistor device with source and drain electrodes and with a top gate insulated from the graphene layer to control the charge doping. Figure adapted from [100].

2.2.6 Other methods

In order to complete the picture, other minor examples of shaping graphene flakes are summarized here. One of them is to use catalytic particles to cut through graphene flakes. Metallic particles such as Fe or Ni interact with graphene in the presence of a hydrogen atmosphere and dissociate carbon-carbon bonds [103–106]. This interaction etches graphene with well defined edges. However the etching direction can not be predetermined and can follow random directions, creating a wide variety of geometrical nanostructures, as shown in Figure 2.12. TEM studies [107] and ab intio calculations [106] suggests that zigzag edge is more favourable to be followed by metal particles.

Another method is carbothermal etching of graphene sheets at 700 °C in Ar atmosphere which create hexagonal etch pits with nearly perfect edges confirmed by Raman measurements [108, 109]. The low D peak in the resulting Raman spectrum indicates low disorder and highly ordered zigzag edges. However, there are no transport measurement reported on nanoribbons created with this method. Other methods are to employ anisotropic etching during CVD growth [110–114] and using an AFM tip to create trenches by oxidizing carbon atoms on the surface [115].

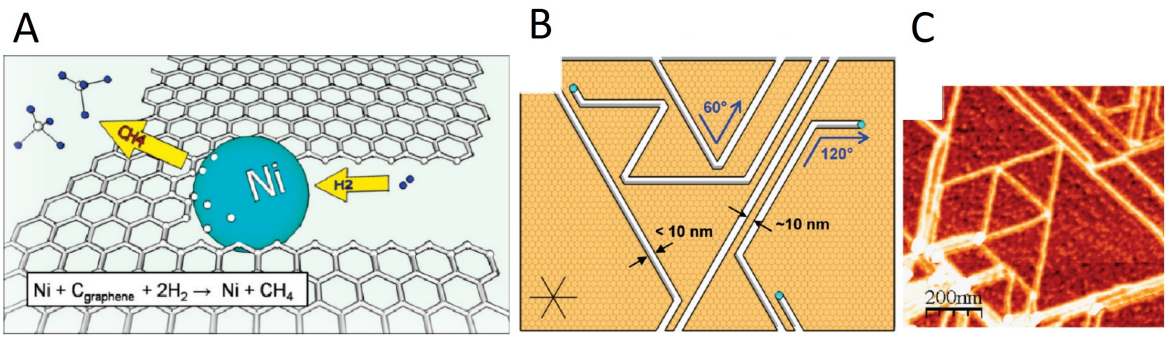

Figure 2.12: A) Cartoon of the process, showing the absorbtion of carbon from graphene by Ni particles. Inset shows the summary of the hydrogenetaion reaction of dissociated carbon atoms, forming methane as the yield of the reaction. B) and C) Sketch and AFM image of nanoparticle assisted etching in single layer graphene. Certain angles between trenches show how the chirality is preserved during the process, making randomly shaped nanostructures. Figure adapted from [103].

2.2.7 Hydrogen Plasma Etching

Among all the etching and growth techniques, those which are anisotropic are favourable since a crystallographic direction is chosen by the nature of the process. Hydrogen plasma etching is an anisotropic etching technique which creates hexagonal etch-pits with edges along the zigzag direciton. It was first proposed by McCarroll et al. [15, 116] and later studied by Yang et al.[117]. When graphene is exposed to hydrogen radicals, these radicals etch graphene, creating hexagonal holes starting from defective sites, as can be seen in Figure 2.13. The crucial point of this technique is that the process can be controlled by defining artificial defects via e-beam lithography to produce on-demand graphene nanoribbons and structures as illustrated in Figure 2.14 [118].

Several works have investigated the details of this process. The process was first develop for graphite flakes and then applied to graphene flakes. This revealed that the underlying substrate is highly influential for the etching characteristics. It has been shown that etching of single layer graphene on SiO_2 is isotropic and give circularly shaped holes [118–122]. The process is highly anisotropic on hBN [119, 122], graphite [117, 122] and for few layer graphene on SiO_2 [118, 120–122]. Atomic resolution Scanning Tunnneling Microscopy (STM) maeasurements showed that the etched edges on graphite are along

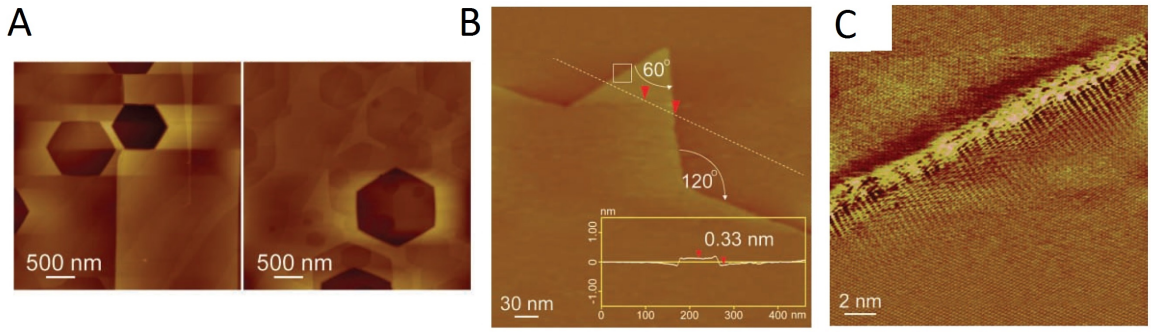

Figure 2.13: AFM images showing the hexagonal etch pits on graphite surface. A) Large scale hexagonal etch pits created by H plasma on the top layers of a graphite flake. B) STM image of two intersecting hexagonal etch pits of monolayer depth, as illustrated by the profile scan in the inset. C) Atomic resolution image of the square marked region in b, showing that the etched edge is parallel to the zigzag direction. Figure adapted from [117].

the zigzag direction, see Figure 2.13 C [117]. However, true microscopic picture could have never been achieved.

Early electronic transport studies on transistors with H plasma etched ribbons showed on-off ratios of about 10 [117] for narrow ribbons of 10 nm on SiO_2, which is a low ratio for a transistor device. Carrier mobility of $2'000\,cm^2/(Vs)$ was measured for a 10 nm wide few layer ribbon on SiO_2 [118]. A recent work from the same group reported carrier mobility of $10'000\,cm^2/(Vs)$ for 10nm wide single layer GNRs on hBN [119] and investigated the magnetotransport properties at low densities [123].

So far, no direct evidence have been shown to describe the etching process on the molecular level. An attempt with molecular dynamics situation gives some insight to the underlying chemical process [124]. This theory explains the etching process in

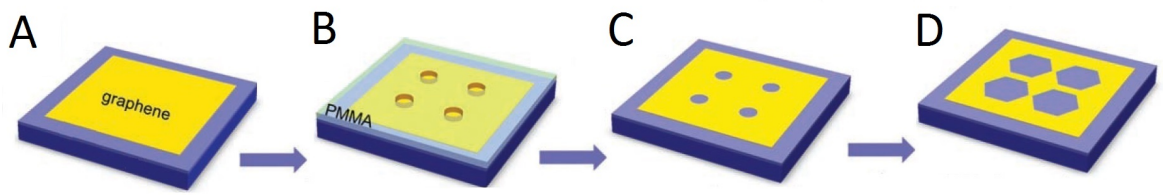

Figure 2.14: From A to D, the process to shape nansoturcutres by e-beam lithography is depicted. First, graphene is deposited on a suitable substrate, shown in purple. Then circular hole etch mask is introduced via e-beam lithography in the second step and the holes are etched with oxygen plasma in step C. At the final step, hydrogen plasma starts to etch from circular holes and form hexagonal holes. Figure adapted from [118].

three phases, as illustrated in Figure 2.15. Full hydrogenation of GNR free edges during phase 1 reduces the potential barriers to H chemisorption on near-edge C atoms from the basal plane. Subsequent hydrogenation of near-edge C-C dimers creates mechanical stress between C atoms (due to local sp^2-to-sp^3 rehybridizations) which leads to the rupture of C-C dimers bonds, unzipping locally the 1st and 2nd edge carbon rows. The unzipping then propagates randomly along the GNR edges and creates suspended linear carbon chains (phase 2). Due to the continuous H bombardment and strong thermal vibrations, the suspended carbon chains are weakened and may then rupture, leading to the sputtering of their carbon atoms as single C atoms or C_2 molecules (phase 3).

Even though this method has been known for some time and investigated by different groups, full characterization of physical and electronic properties are missing. The details of how the etching process depends on the etching parameters, characterization of edge quality and electronic measurements on ribbons created with that method will be the subject matter of the following chapters.

2.3 Raman Spectroscopy in Graphene

Raman microscopy is one of the most common techniques to characterize carbon based materials such as graphene, carbon nanotubes, fullerenes. It is fast, non-destructive and gives insight on structural and electronic properties of the surface. The features and interpretation of graphene Raman spectra are investigated and well-established in literature. A quick look at the Raman spectrum of a graphene flake can immediately disclose the number of layers, orientation or amount of disorder etc. Plus, further analysis of the Raman features can demonstrate more detailed properties of the structure, such as strain, doping, functional groups.

The Raman spectra of monolayer graphene have two distinctive features. The first one is the so called G-peak which appears at around $1580\,\mathrm{cm}^{-1}$ and the other one is the 2D-peak at around $2670\,\mathrm{cm}^{-1}$ for the laser excitation of wavelength 633 nm

(green). Another prominent peak which appears in the case of disorder is the D-peak at 1320 cm^{-1}.

The G-peak originates from a normal first order Raman scattering process as can be seen in Figure 2.16. It is associated with in-plane vibration of sp^2 carbon atoms and it is a doubly degenerate (TO and LO) phonon mode (E_{2g}) at the Brillouin zone center (Γ) [125] . On the other hand, the D and 2D peak originate from a second order (double resonance) process which involves two phonons for 2D peak and one TO phonon and one defect for D peak. The 2D peak is also called G′ in literature since it is the second most prominent peak of graphite samples after G peak. In graphene spectra, there is also D′ peak which is a weak disorder-induced feature, arising around 1620 cm^{-1}.

The double resonant process, shown in Figure 2.16 proceeds as follows: an electron of wave-vector $\vec{\mathbf{k}}$ around **K** valley absorbs a photon with energy E_{laser} and is scattered inelastically by a phonon or by a defect of wavevector **q** to another point around **K′** valley. The electron is then scattered back to the k state, recombines with a hole and

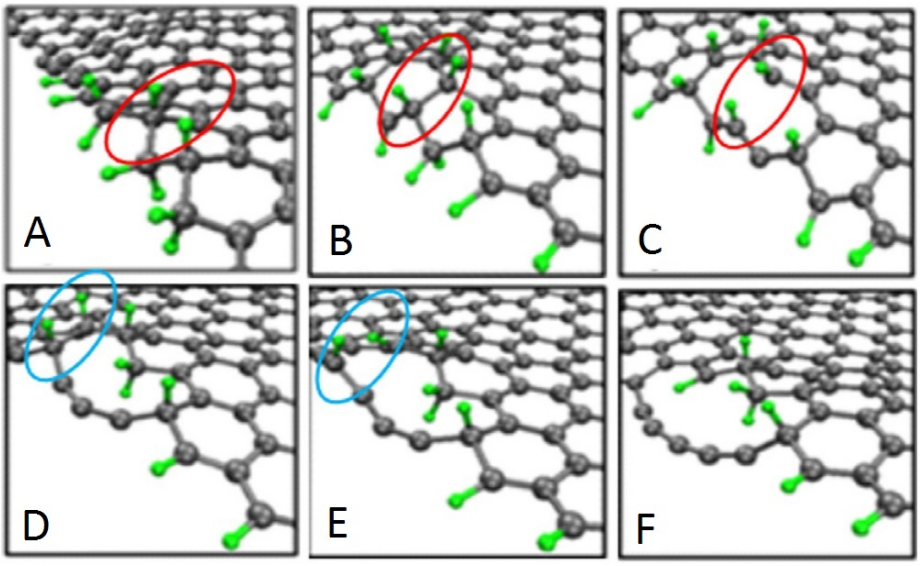

Figure 2.15: Illustration of the molecular dynamics simulation showing how the Hydrogen plasma dissociates carbon atoms at free edges of graphene. First, (A) the edges are hydrogenated (green is Hyrdogen) which leads to H chemiabsorbtion of near-edge atoms. (B-C) Subsequent hydrogenetaion breakes more C-C bonds, creating mechanical stress along the edge, while forming a long Carbon chain (D-E-F). At the last step, the full carbon chain breaks free from the graphene plane. Figure adapted from [124].

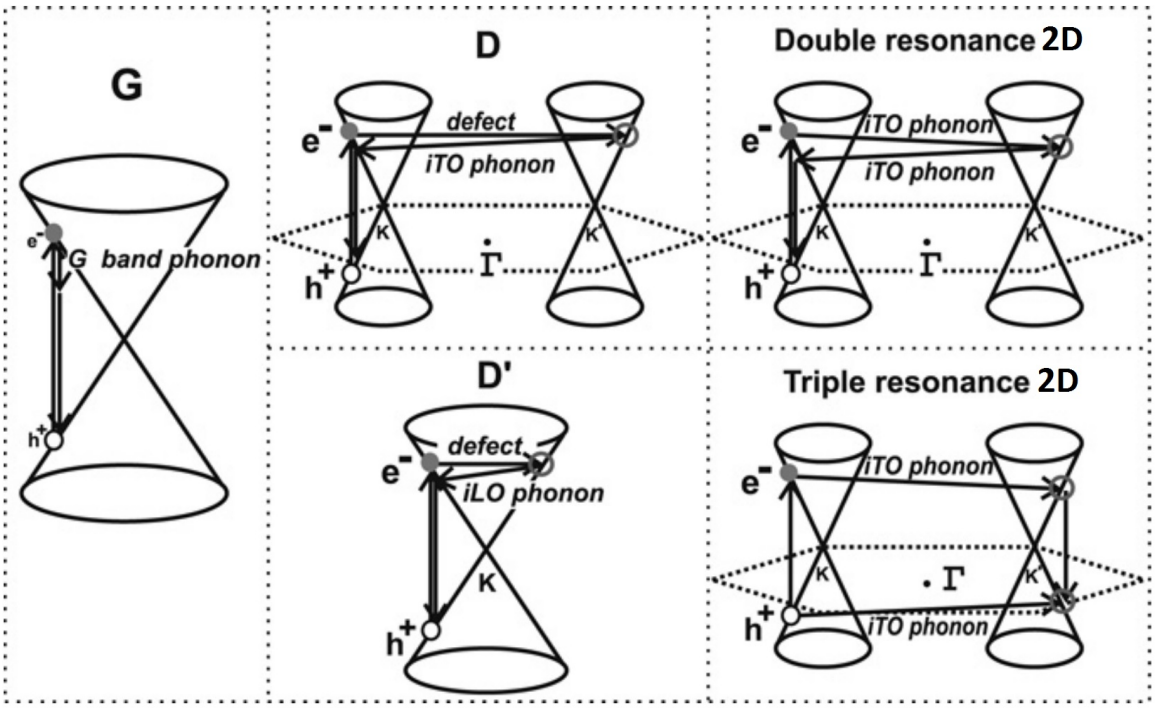

Figure 2.16: The resonance processes of phonons creating the G, D, D′ and 2D peaks. Figure adapted from [125].

emits a photon. If the two scattering process involve two phonons and are inelastic, then the result is the 2D-peak. On the other hand, if the electron is elastically scattered by a defect (instead of one phonon) and then inelastically by a phonon, then the process results in D-peak. This double resonance process is an intervalley process since the scattering events occur in between two inequivalent **K** and **K′** valleys in the first Brillouin zone of graphene. Moreover, the D′ peak is also a double resonance process but it is an intravalley process since it occurs in the same valley as pictured in Figure 2.16.

These main peaks, G, D and 2D, are used to determine the character of graphene samples at hand. First of all, one can determine the layer thickness by looking at the shape of 2D peak, especially to differentiate a single layer from multilayer. As can be seen in Figure 2.17, for single layer graphene, the 2D peak can be fitted with a single Lorentzian, whereas more layered samples require more peaks to be fitted. The multipeak structure of 2D peak for more than 2 layers is related to the dispersion of π electrons in graphene [127, 128]. In addition, the increase in intensity of the G-

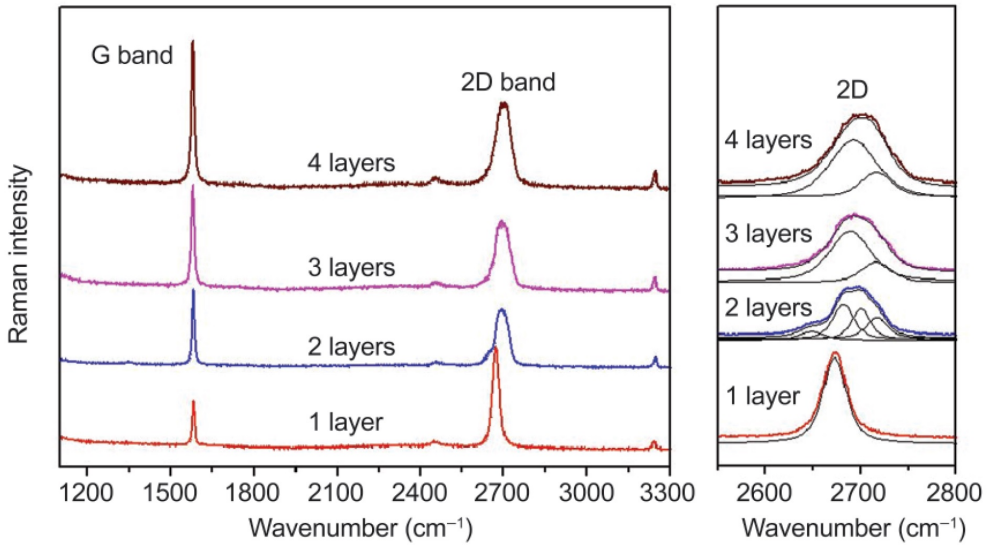

Figure 2.17: Raman spectra showing the difference in 2D peak height and shape depending on the number of layers. The single and multiple Lorentzian fits are shown in the right panel. Figure adapted from [126].

peak is due to the fact that more carbon atoms contribute to scattering for multilayer graphene. Secondly, mechanical deformations and charge doping also cause modifications in Raman spectra. A detailed analysis in the peak positions and bandwidths of G, D and 2D peaks can give information about whether the graphene sheet is under strain or if it is doped [33, 129, 130]. Especially, the relative intensity of 2D peak with respect to G peak, I(2D)/I(G), is a common method to determine if the graphene sheet is doped. High levels of doping will result in a significant decrease of this ratio [131].

2.3.1 Raman Spectrum of Graphene Edges

The disorder-related D peak is not only a measure of the density of defects in a graphene sheet, but also it is the litmus test to determine if an edge is armchair or zigzag terminated. The boundaries of a crystal is also considered as a defect, and for the case of monolayer graphene, the edges of a graphene sheet are extended one-dimensional defects and stimulate scattering events which contribute to D-peak intensity in the Raman spectra. For AC and ZZ edges, the double resonance process is different. This difference in the scattering event gives rise to D peak for AC edges, however it does

not occur for ZZ edges and results in the absence of a D peak. This feature can be utilized to determine if the edge is along ZZ direction or AC direction.

In Figure 2.18, the graphene lattice is depicted in real space (A) and in Brillouin zone (B), oriented according to real space. As explained, the double resonance process starts with a scattering event by a phonon of wavevector $\mathbf{q}$ from $\mathbf{K}$ valley to $\mathbf{K'}$ valley. After that the electron is scattered back to $\mathbf{K}$ valley by a defect in which momentum should be conserved such that $\mathbf{d_x} = -\mathbf{q}$. In panel A of Figure 2.18, the defect wavevectors are drawn for armchair and zigzag edges which are perpendicular to the edge. Comparing with the Brillouin zone picture, it is clear that the armchair wavevector $\mathbf{d_a}$ is able to complete the double resonance process by connecting two points near $\mathbf{K}$ and $\mathbf{K'}$ valleys. However, the zigzag wavevector $\mathbf{d_z}$ cannot connect two valleys for a momentum conserving elastic scattering event. Thus, the Raman spectra will show D peak only for armchair edges but not for zigzag edges [132]. This peculiar difference between armchair and zigzag edges has been observed experimentally by several groups and since then have been used as a method to differentiate between armchair and zigzag edges [132–134]. It should be noted here that the D′ band occurs for both armchair and

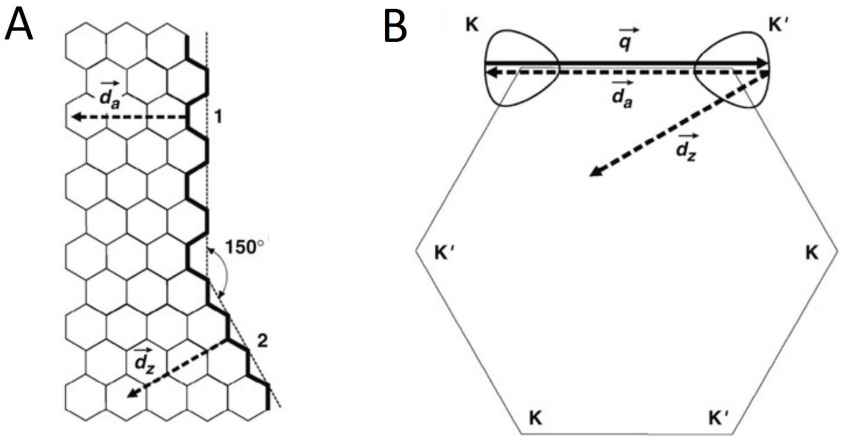

Figure 2.18: Schematic illustration of the double resonance process for zigzag and armchair edges. A) Graphene lattice in real space with edge-scatttering wavevectors corresponding to each edge. B) First Brillouin zone of graphene as the edge-scattering vectors are drawn parallel to real space. This image explicitly shows that the scattering from the zigzag edge does not intersect with another valley to complete the double resonance process. Figure adapted from [132].

zigzag edges since it is an intravalley process and can satisfy momentum conservation for both cases.

Indeed, this property depends severely on the quality of the edge. Ideally, a perfect armchair edge gives high D-peak, whereas for a zigzag edge, D-peak is absent. However, even though an edge generally follows a zigzag direction, it may include some armchair segments and this will result in some weak D-peak intensity. In this case, a more detailed analysis is highly useful to determine the percentage of armchair contribution along a zigzag edge. This brings into the play the polarization dependence of the incident and scattered light from these edges.

Raman scattering from these edges exhibits a polarization dependence on both the incident and scattered light polarizations [132, 134]. Because of the optical anisotropy of graphene, the optical absorption and emission is proportional to $\vec{\mathbf{P}} \times \vec{\mathbf{k}}$ where $\vec{\mathbf{P}}$ is the direction of polarization and $\vec{\mathbf{k}}$ is the wavevector of electron [125]. As a result of this polarization dependence, the D-peak intensity obtains a $\cos^2\theta$ factor where θ is the angle of incident light polarization with respect to $\vec{\mathbf{k}}$. This means that the D-peak intensity will be maximum when the light polarization is set parallel to the edge and

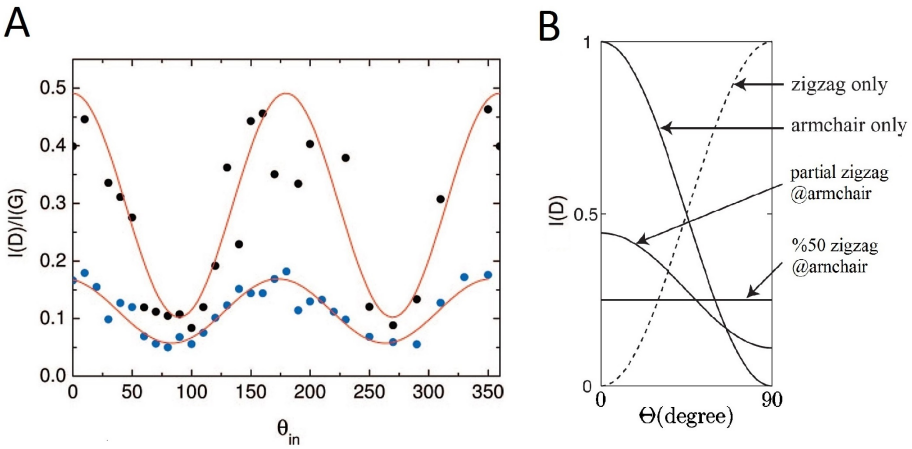

Figure 2.19: A) I(D)/I(G) as a function of θ_{in}, the polarization angle. As the polarization is swept, clear oscillations in D peak intensity is observed for two different edges. Black data points can be assigned to an armchair edge and blue data points to a zigzag edge including armchair segments. The clear finding is that the intensity is maximum when the polarization is parallel to the edge. Figures adapted from [134] B) Polarization dependence of G peak for pure zigzag, pure armchair and partial zigzag segments in average armchair direction. Figure adapted from [135].

minimum when perpendicular.

Further analysis by Casiraghi et al. [134] in a polarization dependent case proposed that, by scanning the angles of polarization, one can obtain the sinusoidal behaviour of the D peak and infer whether the edge is along armchair or zigzag direction and roughly determine its disorder. It should be noted that for impurities, short range defects and also short range AC segments at the edge (shorter than $\hbar\nu_{\mathrm{F}}/\epsilon \sim 0.6$nm where $\hbar$ is the Planck's constant, ν_{F} is the Fermi velocity of the electrons and ϵ is the energy of the electrons measured from Dirac point), the backscattering probability does not depend on the angle of incidence. So these kind of defects at the edge will result in D-peak intensity regardless of light polarization.

In Figure 2.19 A, I(D)/I(G) is represented for two cases, red curve for armchair edge and blue curve for zigzag edge where θ_{in} is measured with respect to the direction of the edge. One can clearly see that, both of these curves do not go to zero for perpendicular orientation, which implies that the edges have some defective sites to result in D peak. The ratio of $\mathrm{I(D)_{min}}$ to $\mathrm{I(D)_{max}}$ can also be used to extract the amount of disorder along the edge [134]. The general dependence of D peak intensity on the incident polarization direction can be written as:

$$I(D)(\theta_{in}) = I(D)_{min} + [I(D)_{max} - I(D)_{min}]cos^2(\theta_{in} - \theta_{max}) \tag{2.1}$$

where $\mathrm{I(D)_{min}}$ and $\mathrm{I(D)_{max}}$ are minimum and maximum D peak intensities and θ_{max} is the angle at which $\mathrm{I(D)_{max}}$ is measured. For long armchair segments (for nearly perfect edges) we expect $\rho_{\mathrm{A_0}} = \mathrm{I(D)_{min}/I(D)_{max}}$ to be small and θ_{max} to correspond to armchair direction. Now we can generalize this analysis to disordered cases. For armchair edges, a disordered armchair edge can have segments with 3 different orientations. If we assume the average armchair direction as reference, there will be some fraction f of

armchair segments at ±60°. Then we can sum up the intensities as follows:

$$\begin{aligned}&(1-f)[\rho_{A_0}+(1-\rho_{A_0})cos^2(\theta_{in})]+\\&(f/2)[\rho_{A_0}+(1-\rho_{A_0})cos^2(\theta_{in}-60^\circ)]+\\&(f/2)[\rho_{A_0}+(1-\rho_{A_0})cos^2(\theta_{in}+60^\circ)]\end{aligned} \tag{2.2}$$

which results in ratio of armchair segments along the average direction, ρ_A:

$$\rho_A=\frac{\rho_{A_0}+3f/(4-3f)}{1+3f\rho_{A_0}/(4-3f)}\geqslant\rho_{A_0} \tag{2.3}$$

On the other hand, a disordered edge along zigzag direction will include armchair segments at ±30° which we can denote as f_1 and f_2. Then addition of intensities can be represented as:

$$\begin{aligned}&f_1[\rho_{A_0}+(1-\rho_{A_0})cos^2(\theta_{in}-30^\circ)]+\\&f_2[\rho_{A_0}+(1-\rho_{A_0})cos^2(\theta_{in}+30^\circ)]\end{aligned} \tag{2.4}$$

which gives

$$\rho_Z=\frac{\rho_{A_0}+(2-k)/(2+k)}{1+\rho_{A_0}(2-k)/(2+k)},\qquad k=\sqrt{1+3\frac{(f_1-f_2)^2}{(f_1+f_2)^2}}. \tag{2.5}$$

For a symmetric edge, f_1 and f_2 should be equal to each other where the maximum intensity is measured to be along the edge direction. ρ_Z, the ratio of zigzag segments along the average edge direction, should be close to 1/3 for long armchair segments and close to 1 for short AC segments or defects.

Not only the D peak, but also the G peak has polarization dependence for different edge types. Theoretical calculations showed that only the longitudinal optical phonon mode is Raman active near an armchair edge whereas for zigzag edge the transverse optical phonon mode is active [135]. This asymmetry between the edge results in observable polarization dependence in the G-peak intensity. As depicted in 2.19 B, if the laser

polarization is defined with respect to edge direction, armchair (zigzag) edges have clear cosine (sinus) dependence. It is important to note here that, for disordered edges, the amplitude of this sinusoidal dependence attenuates and gives a flat response for a chiral edge with a 50 % mixture of zigzag and armchair segments. This dependence is also experimentally observed [136].

As summarized in this section, Raman microscopy is a powerful tool to characterize the type and quality of graphene edges. For our experiments, it is an essential technique to determine the structural properties of hydrogen plasma etched edges of single layer graphene flakes, as will be the topic of Chapter 4.

2.4 Reaching miliKelvin Temperature and Below

Cooling a device to low temperatures means, in principle, sucking the *heat* out of it, be it carried by the phonons or the electrons. This is achieved by efficient coupling of a cold reservoir at T_C to a hot object at T_H which will eventually thermalize at a final temperature $T_C < T_{final} < T_H$. Even though it is fairly easy to cool macroscopic or microscopic devices down to few Kelvin, cooling further below becomes a greater challenge and requires special techniques such as using dilution refrigerators and magnetic refrigeration.

The reasons behind the greater challenge are twofold. First of all, it is difficult to supply a significant amount of cooling power to cool and keep a nano electronic device at low temperatures stably. Secondly, the weak thermal transport in the case of insulators at low temperatures, heat leaks from the warmer environment and material heat release stand as other challenges for low temperature experiments. Hence, novel methods are necessary to overcome these challenges.

Today in modern research laboratories, commercially available and well-established systems are commonly used to cool below 1 K. Liquid helium cryostats and pulse-tube cryo-coolers are the two mostly used cryogenic apparatus to cool devices to about 4 K

by continuous operation. In order to go below 1 K, dilution refrigerators (DR) are used. These units can reach base temperatures of below 10 mK and are the workhorses for the low temperature experiments. However, one prominent limitation of dilution refrigerators is the weak coupling of the coldest parts of the refrigerator to the electronic system of the nano electronic device through insulating paths, resulting in electron temperatures that are typically higher (>50 mK) than the refrigerator temperature [137].

Adiabatic Nuclear Demagnetization (AND) is another well-known technique to reach below miliKelvin temperatures in condensed matter systems. In this technique, conduction electrons inside a metal are cooled directly by the nuclear spin bath. The lowest temperatures reported so far in a nuclear refrigerator (NR) are 1 μK for electrons in Pt [138] and 300 pK for nuclear spins in Rh [139]. One of the advantages of this method is the possibility of coupling the nuclear refrigerator to the measurement leads of a separate nanoelectronic device via conductive paths. A disadvantage on the other hand is that AND is a single-shot technique and it allows limited amount of time at the lowest temperature for the actual experiment.

Phonons and electrons are responsible for heat transport inside a material. Therefore, their thermal conductivity is an important parameter. At low temperatures ($T \ll \Theta_D$, where Θ_D is Debye temperature), the thermal conductivity of phonons, κ_{ph}, scales with T^3 and for electrons, $\kappa_{\mathrm{el}} \sim \mathrm{T}$. This results in weaker thermal conductivity as the temperature gets lower and it is further weaker for insulators where the heat can only be transported via phonons. Therefore, the cooling of conduction electrons in a condensed matter system is difficult through the insulating substrates.

AND stands as a more efficient technique since the conduction electrons are cooled directly by the nuclei and the cooling power can be transported via conductive materials such as the measurement leads of the nano electronic device to be measured. Here in this section, the physics of AND and main heat sources relevant to our experiment will be briefly explained. The techniques that are mentioned above has been known

to scientific community for some time and their working principles, properties and example structures can be found in detail in many textbooks [25, 32, 140–144]

2.4.1 Adiabatic Nuclear Demagnatization

Adiabatic Nuclear Demagnetization (AND) is to cool the nuclei of a paramagnetic material by bringing the system from a high energy magnetically ordered state to a low energy magnetically ordered state while the entropy is kept constant [25, 32, 140]. To explain the process, we consider an ensemble of nuclei with spin I at initial temperature T_i. First, a high initial magnetic field, B_i, is applied to the nuclear refrigerator in order to create a spin split state according to Zeeman effect:

$$\mathrm{E_Z} = -\mathrm{m}\mu_\mathrm{n}\mathrm{g_n}\mathrm{B} \tag{2.6}$$

with nuclear magneton μ_n, nuclear g-factor g_n and magnetic quantum number m (running from +I to -I), see Figure 2.20.

As a result of this high spin polarization, a significant amount of heat is produced. In the second step of the process, which is called *precooling*, this heat of magnetization is absorbed by the dilution refrigerator. The duration of this process depends on the cooling power and thermal conductivity between two systems. Eventually, both systems are thermalized at the initial (precooling) temperature, T_i.

After thermalization, the NR and the DR are thermally disconnected from each other by the help of superconducting (Al) heat switches [145]. This is to assure that the cooling power supplied during the demagnetization step is not wasted to the warmer parts of the cryostat.

The third step, *demagnetization*, is to ramp down the magnetic field adiabatically to a final field B_f which is the key step where the cooling happens. In the high temperature

limit, $E_Z \ll k_B T$, the molar entropy of the nuclear spin system is defined as [25]:

$$S = R \ln(2I + 1) - \frac{\lambda_n B^2}{2\mu_0 T_n^2}, \tag{2.7}$$

where R is the molar gas constant, λ_n is the molar Curie constant, μ_0 is the vacuum permeability and $_n$ is the temperature of the nuclei. Figure 2.21 shows the molar nuclear spin entropy for copper (I=3/2) as a function of temperature. The red arrow shows the reduction in temperature when the magnetic field is ramped down from 8 T to final field of 80 mT for a perfectly adiabatic process where the entropy is kept constant. Then the final temperature is obtained as:

$$S(\frac{B_i}{T_i}) = S(\frac{B_f}{T_f}) \;\Rightarrow\; T_f = T_i \frac{B_f}{B_i}. \tag{2.8}$$

So, the reduction in magnetic field determines the reduction of temperature in an ideal process. The final magnetic field could be chosen as low as possible to reach the lowest temperatures. However, it should be determined according to two mechanisms. First, B_f must be higher the internal magnetic field of the NR where the internal interactions

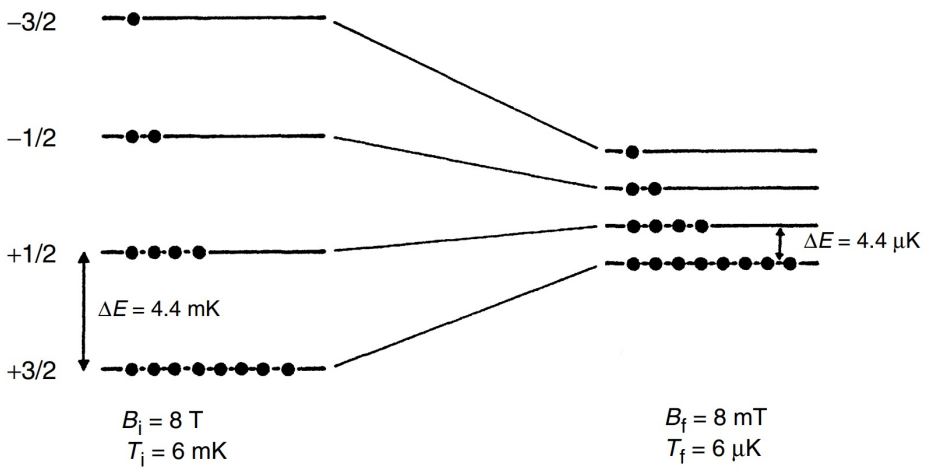

Figure 2.20: Zeeman levels of Cu nuclei with spin $I = 3/2$ before and after demagnetization step. Zeeman splitting and the relative population of the levels are calculated for nuclear spin temperature of 6 mK at 8 T. When the field is adiabatically reduced to 8 mT, the relative population of nuclear spin states are maintained, resulting in lower nuclear spin temperature of 6 μK. Figure taken from [25].

will align the magnetic moments in the NR at the lowest temperature. Second, the cooling power of the nuclear spin bath decreases with magnetic field due to decreasing heat capacity of the nuclei ($C_n \propto B^2/T^2$). Therefore, an optimum final magnetic field can be determined with hyperfine coupling strength K, total heat leak in the system $\dot{Q}_t$ and the molar Curie constant [25]:

$$\mathrm{B_{f,opt}} = \sqrt{\frac{\mu_0 \mathrm{K} \dot{\mathrm{Q}}_\mathrm{t}}{\lambda_\mathrm{n}}}. \tag{2.9}$$

In reality, the final temperature is affected by the heat leaks onto the nuclear refrigerator. These external heat leaks will cause deviations from perfect adiabaticity and result in a higher final temperature. With that in mind, we can define the efficiency of the process as:

$$\xi = \frac{\mathrm{B_f}}{\mathrm{B_i}} \frac{\mathrm{T_i}}{\mathrm{T_f}}, \tag{2.10}$$

which gives $\xi = 1$ for an ideal AND process and $\xi < 1$ for a realistic process due to heat leaks. These heat leaks not only cause higher final temperatures but they are also the reason for warm-up after the system reaches its final temperature. Since AND is a single-shot technique, which means it does not supply continuous cooling power, the final temperature can be only kept for a finite amount of time, hours or days, given by,

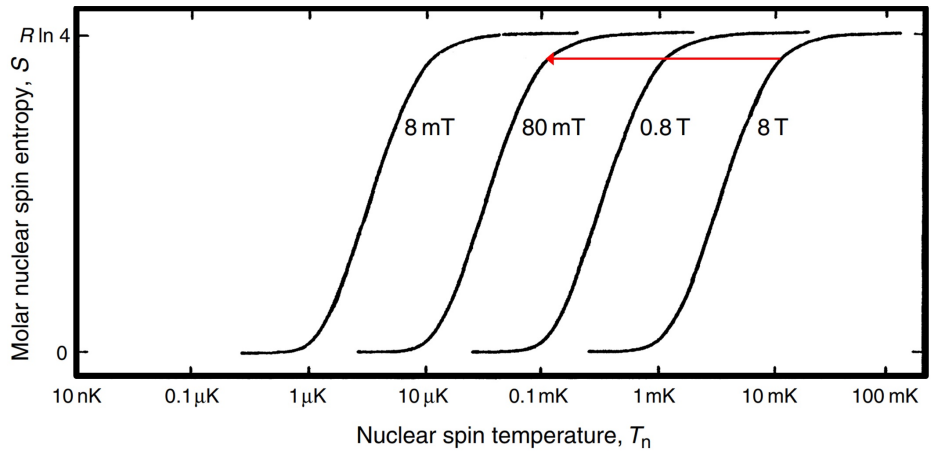

Figure 2.21: Molar nuclear spin entropy of nuclear system calculated for Cu in four different magnetic fields as a function of temperature. Red arrow shows the adiabatic demagnetization process from 8 T to 80 mT. Figure adapted from [25].

again, the amount of heat leak to the system.

2.4.2 Heat Sources

It is impossible to completely isolate an object from its environment and impossible to stop heat flowing from hot to cold. This means that, the device which is cooled to very low temperatures always has a link to other parts of the cryostat, which are eventually at room temperature. So, there is always heat flowing from the warmer environment to the cold device. Not only does one need to supply cooling power continuously, but also extra care should be taken for proper isolation, shielding of black body radiation from warmer parts of the cryostat, filtering to eliminate the high frequency noise from the leads and efficient thermalization of the leads.

One typical source of heat is due to the gas particles filling the space in a cryostat. This can be highly reduced by pumping the system to high vacuum ($\leq 10^{-5}$ mbar). Second one is the black body radiation from high temperature parts of the system to low temperature parts, determined by Stefan-Boltzman law. Although, it is impossible to eliminate completely, the excess heat can be reduced by protective shielding made of highly reflective materials such as space foil. Another less obvious heat leak is due to the internal relaxation in materials, called heat release. When a cryo system is designed and built, the materials used in the system should be chosen accordingly for lowest heat release possible.

Regarding the nanodevices, radio-frequency radiation which couples to measurement leads from room-temperature equipment can bring extra heat to the electronic system. This common problem needs proper filtering of the measurement leads, for example, by lossy thermo-coaxes [146] and with silver-epoxy microwave filters [137]. Also, due to electrical resistance, nanodevices are effected by Joule heating when voltage bias is applied during transport measurements.

Among many, one particular heat source is highly relevant for the study explained in this thesis. When a conductor is placed in a time-varying magnetic field, $\dot{B}$, or

when a conductor moves in an inhomogeneous magnetic field, eddy currents are generated. This effect produces heat continuously as long as magnetic fields and mechanical vibrations are present in the system. The generated heat can be described by:

$$\dot{Q}_{eddy} = \frac{GV\dot{B}^2}{\rho} \qquad \text{and} \qquad \dot{B} = \frac{dB}{dt} = \frac{dB}{d\vec{r}}\frac{d\vec{r}}{dt}. \tag{2.11}$$

Here, G stands for the geometry factor, ρ is the resistivity and V is the volume. To prevent eddy current heating, dimensions and structure of the metals inside the magnetic field region must be carefully designed and the magnetic field inside the solenoid volume must be as homogeneous as possible. The mechanical vibrations in the cryostat must also be reduced efficiently. Floating tables to decouple the cryostat from environment, big cement blocks and bellows to damp vibrations coming from pumps are solutions to the vibration problems. As will be discussed in detail in Chapter 5, pulse tubes are one of the main sources of vibrations in modern cryo-free systems.

2.4.3 State of the Art for microKelvin

While ultra-low temperature experiments have been extensively carried out in quantum fluids or pure metals [32], cooling semiconductor devices below miliKelvin has proven to be extremely challenging since the cooling power from a refrigerator must be carried to a nanoelectronic device along resistive paths. Adiabatic nuclear demagnetization has been utilized in cryo-free systems by single nuclear refrigerants which required insulating links to the nanoelectronic device [147–149]. This, naturally, was inefficient to cool conduction electrons due to reasons explained in previous sections. Up to the day this thesis is being written, electron temperatures below 1 mK have never been reported in semiconducting nanoelectronic devices. Nevertheless, the state of the art now approaches to this limit by cooling normal metal-insulator-superconductor (NIS) junction devices and Coulomb Blockade Thermometers (CBTs) via adiabatic nuclear demagnetization [31, 150–152].

Coulomb Blockade Thermometry was invented in 1994 by J.P.Pekola et al. and measured at 4.2 K [29]. So far, CBTs have been improved by several groups, resulting in lower electron temperatures. The device design has been modified by introducing large cooling fins to increase electron-phonon coupling and also the experimental setups were altered for minimized heat leaks and increased AND performance. Implementing microwave filters on measurement leads helped to reduce the heat leak due to electrical noise and resulted in electron temperatures below 10 mK [137, 150]. Advances in fabrication of CBT samples allowed to lower the charging energy of the tunnel junctions which increased the precision of temperature measurement in few mK range. Upon this improvement, electron temperatures of 3.8 mK is reached in a He^3 immersion cell [153] and of 4.5 mK [151] and 2.8 mK [31] via on-chip magnetic cooling.

3 Anisotropic Etching of Graphite and Graphene in a Remote Hydrogen Plasma

D. Hug, S. Zihlmann, M.K. Rehmann, Y.B. Kalyoncu, T.N. Camenzind,

L. Marot, and D.M. Zumbühl

Department of Physics, University of Basel, CH-4056 Basel, Switzerland

K. Watanabe, T.Taniguchi

National Institute for Material Science, 1-1 Namiki, Tsukuba 305-0044, Japan

This chapter was published in *npj 2D Materials and Applications* **1**, 21 (2017).

3.1 Abstract

We investigate the etching of a pure hydrogen plasma on graphite samples and graphene flakes on SiO_2 and hexagonal Boron-Nitride (hBN) substrates. The pressure and distance dependence of the graphite exposure experiments reveals the existence of two distinct plasma regimes: the *direct* and the *remote* plasma regime. Graphite surfaces exposed *directly* to the hydrogen plasma exhibit numerous etch pits of various size and depth, indicating continuous defect creation throughout the etching process. In contrast, anisotropic etching forming regular and symmetric hexagons starting only from preexisting defects and edges is seen in the *remote* plasma regime, where the sample is located downstream, outside of the glowing plasma. This regime is possible in a narrow window of parameters where essentially all ions have already recombined, yet a flux of H-radicals performing anisotropic etching is still present. At the required process pressures, the radicals can recombine only on surfaces, not in the gas itself. Thus, the tube material needs to exhibit a sufficiently low H radical recombination coefficient, such a found for quartz or pyrex. In the *remote* regime, we investigate the etching of single layer and bilayer graphene on SiO_2 and hBN substrates. We find *isotropic* etching for single layer graphene on SiO_2, whereas we observe highly *anisotropic* etching for graphene on a hBN substrate. For bilayer graphene, anisotropic etching is observed on both substrates. Finally, we demonstrate the use of artificial defects to create well defined graphene nanostructures with clean crystallographic edges.

3.2 Introduction

Graphene nanoribbons (GNRs) have emerged as a promising platform for graphene nano devices, including a range of intriguing quantum phenomena beyond opening of a confinement induced band gap [13, 34, 38, 40, 154].In armchair GNRs, giant Rashba spin-orbit coupling can be induced with nanomagnets, leading to helical modes and spin filtering[51]. Further, Majorana fermions localized at the ends of the ribbon were predicted in proximity of an s-wave superconductor[51]. Zigzag ribbons, on the other hand, were proposed as a promising system for spin filters[38]. Theory showed that electronic states in zigzag ribbons are strongly confined to the edge[34, 38, 40], recently observed in experiments[86, 96, 155, 156]. Further, edge magnetism was predicted to emerge at low temperatures[12, 34, 38, 40, 157], with opposite GNR edges magnetized in opposite directions. High quality, crystallographic edges are very important here, since edge disorder suppresses magnetic correlations[12] and tends to cause electron localization, inhibiting transport studies. GNRs fabricated with standard electron beam lithography (EBL) and Ar/O_2 etching typically exhibit pronounced disorder [50, 57, 58, 158–161], complicating transport studies.

Fabrication methods creating ribbons with clean crystallographic edges were recently developed, including carbon nanotube unzipping [81, 83], ultrasonication of intercalated graphite [78], chemical bottom up approaches [93, 97], anisotropic etching by nickel nanoparticles [103], or during CVD processing [110–112], or carbothermal etching of graphene sheets [108, 109, 162, 163]. Here, we use a hydrogen (H) plasma etching technique [116–119, 164] because it allows precise, top-down and on-demand positioning and tailoring of graphene nanostructures. Such nanostructures can easily be designed to spread out into larger graphene areas incorporated into the same graphene sheet, thus providing for a relatively easy way to make electrical contacts.

In this work, we investigate the anisotropic H plasma etching of graphite surfaces in dependence of the gas pressure and the sample - plasma distance (see Methods).

We find that the etching characteristics can be divided into a direct and a remote plasma regime. In the *direct* plasma regime, the sample is placed within the glowing plasma, and surfaces show many hexagons of various sizes indicating a continuous defect induction throughout the etching process. In the *remote* plasma regime, on the other hand, the sample is placed downstream of the glowing plasma, and etching occurs only from preexisting defects which makes the fabrication of well defined graphene nanostructures possible. Further, we have prepared single layer (SL) and bilayer (BL) graphene flakes on SiO_2 and hexagonal boron nitride (hBN) substrates and exposed them to the remote H plasma. We observe a strong dependence of the anisotropy of the etch on the substrate material. SL graphene on SiO_2 is etched isotropically, confirming previous findings[118, 120], whereas we observe highly anisotropic etching of SL graphene on hBN [119], producing very regular and symmetric hexagonal etch pits. Anisotropic etching of SL graphene on hBN offers the possibility to fabricate diverse graphene nanostructure with well defined edges (e.g. GNRs) and allows investigation of their intrinsic electronic transport properties.

3.3 Results

3.3.1 Etching on Graphite: *Direct and remote plasma regimes*

We first investigated graphite flakes, allowing for rather simple and fast processing. The graphite specimen[165] were cleaned by peeling with scotch tape and subsequently exposed for one hour to a pure H plasma at a temperature T = 400 °C and a distance d from the end of the surfatron. We first present the distance dependence of the H plasma process. Figure 3.1A shows AFM topography scans for exposures of one hour at four different distances at constant pressure $p = 1$ mbar. At the larger distances, etch pits of monolayer step height are created upon plasma exposure, exhibiting a regular hexagonal shape and demonstrating a strongly anisotropic process [116, 117]. All observed hexagons exhibit the same orientation. From previous studies, it is known that

hexagons created by exposure to a remote H plasma exhibit edges pointing along the zigzag direction [116, 117]. As the sample is brought closer to the plasma, significantly more etch pits appear, often located at the border of existing holes, sharing one common hexagon side (see Figure 3.1A, $d = 42\,\mathrm{cm}$). For the closest position $d = 37\,\mathrm{cm}$ – unlike the larger distances – the sample is located within the visible plasma glow region, resulting in a strong and several layers deep scarring of the entire surface.

To quantitatively study the distance dependence, we evaluated larger images to gather better statistics and plot histograms showing the number of holes as a function of diameter, see Figure 3.1B-D. The overall number of holes obviously increases strongly with decreasing sample-surfatron distance d. For small distances, a wide distribution of diameters is seen, ranging from several 100 nm down to nearly vanishing hexagon size, suggesting that new defects serving as etch seeds are created throughout the exposure time. The width of the hole diameter distribution is given by the anisotropic etch rate and the exposure duration in this regime. For larger d, on the other hand, the few holes seen have comparable diameters, consistent with etching proceeding predominantly from preexisting graphite defects, without adding new defects. This results in a narrow width of the distribution of hole sizes. As previously reported [116–118], exposure to energetic ions seems to create defects, while exposure to hydrogen radicals appears to result in anisotropic etching and growth of hexagons centered around preexisting defects and borders.

Next, we turn to the pressure dependence. In Figure 3.2A, AFM topography images are shown at four different pressures p at constant distance $d = 52\,\mathrm{cm}$. The number of holes increases with decreasing pressure, similar to decreasing distance, giving rise to etch pits of monolayer step height at intermediate pressures. At the highest pressures, however, no etch pits were observed, in strong contrast to the lowest pressure, where ubiquitous and deep etching is seen, demonstrating the strong influence of p. Analyzing the etch pits using histograms confirms that p and d have a similar influence on the etching process (compare Figure 3.2B, C with Figure 3.1B-D). Figure 3.1E summarizes

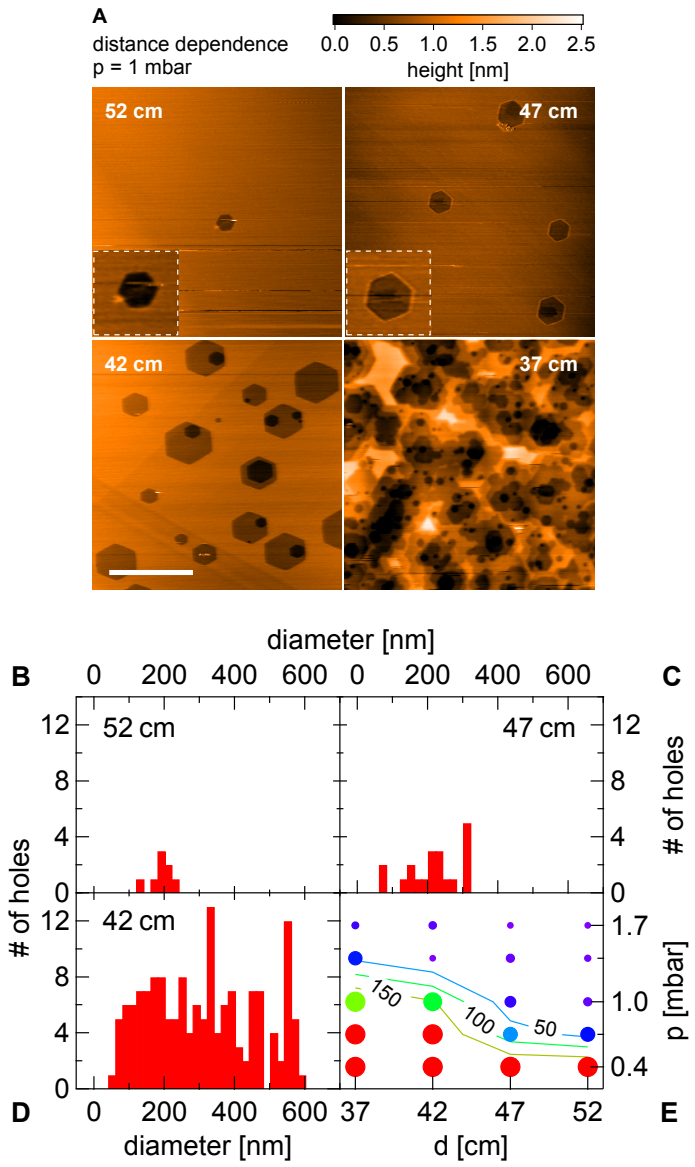

Figure 3.1: Distance dependence of graphite exposures
(A) AFM images (tapping mode) of graphite surfaces for various distances d, as labeled, all exposed to the plasma for 1 h at p = 1 mbar and T = 400°C, all shown on the same color scale. Main panels are $3 \times 3\,\mu m^2$, scale bar is $1\,\mu m$, insets (dashed white boxes) are $0.25 \times 0.25\,\mu m^2$. Slight hexagon distortion at 42 cm is an imaging artefact due to drift. (B-D) Histograms obtained from $10 \times 10\,\mu m^2$ scans, showing the number of holes against hole diameter (bin size 20 nm). (E) The size of the circle markers corresponds to the width of the diameter distribution. The color indicates the number of holes, with red corresponding to large number of holes. For samples located within the glowing plasma (red circles), a lower bound of 300 holes and a minimum width of distribution of diameter of 600 nm is shown.

the histograms of all investigated graphite samples, using color to represent the number of holes, while the size of each marker is proportional to the width of the distribution of hole diameters. A clear correlation between the number of holes and the width of

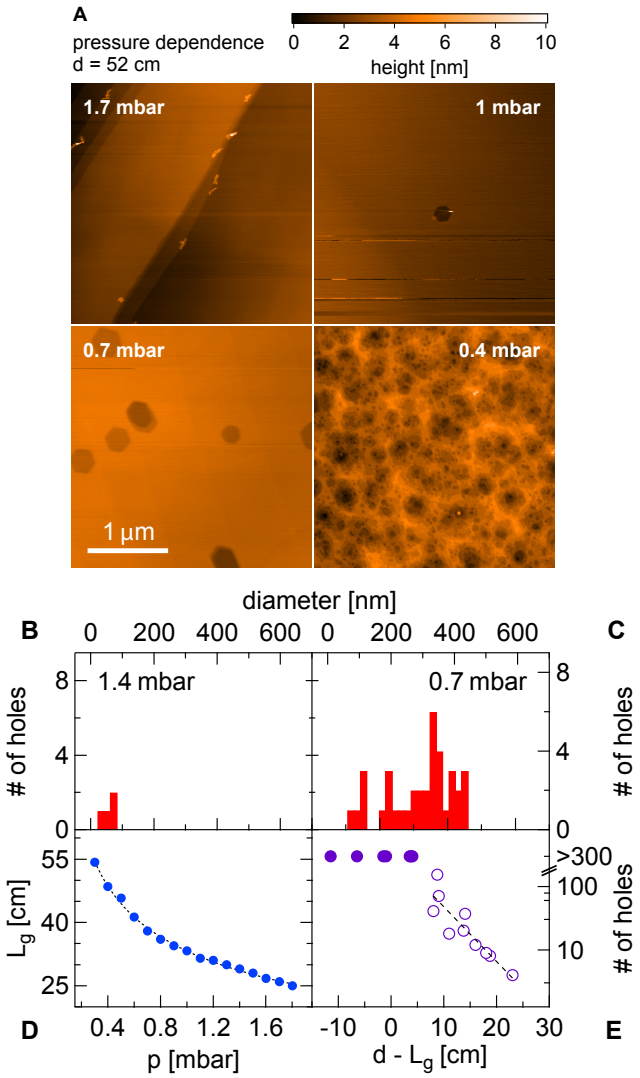

Figure 3.2: Pressure dependence of graphite exposures
(A) AFM images (tapping mode) of graphite surfaces for various p, as indicated, exposed for one hour at $d = 52\,\text{cm}$ and $T = 400°\text{C}$, all shown on the same color scale. All panels are $3 \times 3\,\mu\text{m}^2$. (B,C) Histograms from $10 \times 10\,\mu\text{m}^2$ scans, displaying the number of holes against hole diameter (bin size 20 nm) for p as labeled. (D) Length L_g of the optically visible plasma as a function of p. The dashed curve is a $1/\sqrt{p}$ fit. (E) Number of holes versus distance from plasma edge $d - L_g$. A lower bound of 300 holes is given for the heavily etched cases where an exact hole-count was not feasible. The dashed black line is an exponential fit to the data with < 300 holes with 1/e decay length ~ 5 cm.

the distribution is seen: the largest circles are red, while the small circles are purple.

The analysis of the graphite exposure data leads to two qualitatively different types of processes: the *direct* and the *remote* plasma regime. In the *direct* plasma regime (large, red circles, Figure 3.1E), the sample is located directly within the plasma discharge region, hence exposing it to large densities of radicals and ions, capable of inducing

defects throughout the exposure, giving a broad hole diameter distribution. In the *remote* plasma regime (small, purple circles, Figure 3.1E), on the other hand, the sample is positioned outside, downstream of the plasma generation region, where ions have recombined and only a residual flux of radicals is present. There, etching proceeds predominantly from preexisting defects and edges, leaving the basal planes mostly untouched. In this regime, a narrow distribution of hole diameters results, centered around the diameter given by the anisotropic etch rate and the exposure time.

Further, there is an intimate connection between distance and pressure: lower pressure results in a longer gas mean free path and therefore a larger average distance for recombination in the diffusive gas. This results in a larger length of the plasma column $L_g(p)$, measured from the edge of the visibly glowing plasma to the surfatron, see Figure 3.2D. Thus, changing the pressure with fixed sample position modifies the distance between sample and plasma edge. Hence, it is useful to introduce an effective distance $d' = d - L_g(p)$, the distance from the sample to the edge of the glowing plasma. Thus, $d' \lesssim 0$ roughly marks the direct plasma regime while $d' \gg 0$ signifies the remote plasma regime. Reactive particles are generated inside the plasma column and start recombining once they have left the plasma generation region.

3.3.2 Kinetics of Hydrogen Plasma in a Quartz Tube

The reaction kinetics in low temperature H plasmas are highly non-trivial despite the relatively simple chemical composition [166]. Nevertheless, it is well known that at the pressures used here ($p \sim 1\,\mathrm{mbar}$), the predominant radical decay mechanism is surface mediated association rather than gas collisions. Two colliding H atoms require a third body to carry away the excess energy for association to occur [167]. However, under the present conditions, three body collisions are very unlikely, thus leaving only the surface assisted process (which also leads to surface heating [168]). Recombination of ions, in contrast, can also occur through an additional collisional channel, in absence of a surface. Which species – ions or radicals – decay on a shorter length scale downstream

of the plasma edge thus depends on both the surface properties and gas parameters. For anisotropic etching without defect creation, a flux of H radicals in absence of ions is needed, as previously reported [116–118], thus requiring the ion density to decay on a shorter length than the radicals.

The surface attenuation of H radicals thus plays an important role, and was previously studied [168, 169]. Some glasses such as pyrex or quartz – as used in our experiments – were identified as a materials with a low recombination coefficient, particularly compared to some common metallic surfaces such as stainless steel and aluminum. This weak surface attenuation can open a downstream window offering a flux of H radicals while essentially all ions have already recombined, as desired and achieved here, see e.g. Figure 3.1B, 3.2B and 3.3 (below). Nevertheless, the etch rate in the downstream window was observed to decrease slowly over long periods of time, reaching a vanishingly small etch rate after more than 100 hours of plasma exposure. The elevated temperatures in the furnace may enhance impurity migration towards the surfaces of the tube, possibly amplifying the surface attenuation of H radicals. Larger anisotropic etch rates were observed when utilizing higher purity quartz tubes manufactured from synthetic fused silica [170], supporting the assumption of the role of impurities. High impurity content and even small amounts of metallic deposition on the tube wall give wave damping due to dielectric losses and result in an enhanced decay of radicals.

To study the decay of reactive species, we note that the ion flux is proportional to the number of holes created. We find a roughly exponential decrease of the number of holes with distance, see Fig.3.2E and supplementary online materials (SOM), with a 1/e decay length of about 5 cm. The anisotropic etch rate, on the other hand, is related to the flux of H radicals. We extract the anisotropic etch rate, defined as the growth per unit time of the radius of a circle inscribed to the hexagonal etch pit, averaged over a number of holes, shown in Figure 3.4A. Only the largest set of hexagons of each exposed graphite sample were evaluated to obtain the etch rate, since smaller holes might not have etched from the beginning of the exposure. As expected, the anisotropic etch

rate is largest for small distances, falling off quickly with increasing separation from the plasma edge. There is also an apparent pressure dependence, with larger pressures tending to give lower etch rates, see Fig. 3.4A. Given only two or three points along the d-axis for each pressure, and only few holes for some parameter sets (d, p), a reliable H-radical decay length cannot be extracted from these data. A theoretical estimate gives an H-radical decay length of $\sim 12\,\mathrm{cm}$, see SOM, in agreement with observations in Fig. 3.4A, and longer than the ion decay length of 5 cm, as observed. The etch rates we extract are a few nm per min at 400 °C, consistent with previous reports [117, 118].

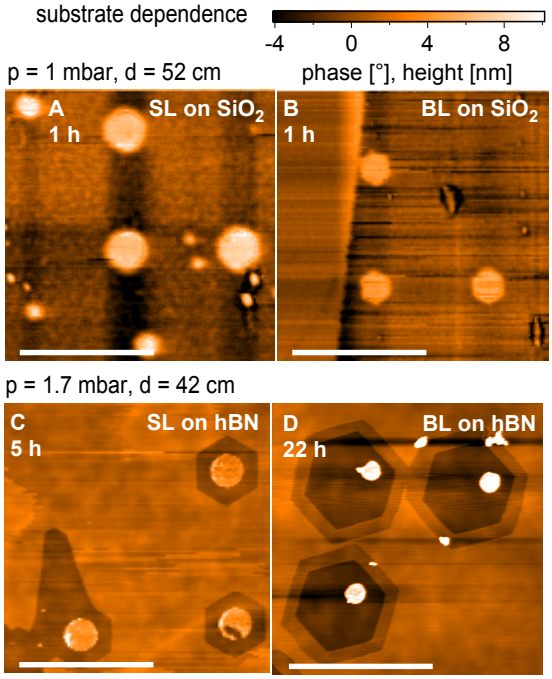

Figure 3.3: Substrate dependence of SL/BL graphene (A,B) AFM phase contrast images of a SL (A) and BL (B) section of the same flake on a SiO_2 substrate, etched for 1 h at $T = 450\,°C$. Round holes of 50 nm diameter were defined before H-etching. AFM topography image of a SL (C) and BL (D) flake on hBN etched for 5 h and 22 h, respectively. Holes of 200 nm (SL) and 100 nm (BL) were defined before etching. For (D) the color scale values are divided by four. The scale bars on all images are 1 μm.

3.3.3 Etching on Single and Bi-layer Graphene: *Substrate Dependence*

Next, we study the plasma exposure of SL and BL graphene exfoliated onto a SiO_2 substrate using the established tape method [6]. We patterned disks using standard EBL and reactive ion etching with an Ar/O_2 plasma, resulting in circular graphene holes

which were subsequently exposed to the remote H plasma in the regime where H radicals but essentially no ions are present, as determined from the graphite experiments. BL graphene grows regular hexagons with parallel sides (see Figure 3.3B), as expected from the graphite results. SL graphene, on the other hand, displayed mostly round holes (see Figure 3.3A), though some weakly developed, irregular hexagonal shapes are also occasionally seen. Further, several additional, not EBL defined holes appear on the SL after exposure, all smaller than the EBL initiated etch pits. After a second plasma exposure, the number of holes on the SL increased further, indicating generation of new defects, while only EBL defined holes appear on the BL. Note that the SL and BL regions shown in Figure 3.3A and B are located on the same graphene flake, ensuring identical plasma conditions.

In addition, the average hole diameter on SL is visibly larger than on the BL (Figure 3.3A and B) after the same exposure time, indicating a faster etch rate on SL. Thus, SL on SiO_2 is more reactive when exposed to the plasma and no longer anisotropic when exposing . This is consistent with previous reports [118–120], and is suspected to arise from charge inhomogeneities in the SiO_2 substrate [171–173] or other SiO_2 surface properties. A broad range of plasma parameters in the remote regime were investigated for SL and BL samples on SiO_2, giving qualitatively similar results (isotropic SL etching). The etch rate for SL and BL on SiO_2 is shown in Figure 3.4B. For the SL samples, only the EBL defined holes were evaluated, ignoring the plasma induced defects, since these do not etch from the beginning of the exposure. Clearly, for all plasma parameters studied, SL exhibits a significantly larger etch rate compared to BL [117, 120], as already visible from the AFM images in Figure 3.3A and B. The temperature dependence of the etch rate for both SL and BL on SiO_2 is shown in Figure 3.4C. The etch rates are strongly reduced at temperatures far above and below the process temperature, consistent with previous reports [117, 120], and consistent with reported hydrogen recombination rates on quartz increasing dramatically with temperature [174].

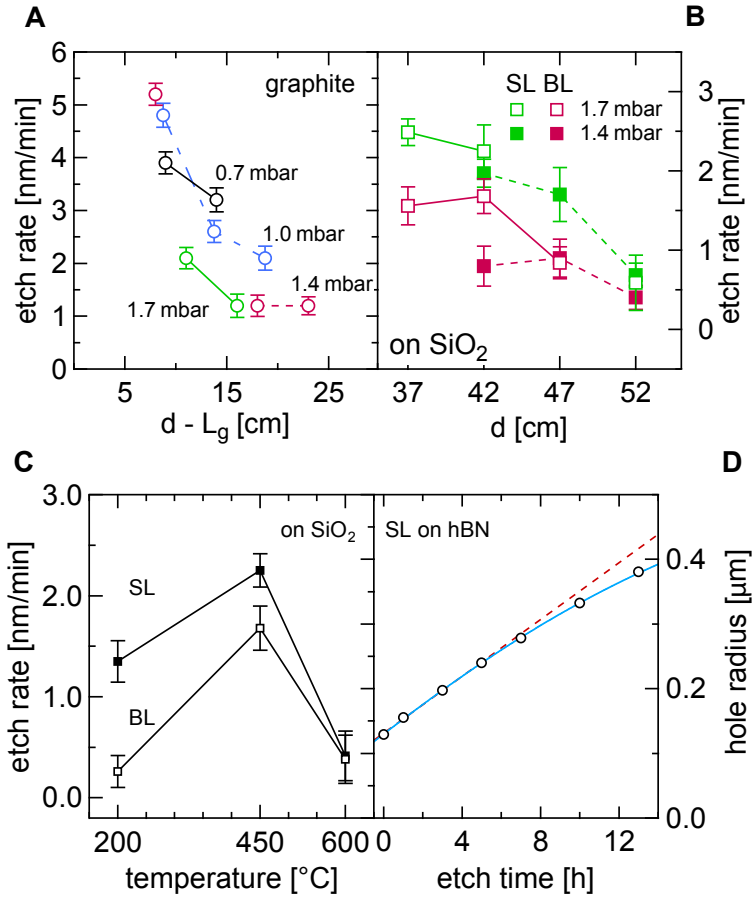

Figure 3.4: Anisotropic etch rates (A) Graphite anisotropic etch rate versus distance from plasma $d - L_g$ for several configurations. (B) Etch rate of SL and BL on SiO_2 at indicated parameters. (C) Temperature dependence of the etch rate of SL and BL samples on SiO_2. (D) Average radius of a circle inscribed to the hexagonal etch pits as a function of exposure time for SL on hBN. Several etch pits were evaluated in order to obtain average size and standard deviation, where the latter is smaller than the diameter of the marker circle. The dashed red line is a linear fit to the points at ≤ 5 h, the blue curve is a tanh-fit shown as a guide for the eye.

To study the substrate dependence, we use high-quality hBN crystals as grown in Ref. [175]. SL and BL graphene were aligned and deposited onto areas covered with several 10 nm thick hBN lying on a SiO_2 substrate, following the recipe of Ref. [70]. Then, the same fabrication steps were repeated as before to fabricate circular graphene holes. Figure 3.3C shows an AFM topography image of SL graphene on hBN after 5 h of remote H plasma exposure. Clearly, very regular and well aligned hexagonal holes are visible, indicating a highly anisotropic etch. Etching of the hBN substrate by the H plasma was not observed, see profiles in SOM. We observed this anisotropic SL graphene

etching on hBN in more than 10 samples demonstrating the high reproducability of the process.

In Figure 3.3D we present an AFM topography image of a BL graphene flake on hBN which was exposed to the H plasma for 22 h. We observe anisotropic etching of the BL flake with a slightly higher etch rate for the top layer (~ 0.3 nm/min) compared to the bottom layer (~ 0.2 nm/min), leading to a staircase-like structure at the etch pit borders. As seen in Figure 3.3D, the hexagons in the bottom and the top layer are of the same orientation. We note that the bottom layer is on hBN while the top layer is laying on graphene. The situation of the top layer is comparable to the SL etching on a graphite surface, where it was shown that the edges of the hexagons are aligned with the zigzag direction of the graphite lattice [116, 117]. Since the bottom layer exhibits hexagons oriented in the same direction as the hexagons emerging on the top layer, this further confirms that the etching of SL graphene on hBN is yielding etch pits oriented along the zigzag direction. The ribbon defined by the two left hexagons in Figure 3.3D has a width of about 20 nm, demonstrating the fabrication of nanoscale graphene structures with a remote H plasma.

The size of the SL hexagons as a function of exposure time is shown in Figure 3.4D. A linear fit (dashed red) is clearly over estimating the etch rate for long exposure times, deviating from the data by several standard deviations for the longest times. This hints towards either an insufficient H atom collection mechanism as the etch pits are growing larger or an aging effect of the tube as discussed above.

Raman spectroscopy on SL and BL samples on hBN was performed before and after H plasma etching. The D and D′ disorder peaks were not seen (see SOM), both before and after H plasma etching. This suggests that neither defect formation nor hydrogenation [127, 176–178] is occurring in the bulk 2D during plasma etching, taking into account the annealing of the sample during the cool down phase [176], opening the door for high quality electrical properties.

The EBL defined circles stand very clearly visible in the center of the hexagons as an

elevated region, as seen in Figure 3.3C and D, growing in height but not diameter upon further H plasma exposure. These discs appear also away from the graphene flakes directly on the hBN, wherever circles were EBL/Ar/O_2-plasma defined. However, these elevated regions are also observed to shrink in height in ambient conditions. For a better understanding of the composition and behaviour of these surface structures, further investigations are required, which are however beyond the scope of this work. In addition, the adhesion between graphene and hBN often appears to be rather poor. Graphene flakes of several micrometres in length seem to be tilted with respect to the circular pillars induced by EBL. AFM tip forces or elevated temperatures may have shifted the flakes from their original position [179, 180].

3.4 Conclusions

In conclusion, we have investigated the pressure and distance dependence of the anisotropic etching of graphite surfaces in a H plasma. We have found that the etching characteristics can be divided into two regimes, the remote and the direct plasma regime. In the remote region of the plasma ($d' > 0$) etching only occurs at preexisting defect sites whereas for $d' < 0$ new defects are induced. Further, we have prepared SL and BL graphene flakes on SiO_2 and hBN substrates and exposed them to the remote H plasma. We observed isotropic etching of SL graphene on SiO_2, whereas on hBN it is highly anisotropic, exhibiting very regular and symmetric hexagonal etch pits. BL graphene, on the other hand, did not show a substrate dependence of the etching character and was anisotropic for both substrates.

By inducing artificial defects by lithographic means it becomes possible to pattern graphene nanostructures of various geometries with clean crystallographic edges defined by the etching in a remote H plasma. This leads to the opportunity to fabricate GNRs with well defined edges on a well suited substrate for electronic transport experiments, such as hBN. It would be interesting to study the etching process in dependence of the graphene electrochemical potential, which can be adjusted in-situ with a back gate

during the etching process. Also, a remote nitrogen plasma [181] could be investigated to be potentially used in a similar way to define armchair edges via anisotropic etching of atomic nitrogen.

3.5 Methods

A pure H plasma was created in a quartz tube through a matching network by a 13.56 MHz radio frequency (RF) generator at a typical power of 30 W. See Figure 3.5 for a sketch of the setup. This RF power was capacitively coupled to the 80 mm diameter tube by an outer electrode acting as a surfatron [182]. The pressure was regulated using a needle valve for 20 SCCM H gas flow of purity 6N. The sample was placed at a distance d from the end of the surfatron, was electrically floating and a three-zone furnace controlled the temperature T. The ion impact energy is roughly the difference between the plasma potential and the floating potential and is around $10-15$ eV with an average ion mass of 2 amu. We estimate the ion flux to be significantly lower than 10^{15} ions/cm^{2}s measured for a similar plasma setup but at lower pressure [178]. In order to characterize and optimize the anisotropic etching process, we studied the influence of pressure, distance, and temperature on the etching process, generally finding good repeatability.

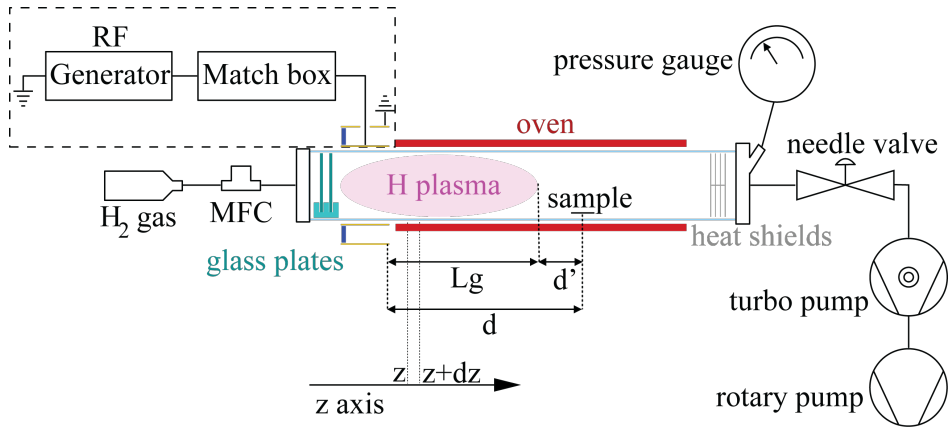

Figure 3.5: Setup of the plasma furnace. The quartz tube has a length of ca. 1 m and a diameter of 80 mm (drawing not to scale).

3.6 Supplementary Information

3.6.1 Direct and remote plasma region

In Figure 3.6, AFM scans acquired after exposure of natural graphite samples for 1 hour to a pure hydrogen (H) plasma at a power of 30 W depict the influence of the pressure and distance on the etching strength and type. For every pressure and distance combination a new graphite sample was fabricated as described in the main text. The matrix representation of the AFM scans of the complete set of investigated parameters remarkably demonstrates the transition from soft anisotropic etching (above or to the right of the cyan line) including only H atoms, to strong etching parameters (below or to the left of the cyan line) comprising also ions. The separation between the two regimes is based upon the size distribution of the hexagonal pits as ions are expected to induce defects acting as new etch sites throughout the whole exposure time. Lowering the pressure as well as decreasing the distance has the effect to increase the number of holes as well as the size distribution and depth of the etch pits, demonstrating an increase of the reactive particle density. On some of the AFM images, unintentional growth or deposition of some additional nanostructures such as worms or particles is seen, e.g. $d = 42\,\mathrm{cm}$ and $p = 1.4\,\mathrm{mbar}$ or $p = 0.7\,\mathrm{mbar}$. For all AFM scans shown in Figure 3.6, the number of holes and their respective diameters are evaluated and plotted in histograms shown in Figure 3.7, describing a comparable picture as the AFM topography scans. Again, not only the amount of holes but also the width of the diameter distribution shows a strong dependence on pressure and distance. As for the AFM scans, the remote (upper right) and the direct (lower left) plasma region can be distinguished using the widths of the distributions in the histograms. In the lower right panels we estimated the number of holes for each diameter to > 12 and the width of the diameter distribution to be at least 600 nm, since an exact investigation of the hole number and diameter was not feasible (see Figure 3.6).

The number of hexagons etched into the graphite surface as well as the width of the

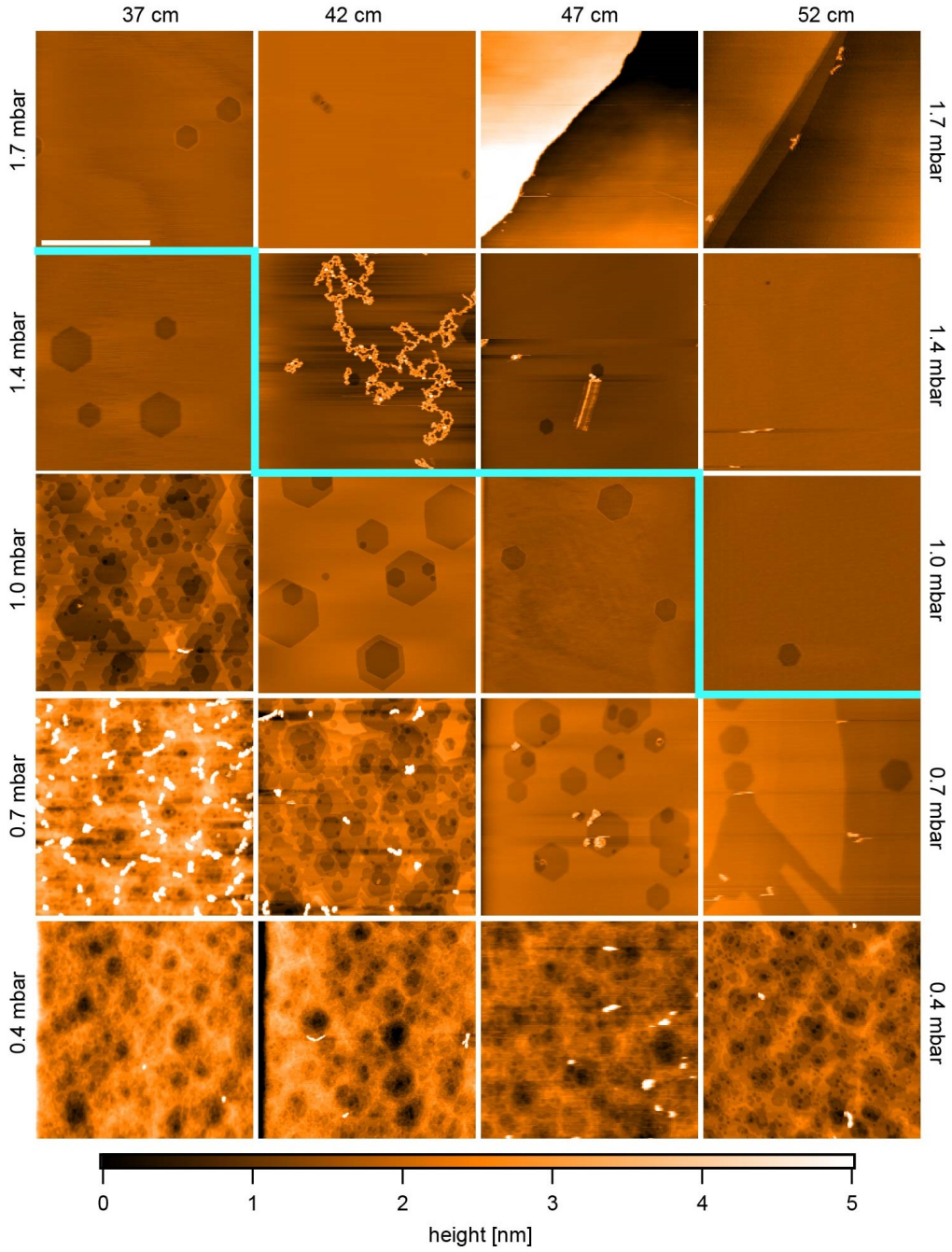

Figure 3.6: Distance and pressure dependence of graphite plasma exposure. AFM topography scans at all parameters investigated in Figure 3.1. All AFM images are $2 \times 2\,\mu\mathrm{m}^2$ in size. The cyan curve marks the transition from the remote (upper right) to the direct (lower left) plasma region. On some surfaces, particles are visible which probably are amorphous carbon residues, either grown or deposited during the etching process (see AFM scans for $p = 0.7\,\mathrm{mbar}$ and $d = 37\,\mathrm{cm}$ or $p = 1.4\,\mathrm{mbar}$ and $d = 42\,\mathrm{cm}$).

hole diameter distribution reflect the number of ions inducing defects on the graphitic surface, assuming a low intrinsic defect density on the surface of the graphite samples.

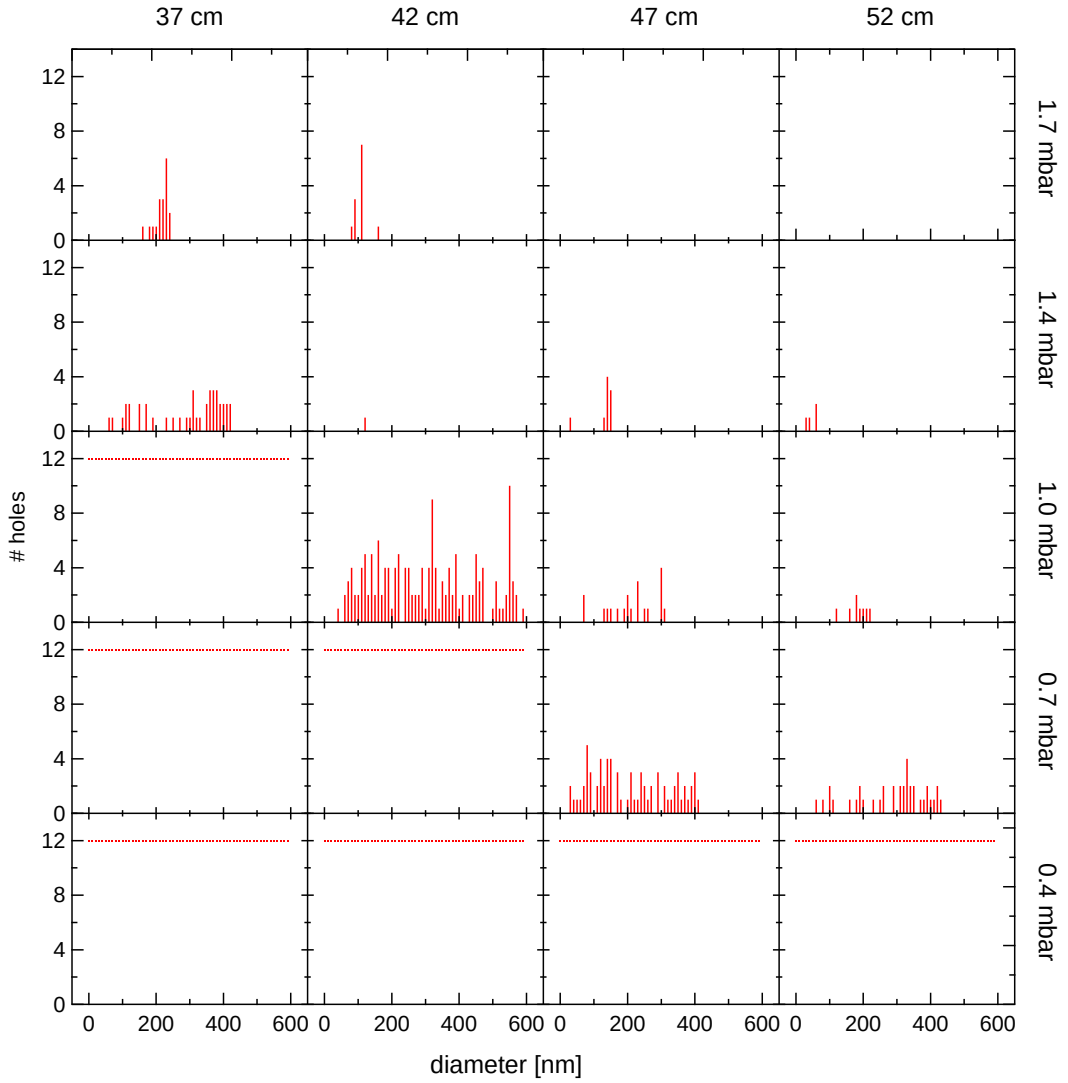

Figure 3.7: Distance and pressure dependence of graphite plasma exposure. Histograms (10 nm bin size) showing the number of holes for all pressure and distance parameters corresponding to Figure 3.6, obtained from $10 \times 10\,\mu\text{m}^2$ AFM scans. For AFM scans of strongly etched surfaces, we plot 12 holes for every hole diameter.

3.6.2 Exponential decay of reactive particles

The number of holes (purple) and the width of the diameter distribution (orange) is shown in Figure 3.8 against the distance between the plasma edge and the sample, $\mathrm{d}' = d - L_g$. For $\mathrm{d}' < 0$ the sample is directly exposed to the glowing plasma, hence experiencing the impact of ions perforating the graphite surface with uncountable, several layers deep holes. For $\mathrm{d}' > 0$ on the other hand, the hole number and the width of the hole distribution both appear to roughly decay exponentially with larger

sample-plasma distance, with an 1/e decay length of $\sim 5\,\mathrm{cm}$ extracted from a fit to an exponential (dashed lines).

The radical concentration is decaying exponentially when moving down the axis of the tube, and is given by [168, 174]

$$[H] = [H]_0 \cdot \exp\left(-a\sqrt{p}d'\right) \tag{3.1}$$

with sample-plasma edge distance d', concentration $[H]_0$ at $d' = 0$, pressure p, and the geometrical factor a:

$$a = \sqrt{\frac{v_{therm}\gamma}{R \cdot D'}}. \tag{3.2}$$

Here, $v_{therm} = \sqrt{8k_BT/(\pi m)} \approx 2'750\,\mathrm{m/s}$ is the molecular H_2 thermal velocity, with Boltzmann constant k_B, hydrogen mass m and temperature T. The material dependent recombination coefficient [168, 174] of the radicals is $\gamma \approx 7.5 \cdot 10^{-4}$, $R = 4\,\mathrm{cm}$ is the radius of the quartz tube and $D' = 7.39\,\mathrm{atm\ cm^2/s}$ is the temperature dependent diffusion coefficient taken here at $\sim 700\,\mathrm{K}$ from Ref. [183, 184]. Note the explicit pressure dependence of the decay length. Here, this results in a decay length of $\approx 12\,\mathrm{cm}$ at $p = 1\,\mathrm{mbar}$, which is consistent with our data. As mentioned in the main manuscript, the recombination of the radicals in the gas phase is expected to be irrelevant and the radicals only recombine at the surface of the quartz tube for the pressure range $p \sim 1\,\mathrm{mbar}$ used here.

3.6.3 Raman measurements before and after plasma exposure

The influence of the H atoms on the graphene quality was further investigated by performing Raman measurements before, after 3 h and after 5 h of plasma exposure, as shown in Figure 3.10. To compare the Raman traces, we subtracted the background before normalizing the traces with the graphene G peak height at $\approx 1582cm^{-1}$. The Raman scans taken on the bare hBN substrate in panel D are normalized to the SiO_2 peak (not visible) to allow comparison. All Raman measurements presented in this

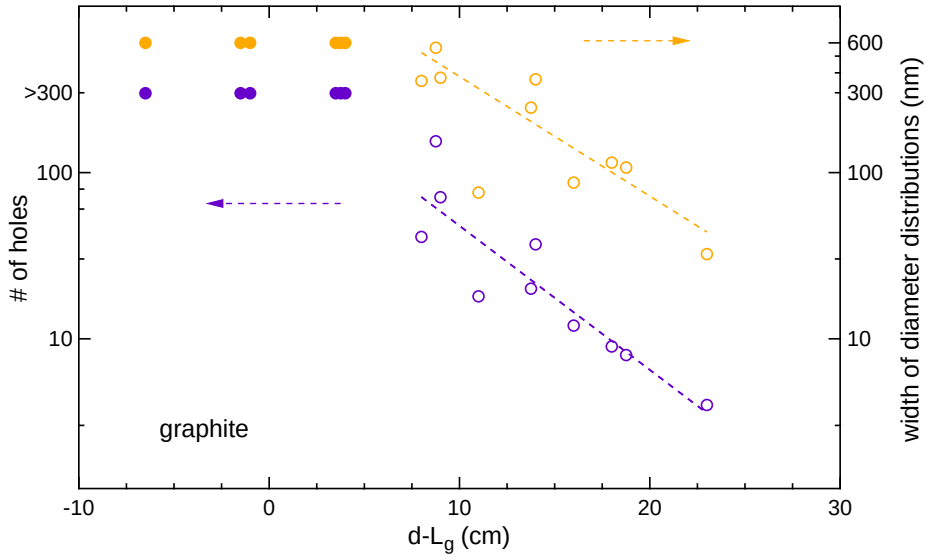

Figure 3.8: Number of holes (purple, left axis) and width of diameter distribution (orange, right axis) as a function of effective distance $d' = d - L_g$.

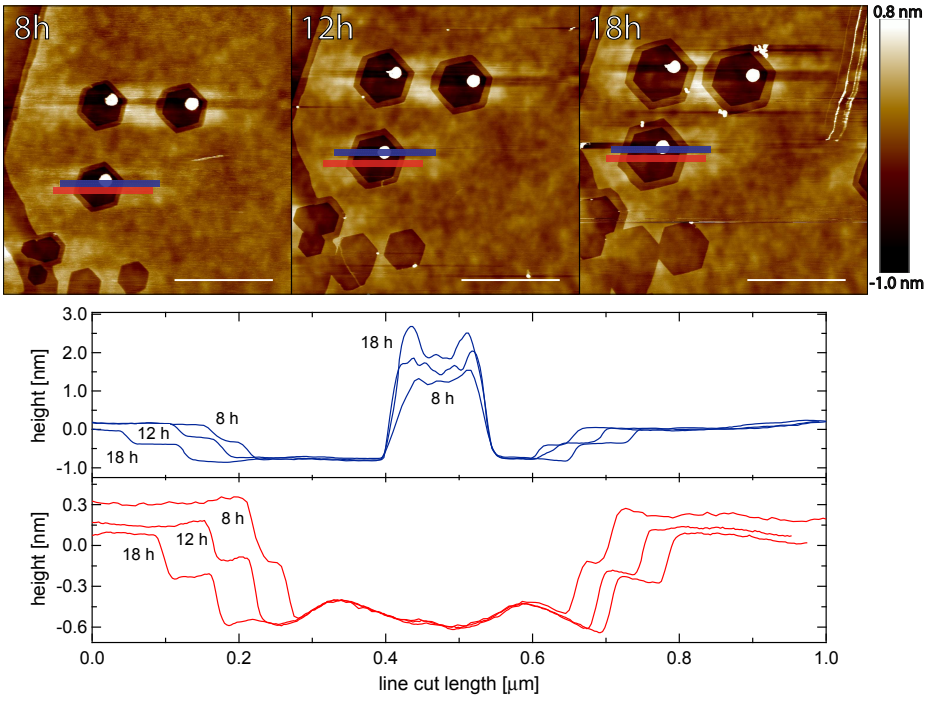

Figure 3.9: AFM images of BL graphene on an hBN substrate. Time series after 8 h, 12 h and 18 h of remote H-plasma exposure (upper panel). AFM profiles (lower panel) taken along paths indicated in upper panel (color coded). Averaging over the vertical range as indicated by the finite vertical width bars in the upper panel is performed to obtain an improved signal. These cuts demonstrate that the hBN substrate is not etched by the H-plasma, since the graphene step height is independent of exposure time. The center pillar appears to be growing with exposure time.

work were acquired with a green laser with a wavelength of $\lambda = 533\,\mathrm{nm}$, where the bulk hBN E_{2g} peak at $1366\,\mathrm{cm}^{-1}$ and the graphene D-peak at $1350\,\mathrm{cm}^{-1}$ are close to each other. Nevertheless, in many cases a weak D-peak can still be reliably extracted.

Panel D shows Raman spectra of the hBN flake before (yellow), after 3 h (blue) and after 5 h (red) of remote H plasma etching. The hBN E_{2g} peak [185] shape, height and position does not significantly change, indicating no or only insignificant interaction of the hBN with the H plasma. Panel E shows Raman spectra acquired on bulk graphene, again before (yellow), after 3 h (blue) and after 5 h (red) of H plasma etching. We did not observe a D-peak in the bulk of the graphene flakes even after 15 h of plasma etching (not shown), indicating no induction of defects or hydrogenation of our samples [127, 176]. Note that after the end of the plasma exposure, the samples are annealed in vacuum while the oven is cooling down from process temperature to room temperature.

Significant information about the type and quality of edge can in principle be obtained from Raman spectra of the graphene edge [109]. However, care needs to be taken to not overheat and possibly reconstruct or otherwise change the edge with the laser [186] when illuminating the graphene edge on SiO_2 at a laser power of 1.5 mW or more. Our spectra do not meet these low power requirements. The damage threshold for graphene on hBN is not known, and study of these effects goes beyond the scope of this work.

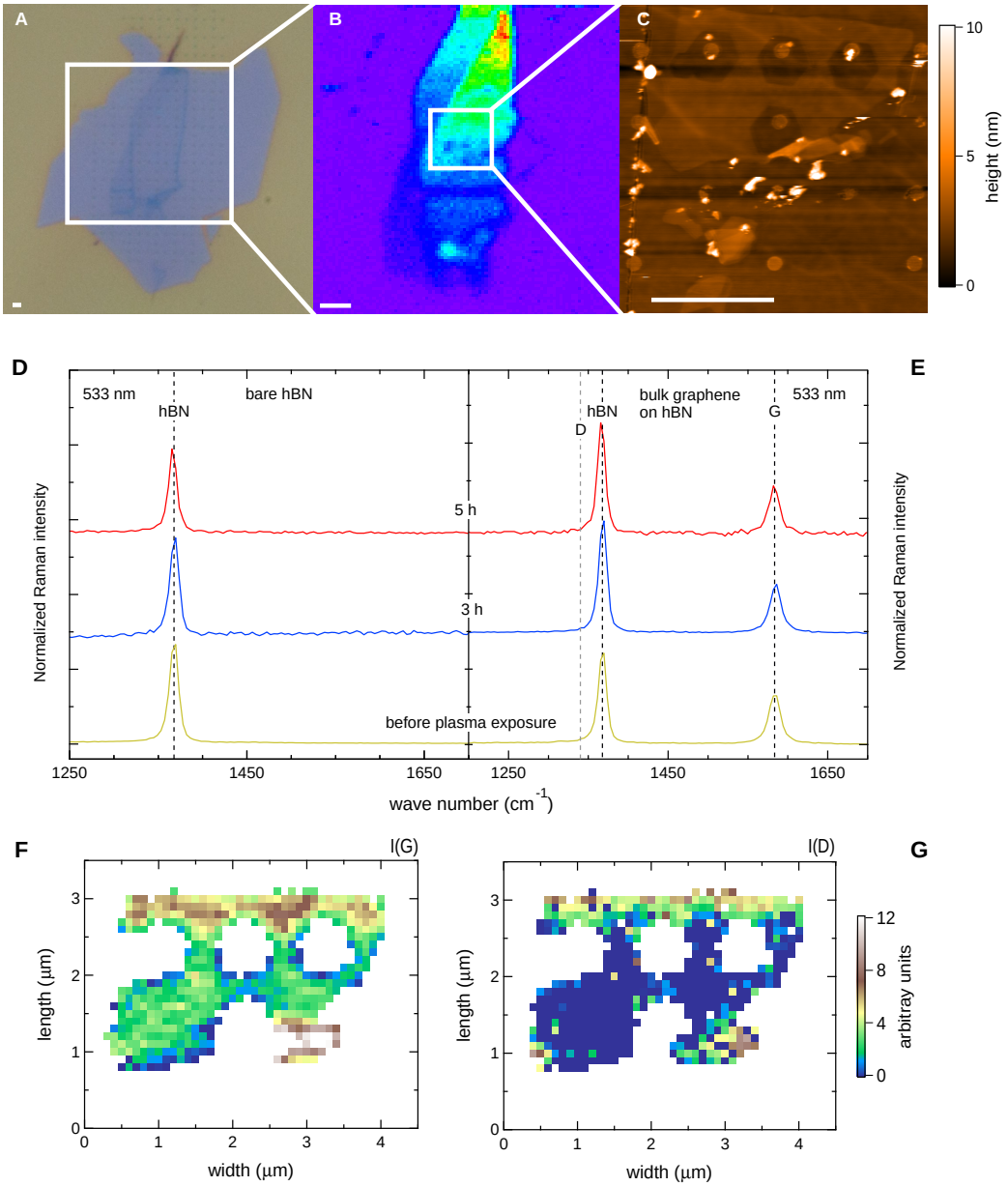

Figure 3.10: Raman spectra and spatially resolved Raman scans of the hBN sample in the main paper. Panel A: optical image of a graphene on hBN sample. Panel B: Raman map of the 2D peak of the same graphene flake before H plasma exposure. Panel C: AFM topography scan showing the region where the Raman single spectra were taken. The scale bars in Panel A to C are 2 μm. Panel D and E: Raman spectra of the bare hBN flake (panel D) and bulk graphene on hBN (panel E) before (yellow), after 3 h (blue) and after 5 h (red) of remote plasma exposure. The Raman spectra are vertically shifted for clarity. Panel F and G: 2D maps of the G peak (panel F) and D peak (panel G) of the flake region shown in panel C.

4 Characterization of Graphene edges defined with Remote Hydrogen Plasma

Y.B. Kalyoncu*, M.K. Rehmann*, M. Kisiel, F. Müller,

E. Meyer, and D.M. Zumbühl

Department of Physics, University of Basel, CH-4056 Basel, Switzerland

N. Pascher

Nanosurf AG, Graeubernstrassse 12, 4410, Liestal, Switzerland

F.J. Giessibl

Department of Physics, University of Regensburg, 93053 Regensburg, Germany

K. Watanabe and T. Taniguchi

National Institute for Material Science, 1-1 Namiki, Tsukuba 305-0044, Japan

Ming-Hao Liu

Department of Physics, National Cheng Kung University, Tainan 70101, Taiwan

This chapter is prepared for publication.

*These authors contributed equally to this work.

4.1 Abstract

We investigate the quality of hydrogen plasma defined graphene edges by Raman spectroscopy, atomic resolution AFM and low temperature electronic transport measurements. The exposure of graphite samples to a remote hydrogen plasma leads to the formation of hexagonal shaped etch pits, reflecting the anisotropy of the etch. Atomic resolution AFM reveals that the sides of these hexagons are oriented along the zigzag direction of the graphite crystal lattice and the absence of the D-peak in the Raman spectrum indicates that the edges are high quality zigzag edges. In a second step of the experiment, we investigate hexagon edges created in single layer graphene on hexagonal boron nitride and find a substantial D-peak intensity. Polarization dependent Raman measurements reveal that hydrogen plasma defined edges consist of a mixture of zigzag and armchair segments. Furthermore, electronic transport measurements were performed on hydrogen plasma defined graphene nanoribbons which indicate a high quality of the bulk but a relatively low edge quality. These findings are supported by tight-binding transport simulations. Hence, further optimization of the hydrogen plasma etching technique is required to obtain pure crystalline graphene edges.

4.2 Introduction

Graphene edges play an important role in many physical phenomena [34, 40]. In particular, the edge shape defines the electronic properties of graphene nanoribbons (GNRs). Crystallographic edges of the armchair (AC) type are predicted to enable the creation of helical modes and Majorana fermions [51] and to be excellent candidates for the implementation of spin qubits [154]. For pure zigzag (ZZ) edges, edge-magnetism was predicted to emerge which can be used for spin filtering[13]. For these effects to be observable in experiment, high quality edges are necessary because edge disorder suppresses magnetic correlations [12] and leads to electron localization which complicates transport studies[50, 57, 58, 159–161]. It has been observed, that GNRs fabricated by ebeam lithography and reactive ion etching (RIE) in an Ar/O_2 plasma have a high degree of edge disorder [57, 58, 159–161]. Hence, other approaches to create GNRs with high quality edges are pursued such as carbon nanotube unzipping [81–83], ultrasonication of intercalated graphite [78], chemical bottom up synthesis[93, 97], anisotropic etching by nickel nanoparticles[103], anisotropic etching during CVD processing [110–113], or carbothermal etching of graphene sheets[108, 109, 162, 163]. Another promising approach which was considered to create high quality crystallographic graphene edges is to employ a hydrogen (H) plasma to perform anisotropic etching of graphite and graphene[15, 116–120, 122, 123, 164, 187].

In this study, we characterize H plasma defined graphene edges on graphite and single layer (SL) graphene on hexagonal boron nitride (hBN) by means of atomic force microscopy (AFM), Raman spectroscopy and low temperature electronic transport measurements. We find high quality ZZ edges on graphite surfaces, manifested by the absence of the D-peak in the Raman spectrum[132, 188]. In contrast, SL graphene on hBN edges exhibit a large D-peak which is indicative of the presence of edge disorder and AC segments. In comparison, the D-peak intensity measured at H plasma defined edges is twice as large as on edges created with RIE. Polarization dependent Raman measurements reveal an edge configuration which consists of approx. 60 % ZZ and

40 % AC segments. Moreover, electronic transport measurements performed across a pnp junction of a H plasma treated graphene flake exhibit Fabry-Pérot oscillations, reflecting the high electronic quality of the bulk graphene flake after H plasma exposure. However, at high magnetic field valley-isospin oscillations appear and indicate a rather low edge quality. In a second device we investigate transport through narrow GNRs with RIE defined edges and H plasma defined edges and find comparable mobilities for these two edge types.

The results from the Raman experiments and the electronic transport studies give a consistent picture, indicating the presence of disorder at H plasma defined graphene edges and thus the need for optimization of the etching process to enable the creation of high quality ZZ edges.

4.3 Results and Discussion

4.3.1 High Quality ZZ Edges on Graphite.

In a first step of the experiment, we intend to visualize the edge of a hexagon created by H plasma exposure, to learn its crystallographic direction and its atomic configuration. Therefore, we record topography and force images by means of ambient qPlus based atomically resolving AFM[189] (Figure 4.1 a) - c)) on a graphite surface which shows several hexagons. In panel a) we show one corner of a hexagon, and its edges are demarcated with white dashed lines. From a) to c), black squared regions are scanned with higher resolution with the same sample orientation. Figure 4.1 c) is a constant height atomic resolution force image of the graphite surface close to the edge and the hexagonal lattice structure is superimposed on the image. The green dashed line in panel c) is drawn parallel to the white dashed lines in panel a) and b). This picture clearly shows that the edge is in parallel to the ZZ direction, in agreement with recent findings [117]. Although the above discussed AFM measurements allow to unambiguously assign the macroscopic edge orientation of the hexagons to the ZZ

direction, thermal drift hindered to position the edge inside the scan range for the atomic resolution imaging, hence it was not possible to actually visualize the atomic configuration of the hexagon edge.

To access information about the edge configuration on the atomic level, Raman measurements are conducted on a graphite flake which was exposed to H plasma under similar conditions as the sample investigated in Figure 4.1 a) to c). 41 Raman spectra are taken over a $5 \times 5\,\mu m^2$ region, covering the whole area as shown in Figure 4.1 d) with the grid of black circles. This web of spectra makes sure that the surface is fully covered. The resulting 41 spectra are laid on top of each other in panel e). These 41 spectra are essentially the same; in particular, the G and 2D-peaks fit to each other and there is no D-peak as seen in Figure 4.1 e). The absence of the D-peak in any of these spectra indicates high quality ZZ edges since any edge disorder would result in some D-peak intensity[132–134, 188, 190].

4.3.2 Raman Spectroscopy on SL Graphene Hexagons on hBN.

Next, we investigate the edge quality of hexagons created in SL graphene flakes on a hBN substrate. In a previous work [122], we showed that the character of the etch is substrate dependent and that it is also possible to get highly anisotropic etching if SL graphene is placed on a hBN substrate. However, it remains unclear how good the edge quality is on a microscopic level. To find out, we prepare a SL graphene flake on a hBN substrate and etch it for 4 h in a remote H plasma to perform Raman measurements at the created graphene edges.

Figure 4.2 a) shows an AFM height image of a SL graphene flake on a hBN substrate. The two darker disks are induced defects which we fabricated by means of ebeam lithography and RIE in an Ar/O_2 plasma. Upon H plasma exposure, they transform into regular hexagonal shaped etch pits. Moreover, smaller hexagons grow next to the two big ones. Those smaller hexagons are either grown from lattice defects already present after exfoliation or induced during H plasma exposure (i.e. by highly energetic

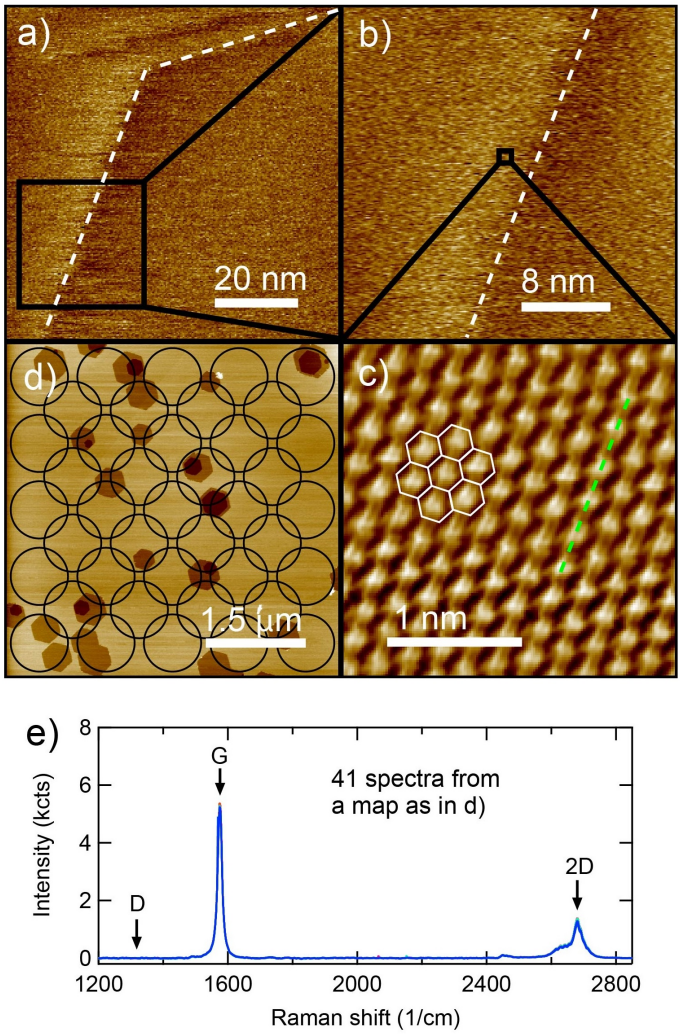

Figure 4.1: AFM maps and Raman spectra of H plasma etched graphite a) AFM height image of a section of a hexagonal shaped etch pit on a graphite flake which was exposed to a remote hydrogen plasma. b) Zoom-in on data shown in panel a). c) Atomic resolution AFM force image of the black squared region in b). The graphene lattice is superimposed in white. The green dashed line indicates the ZZ direction and is parallel to the hexagon edges (white dashed lines in a) and b)). d) Tapping mode AFM image of a $5 \times 5\,\mu m^2$ area of a graphite flake. The black circles with a diameter of 800 nm, given by the laser spot size, indicate the locations at which Raman spectra were taken. e) 41 Raman spectra laid on top of each other.

ions). To learn about the edge quality of such SL graphene edges, we record Raman spectra at the locations indicated by the red and green dashed circles in a) and show them in panel b). We observe the graphene related G and 2D-peaks and the hBN peak coming from the substrate. More importantly, the graphene D-peak appears to the left of the hBN peak at both measurement locations. The difference in intensity could stem from differences of the probed edge segment length. Further, we overlay a

spectrum taken on the graphite sample shown in Figure 4.1 (blue curve). Apparently, there is no D-peak for the graphite case whereas we do observe a D-peak for the SL graphene on hBN edges. This indicates, that there is a significant amount of disorder present at the hexagon edges in SL graphene.

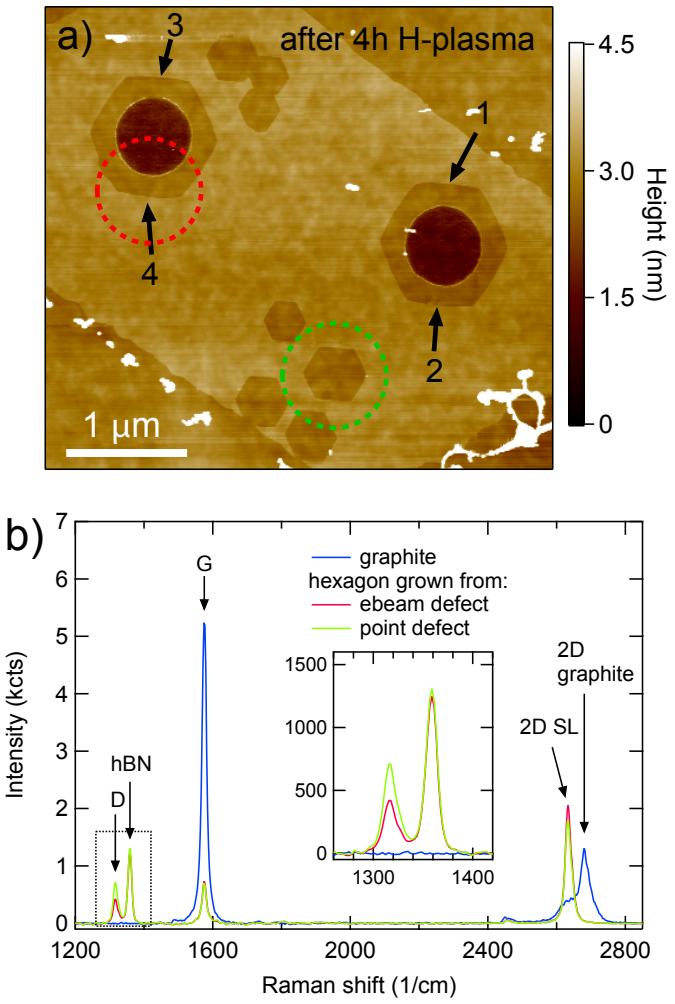

Figure 4.2: AFM height image and Raman spectra of H plasma defined SL graphene edges a) AFM height image of a SL graphene flake on a hBN substrate after 4 h of remote H plasma exposure. Two round shaped defects of a diameter of 600 nm were created by ebeam lithography and RIE etching in a Ar/O_2 plasma. They serve as nucleation centers for the anisotropic etch which transforms them into hexagonal etch pits. Besides the two patterned defects, there are defects which grow into the smaller hexagons visible next to the larger ones. The red and green dashed circles indicate the locations at which the Raman spectra shown in b) were recorded. The black numbers denote the different investigated edge segments of which the measurements are shown in Figure 4.3 f). b) Raman spectra of graphite (blue) and of SL graphene edges encircled by the green and red dashed circles in panel a). The inset shows the region of the D-peak.

Obviously, the hexagon edges created in SL graphene on hBN are of different quality compared to the edges of hexagons formed on graphite. Already in our previous study [122] we have observed that the substrate has a big influence on the etching character. Although hBN as a substrate allows for highly anisotropic etching, the edge configuration on a microscopic level is different from the one on graphite surfaces. This could be due to several reasons, e.g. the different lattice constants of graphene and hBN could potentially lead to strain effects[191] or to the appearance of Moiré superlattice effects [173] which could influence the quality of the H plasma etching process.

4.3.3 Evolution of the Raman D-mode from RIE to H Plasma Defined Graphene Edges.

Next, we study the evolution of the observed D-peak over a time sequence of the etching process. This series of measurements shows how the edge quality evolves from a RIE defined circular hole to H plasma defined edges and further studies the effect of annealing. We started with defining circular holes by means of ebeam lithography and RIE with an Ar/O_2 plasma, which creates disordered edges without any defined crystal orientation [57, 58, 159–161, 192]. The AFM image of this RIE defined circular hole is shown in Figure 4.3 a). Raman single spectra were recorded with circularly polarized light at the bottom edge of the hole indicated by the black dashed circle. Circular polarization ensures that the Raman signal is collected equally at every point of the edge, regardless of the edge direction. After the measurements, the sample is exposed to the remote H plasma first for 2 hours and then 2 more hours, creating hexagonal etch pits of increasing diameter as shown in Figure 4.3 b) and c). As a final step, we annealed the sample in vacuum. After each step, Raman spectra are measured at the same location.

In Figure 4.3 e), four Raman spectra measured at different stages shown in a) to d) are plotted, normalized to the G-peak height. All spectra are averages over five measurements recorded under same conditions and looking all very similar. As expected, the

RIE defined hole shows a D-peak (blue curve). After the first H plasma etching (red curve) the D-peak intensity surprisingly increases approximately by a factor of two and stays at this level for further etching (green curve). Finally, annealing at an elevated temperature of 700 $°C$ again increases the D-peak (black curve), suggesting structural edge defects as the D-peak origin, since annealing likely would reduce, not increase, the amount of edge hydrogenation. We note also that when investigating bulk graphene with Raman spectroscopy, where no edge segments are inside the laser spot, we do not observe any D-peak, consistent with previous work [176], indicating the absence of bulk hydrogenation (see supplementary online material (SOM) S1), though it is in principle possible that annealing at even higher temperatures might be required to remove hydrogen from the edge. The bright circular rim of the RIE defined circular hole on

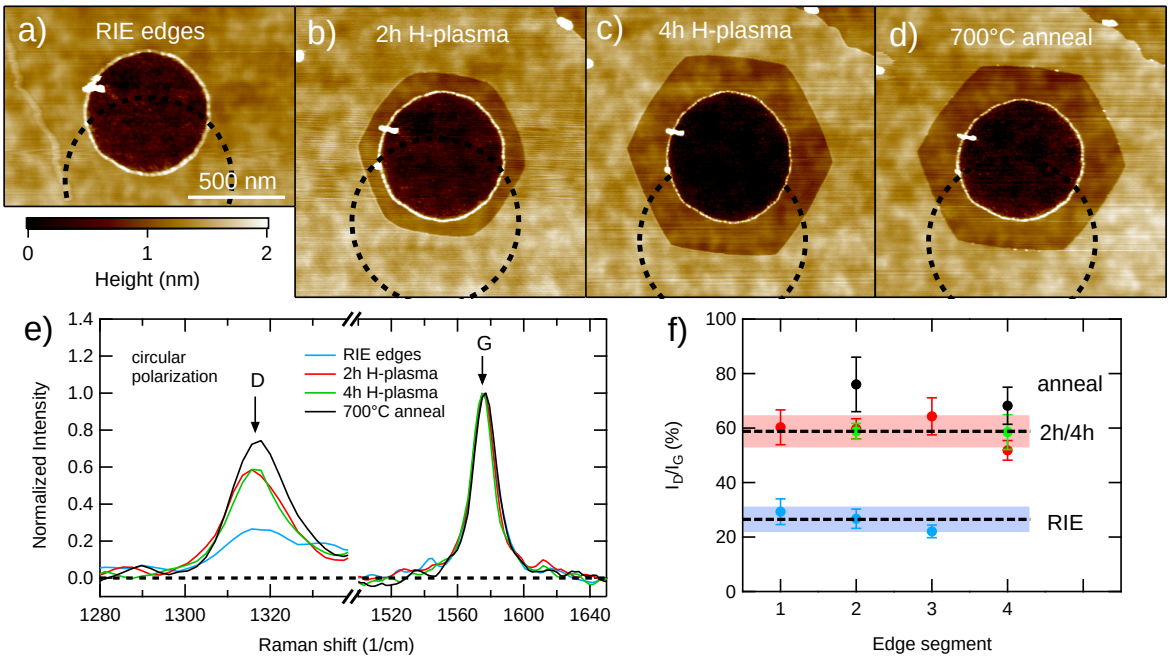

Figure 4.3: Comparison of RIE defined edges with H plasma defined edges a) to d) AFM height images of ebeam defined defects in SL graphene on hBN, after RIE a), after 2 h b) and 4 h c) of remote H plasma etching and after annealing at $T = 700$ for 30 min at a pressure of $1.6 \cdot 10^{-3}$ mbar d). The black dashed circles indicate the spot size of the Raman measurements. e) Raman spectra recorded with circularly polarized light at the bottom edge of the right hole (edge segment #2, see Fig. 4.2 a)) after RIE, 2 h, 4 h and after annealing at $T = 700$. The spectra are normalized to the G-peak and each curve is an average of five measurements. f) Normalized D-peak intensities recorded at different edge segments as labeled in Fig. 4.2 a). The blue and red shaded bands are the standard deviations from all the corresponding measurements.

hBN (Fig. 4.3 b)-d)) does not contribute to the graphene bands in the Raman spectrum (see SOM S1). Further, changes in both graphene area and edge length enclosed in the laser spot are giving negligible contributions to the evolution of the D-peak; see SOM S5 for details. In Figure 4.3 f) we find the same trend in D-peak intensity for all four different edge segments which are indicated in Figure 4.2 a) by the black arrows and numbers. The values for different edge segments stay in a narrow window, giving consistent results.

The increase of the D-peak upon the first H plasma exposure could stem from the formation of AC segments at the edges, since AC edges are highly D-peak active [132–134, 188, 190]. From previous studies[122], it is clear that the direction of the edge generally goes along the ZZ direction. Hence, we conclude that the SL graphene edges on hBN run along the ZZ direction but have a substantial amount of disorder, probably at least partially in form of AC segments. To test this hypothesis, we study the edge disorder with the angular dependence using linearly polarized light [134, 193].

4.3.4 Polarization Angle Dependent Raman Measurements.

Xu and coworkers in Ref. [193] have observed edge reconstruction on ZZ edges due to thermal treatment. Since we etch our samples at a temperature of $T = 400\,^{\circ}C$, it might be that also our graphene edges experience thermal reconstruction. Indeed, it is theoretically predicted that an AC edge has lower energy compared to a ZZ edge[194]. A model to extract the relative abundance of AC-30° segments and point defects was proposed in Ref. [193]. We apply this model to our data and see that the observed D-peak signal only comes from AC-30° segments and that essentially no point defects are present (see SOM S4). Furthermore, Casiraghi et al. in Ref. [134] proposed a theory to calculate the ratio of ZZ segments to AC-30° segments which we apply to our data; see Figure 4.4. Panel a) shows an AFM height image of a hexagon created in SL graphene supported on a hBN substrate. The Raman spectra were recorded at the laser spot indicated by the white dashed circle. The angle θ of the polarization

with respect to the edge is marked in light blue. In panel b) we plot the normalized D-peak intensities as a function of θ. The blue curve is a fit to equation 1 of Ref. [134]. Since our hexagons exhibit rather straight edges, we take an equal amount of +30° and -30° AC segments. We find that our graphene edge consists of about $59 \pm 2\,\%$ ZZ and $41 \pm 2\,\%$ AC-30° segments. This is in excellent agreement with a second data set acquired on a different hexagon on the same graphene flake (see SOM S4 for data taken at different stages of the etching process).

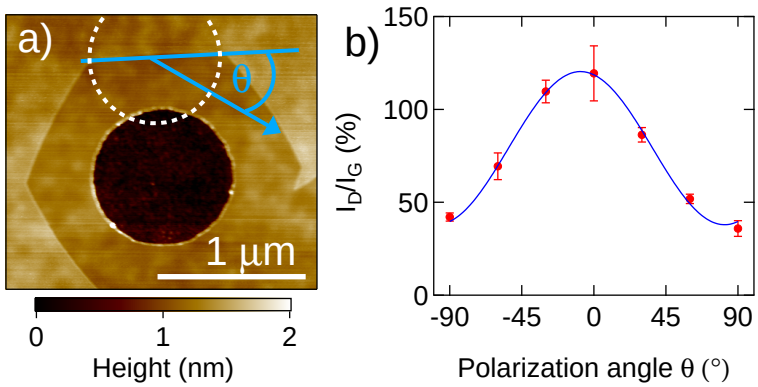

Figure 4.4: Polarization angle dependence of a SL/hBN graphene edge a) AFM height image of a hexagonal etch pit in a SL graphene flake on a hBN substrate after 6 h of remote H plasma exposure. The white dashed circle indicates the laser spot where the Raman spectra were recorded and θ denotes the angle of the laser light polarization with respect to the graphene edge. b) Normalized D-peak intensity for different polarization angles θ. The blue curve is a fit to equation 1 of Ref. [134] yielding $I(D)_{min} = 38 \pm 2$, $I(D)_{max} = 120 \pm 2$ and $\theta_{max} = -8 \pm 1$.

Besides the polarization dependence of the D-peak, the G-peak can also serve to get insight into the structure of graphene edges [135, 136]. In particular, a clean AC edge is expected to exhibit a $\cos^2(\theta)$ dependence and a clean ZZ edge a $\sin^2(\theta)$ dependence. An edge with a mixture of ZZ and AC segments would result in a corresponding mixed angular dependence with a weak amplitude of modulation. This is what is seen in our data and is thus again consistent with a similar mixture of ZZ and AC segments.

4.3.5 Fabry-Pérot Interference in a H Plasma Defined GNR pnp Junction.

Next, we investigate the influence of H plasma treatment on the electronic property of graphene. In particular, we address the quality of bulk graphene and features arising

from the H plasma defined graphene edges. To this end, we fabricate a SL GNR with H plasma defined edges following the ZZ direction of the crystal lattice, done as follows. After a first exposure of the graphene flake to the remote H plasma, a few hexagons grow from which we can learn the crystallographic orientation of the flake. Next, the graphene flake is cut into stripes which run parallel to the hexagon sides and hence parallel to the ZZ direction of the crystal lattice (see Figure 4.5 a)). Subsequently, another H plasma exposure leads to etching from the ribbon edges and thus leaves a GNR with H plasma defined graphene edges. We note that the investigated GNR is free of defects in form of missing carbon atoms, because otherwise these defects would have grown into hexagons (see panel b)). The white dashed rectangle in panel b) indicates the location of the top gate which was fabricated after encapsulation with hBN[73]. In panel c), a schematic of the cross section of the device is shown.

The local top gate and the global back gate allow to tune the charge carrier densities inside and outside the top gated regions independently. This enables the possibility to tune the system into bipolar regimes, i.e. pnp or npn, thus creating two pn junctions which can form a cavity for the charge carriers. If the charge carriers move ballistically inside such a cavity, Fabry-Pérot resonances appear [195]. In panel d), we show the conductance as a function of back gate and top gate voltages in the pnp regime. Clear fringes due to Fabry-Pérot resonances are seen to fan out from the charge neutrality point. The oscillation frequency of the Fabry-Pérot resonances is linked to the cavity length L. We extract values for L in the range of $L = 160\,\mathrm{nm}$ to $330\,\mathrm{nm}$ (see SOM S3 for details about the cavity length extraction). Since L represents a lower bound for the mean free path, we can calculate the corresponding lower bound of the mobility, which is approximately $60'000\,\mathrm{Vs/cm^2}$, reflecting the high electronic quality of graphene after H plasma exposure.

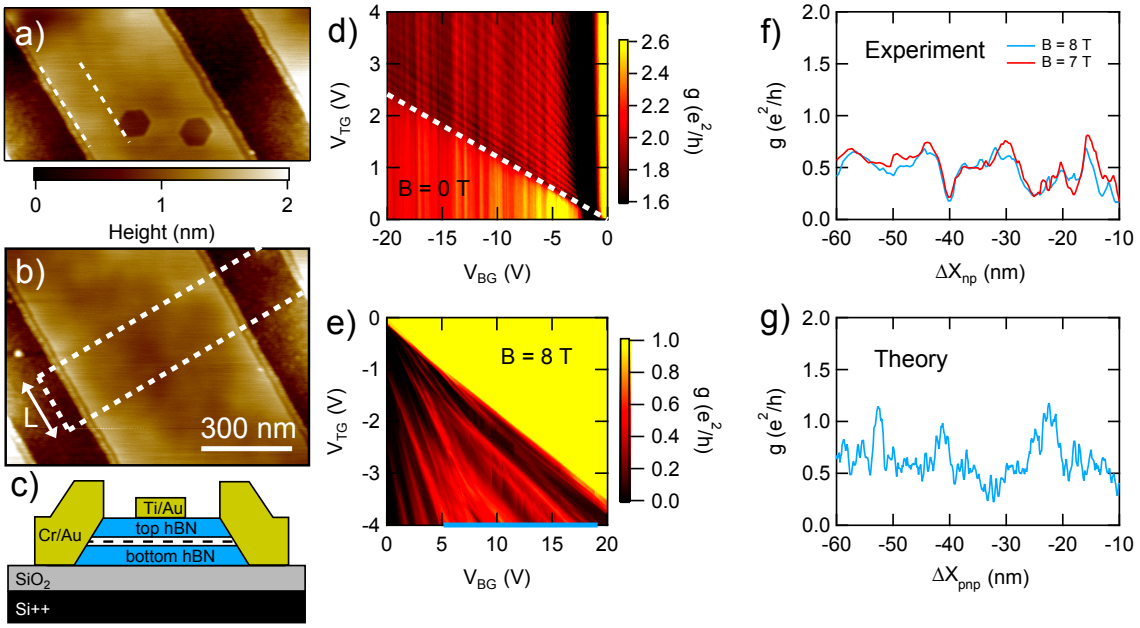

Figure 4.5: Electronic transport measurements of encapsulated GNR with H plasma defined edges a) AFM height image of a SL GNR with remote H plasma defined edges and hexagonal shaped etch pits in the bulk. The white dashed lines indicate that the hexagon edges are well aligned with the GNR edges. b) AFM height image of the GNR on which electronic transport was measured. The white dashed lines indicate the location of the top gate which was evaporated on top of a hBN capping layer and has a width of 200 nm. The GNR is 600 nm wide and measures 1.6 μm in length between the source and drain contacts. c) Device schematic of the encapsulated GNR with a global back gate and a local top gate. The black dashed line indicates the SL GNR. The bottom and top hBN layers have a thickness of 42 nm and approx. 35 nm, respectively. d) Differential conductance as a function of back gate V_{BG} and top gate V_{TG} voltage at $B = 0$ T in the pnp region (n under the top gate). e) Similar map as in d) but recorded at $B = 8$ T and in the npn regime (p under the top gate). In the bi-polar regime, resonances fanning out linearly from the charge neutrality point are visible. f) Cut along the blue solid line in e) and an additional curve recorded at same gate voltages but at $B = 7$ T. The x-axis was converted from back gate voltage to the pn-interface location Δx_{pn}; see SOM S7 for details. g) Calculation of the conductance through a GNR following the ZZ direction with disorder in form of AC-30° segments and a bulk disorder of 35 meV plotted versus the position of the pnp-region ΔX_{pnp}.

4.3.6 Valley-Isospin Dependent Conductance Oscillations in a H Plasma Defined GNR.

These measurements can be repeated at high magnetic field (see Figure 4.5 e)). We follow an analysis based on ref. [196] to study the edge quality in transport. At high magnetic field, the charge carriers move along the edges of the GNR and along the pn-interfaces. With scanning gate voltages one can effectively move the pn-interface along

the edge of the ribbon and in this way scan the edge and probe its disorder [196]. In panel f), we show a cut along the blue solid line in the map of panel e) at $V_{TG} = -4\,\mathrm{V}$ and a similar cut recorded at $B = 7\,\mathrm{T}$, showing that the oscillations already develop at lower field and remain stable as the magnetic field strength is increased. This is a sign that the observed oscillations originate from the valley-isospin physics.

Theoretical expectations for ribbons with one-atom steps at the top edge and zero bulk disorder show a conductance oscillating from 0 to $2\,\mathrm{e}^2/\mathrm{h}$ for the ZZ case (see Figure 4.6 a)) and from 0 to $\sim 1.5\,\mathrm{e}^2/\mathrm{h}$ for the AC case (see Figure 4.6 b)). If a realistic bulk disorder strength of 35 meV (extracted from the experimental data based on the width of the Dirac peaks) is added, the oscillations in the ZZ case collapse to a roughly constant conductance of $\sim 0.6\,\mathrm{e}^2/\mathrm{h}$, whereas the AC case is essentially unaffected by the bulk disorder. We note that the AFM results presented in Figure 4.1 indicate that the edges are following the ZZ direction. Hence, for further calculations we focus on ZZ GNRs with different kinds of edge disorder, as follows. A GNR with disordered edges and generally following the ZZ direction shows fast oscillations with an amplitude of $\sim 2\,\mathrm{e}^2/\mathrm{h}$ for zero bulk disorder. These oscillations are not stable upon 35 meV of bulk disorder and also collapse to a roughly constant conductance of $\sim 0.6\,\mathrm{e}^2/\mathrm{h}$ (see Figure 4.6 c)). An AC ribbon with edge disorder, on the other hand, would retain oscillations with a large amplitude of $\sim 2\,\mathrm{e}^2/\mathrm{h}$ upon a realistic bulk disorder strength [196] (not shown). Our measurements show neither of these behaviors (see Figure 4.5 f)). However, calculations for a ribbon which follows the ZZ direction and with disorder in form of AC-30° segments show oscillations which are relatively robust against a bulk disorder of 35 meV and which look qualitatively similar to the ones found in experiment (see Figure 4.5 g) and Figure 4.6 d)). Hence, these findings are in agreement with what we found in our Raman studies presented above, i.e. SL graphene edges on hBN created by remote H plasma exposure follow the ZZ direction but contain edge disorder in form of AC-30° segments.

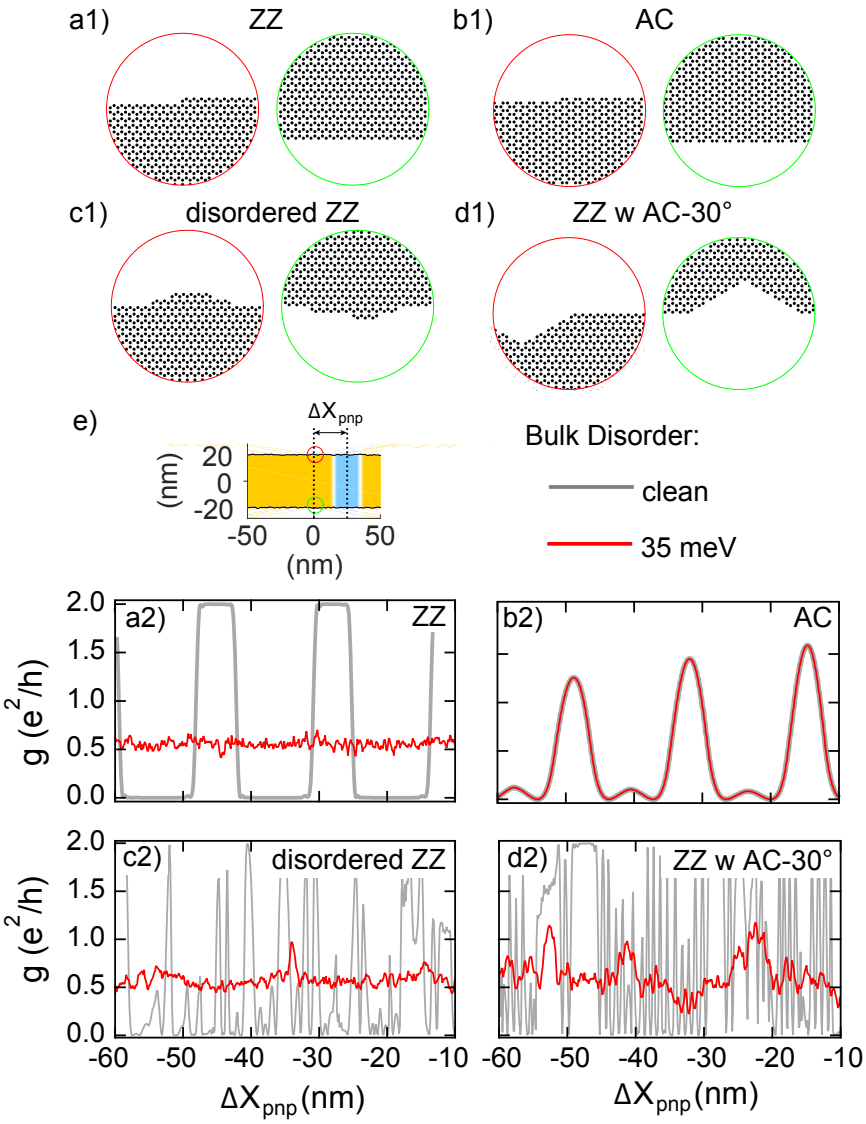

Figure 4.6: Quantum transport simulations a1) Ribbon with a perfect ZZ edge at the bottom and one-atom steps at the top edge. b1) Similar case as in a1) but following the AC direction. c1) Ribbon following the ZZ direction but with a large amount of edge disorder on both edges. d1) ZZ edge ribbon with 40% fraction of randomly distributed AC-30° segments on both sides (as found in experiment) with a depth of 1 nm. e) Sketch of the ribbon model with a pnp junction. The yellow regions are p-doped and the blue region is n-doped. The red and green circles are zoom-ins on the top and bottom edges of the ribbons as indicated in the ribbon model. Panel a2) to d2) show conductance as a function of ΔX_{pnp} for the respective ribbon structures shown in a1) to d1). The blue curves are for zero bulk disorder and the red curves for 35 meV, the value from experiment. Only the ZZ with AC-30° segments case qualitatively agrees with the experiment.

4.3.7 Electronic Transport Through H Plasma Defined Constrictions.

In Figure 4.7, we show transport measurements for narrower and shorter graphene constrictions fabricated in a different way. Prior to encapsulation, we define two round holes of small diameter into the graphene layer with Ar/O_2 plasma and expose these to the remote H plasma to create hexagons sandwiching a GNR with ZZ edges between them, see Figure 4.7 b). Here, the round seed hole is relatively small, only about 100 nm in size, and most of the $\sim$ 500 nm hexagon was etched with the H plasma process in an exposure of about 5 hours. For the Fabry-Pérot sample, in contrast, only a relatively small amount of H plasma etching was performed (about 1 hour), enlarging the Ar/O_2 plasma defined structures only slightly. It would be interesting to compare in transport experiments ribbons with long and short H plasma exposure, even though no time dependence of the edge quality was observed on the Raman samples (see Figure 4.3). It is plausible that longer exposure has a healing effect on the edge, such that it removes defects more efficiently and creates less disordered atomic arrangements. Plus, for longer exposures the ribbon direction is solely determined by the graphene lattice since the etching starts from a round defect and evolves naturally to a hexagon with edges along the ZZ crystal axis. In the Fabry-Pérot sample (short exposure), a small misalignment between the overall ribbon direction and the ZZ crystal axis may remain after the H plasma etching. Also, the ebeam defined circles are clearly visible as an elevated region. Such regions are known to appear after H plasma exposure and have been observed in many samples [122]. However, further investigation is required to better understand these features.

Figure 4.7 shows an example of such a ZZ GNR, with 4-wire conductivity as a function of global back gate voltage plotted in panel a), comparing a H plasma defined ribbon (blue) with a RIE defined ribbon (black). Both ribbons are fabricated on the same graphene flake, allowing direct comparison. As seen, the two curves are very similar, resulting in comparable mobilities, and no plateaus of quantized conductance are clearly evident. We note that for most of the gate voltage range the mean free path is larger

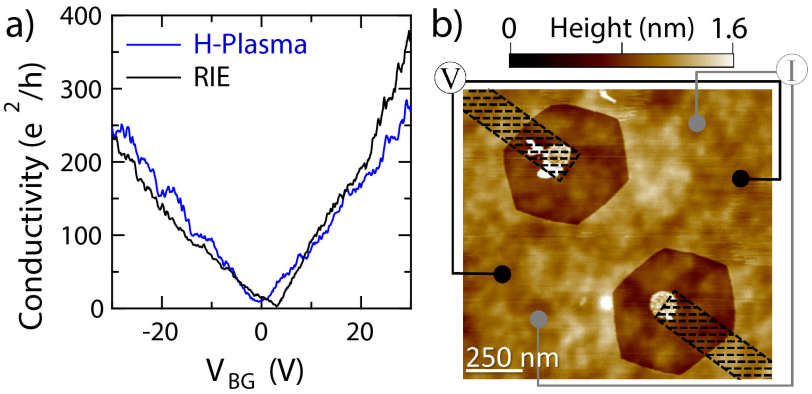

Figure 4.7: a) Four-wire conductivity as a function of gate voltage for two GNRs etched in the same encapsulated sample, fabricated as labeled. A series resistance is subtracted from each curve, consistent with the the number of squares between the ribbon and the contacts ($\sim 200\,\Omega$ for blue and $\sim 400\,\Omega$ for black curve) b) AFM height image of H-plasma etched GNR with a width of $\sim 300\,\text{nm}$. Two Cr/Au edge contacts (not shown) are evaporated on each side of the ribbon after encapsulation and the black dashed regions are etched out to prevent short circuiting of the ribbon.

than 500 nm in bulk, determined from a separate Hall bar sample, see SOM S6. Even though the ribbons are about a factor of 2 shorter than the mean free path, conductance quantization is not observed. Hence the edges are the dominant source of scattering, irrespective of whether they are defined with H plasma or RIE. We note that none of the wiggles seen in these conductivity traces obviously develop into a conductance plateau even under application of a magnetic field.

4.4 Conclusion

In conclusion, we have found that H plasma defined hexagons in SL graphene on hBN exhibit a relatively large D-peak. Polarization dependent Raman measurements revealed an edge configuration consisting of approximately 60 % ZZ and 40 % AC-30° segments. In contrast, H plasma defined hexagons on graphite did not show any D-peak intensity, thus seem to be high quality ZZ edges. Electronic transport measurements on H plasma defined GNRs unveil high electronic quality of the bulk graphene after H plasma exposure, manifested in Fabry-Pérot resonances. We note that the exposure of graphene to the remote H plasma is an excellent cleaning method, since it removes residues very efficiently without degrading the quality of the graphene crystal lattice.

This is confirmed by Raman spectroscopy (no D-peak in the bulk), AFM (very clean surfaces without PMMA residues) and electronic transport measurements (high electronic mobility). However, measurements at high magnetic field show valley-isospin oscillation characteristics which indicate the presence of edge disorder. In particular, quantum transport simulations for a ZZ GNR with AC-30° segments fit the experimental data best and support the findings of the Raman experiments. Moreover, transport through narrow graphene constrictions showed similar mobilities for RIE defined edges and H plasma edges.

Hence, the Raman investigations and the transport measurements both indicate the presence of edge disorder for H plasma defined SL graphene edges. Further investigations are needed to identify possible origins of the disorder such as e.g. hBN-graphene interactions where the relative rotation angle could play a role[173, 197], or a too high thermal energy leading to edge reconstruction[193]. Thus, further optimization of the H plasma etching process is required in order to obtain high quality crystallographic graphene edges.

4.5 Methods

AFM specifications: Two different AFM instruments were used for the measurements presented in this work. The data shown in Figure 4.1 a) to c) was obtained by means of ambient qPlus based atomically resolving AFM[189], namely with a quartz force sensor with resonance frequency $f_0 = 33\,\mathrm{kHz}$, stiffness $k = 1800\,\mathrm{N/m}$ and quality factor $Q = 3000$. Coarse topography images in Figure 4.1 (a) and b)) were acquired in the frequency-modulated mode while Figure 4.1 c) shows an atomically resolved frequency shift image acquired in the constant height mode. The details of the setup are described elsewhere [198]. For all other AFM data a Bruker Dimension 3100 was used. All data measured with this instrument was acquired in intermittent contact mode (amplitude modulated).

H plasma parameters: The following parameters were used for the exposures of all

samples presented in this work: $T = 400$, $p = 1.7\,\text{mbar}$, H_2 gas flow of 20 SCCM. The details of the setup are described elsewhere[122].

Raman microscope: The Raman measurements were acquired with a WITEC alpha300 Raman system. The wavelength of the He-Ne laser was 633 nm and the used objective was 100x with $NA = 0.9$. The laser power was set to 1.5 mW or below for all measurements. This power is low enough to exclude any laser induced structural changes (see SOM S2). To extract the peak heights, we first subtract the background and fit single Lorentzians (for the G and 2D-peaks) and a double Lorentzian for the D and hBN peaks.

Sample fabrication: We used graphite flakes from NGS Naturgraphit GmbH. SL flakes were obtained by the scotch tape method[6] and transferred on top of hBN crystals by the wet transfer technique described in Ref. [70]. High quality hBN crystals[175] were exfoliated on top of a p++ doped Si wafer covered by 300 nm SiO_2 following the same scotch tape method. For the sample in Figure 4.7, we used an hBN flake from HQ-Graphene. After H plasma etching, the electronic transport samples were in addition encapsulated by a top hBN flake to ensure high cleanliness and stability of the devices. To cut the hBN/graphene/hBN stack in order to shape it or define control ribbons an $SF_6/Ar/O_2$ gas mixture was used in an RIE process. Cr/Au side-contacts were fabricated following ref. [73] with an additional RIE step with CHF_3/O_2 gas prior to metalization.

Electronic transport measurements: Standard low frequency lock-in measurements were performed in a variable temperature insert at $T = 4\,\text{K}$.

Quantum transport simulations: All quantum transport simulations are done with the following parameters. Magnetic field is fixed at $B = 16\,\text{T}$, the distance between two pn-interfaces is set to 20 nm, and the smoothness of the pn and np regions is approximately 5 nm. All calculations with disorder are averaged over 200 different configurations of Anderson-type disorder potential. All calculations are done at zero temperature.

4.6 Supplementary Information

4.6.1 High quality bulk graphene after hydrogen plasma exposure

In order to investigate the influence of remote hydrogen (H) plasma exposure on the graphene flake, we recorded Raman maps (see Fig. 4.8). In panel a) and b) we show the integrated 2D- and D-peak intensities, respectively. It is nicely visible, that the D-peak intensity is only high at the edges of the flake and the hexagons and very low in the bulk, showing that exposure of graphene to remote H plasma only edges from defects and the edges and leaves the bulk intact. Furthermore, we can exclude hydrogenation of bulk graphene because this would lead to D-peak intensity [176]. Panel c) shows an AFM height image of the region where the Raman maps in a) and b) were recorded. The green, red and purple crosses are drawn at the same location on the flake through a) - c), namely the green cross lays inside the hexagon, the red cross at the edge and the purple cross on bulk graphene.

Raman spectra were recorded at the location of these crosses and are shown in panel d) with the corresponding color coding. We observe the graphene related D-, G-, and 2D-peaks, as well as the hBN-peak coming from the substrate. Looking at the G- and 2D-peaks, the intensity is highest for the measurement on bulk graphene, decreases to about half the intensity for the measurement at the hexagon edge and almost vanishes for the measurement taken inside the hexagon. Since the laser spot size is on the order of the hexagon size, the G- and 2D-peak intensities do not fully vanish because the tails of the Gaussian beam shape still excite a small fraction of graphene. Interestingly, the D-peak intensity is only high for the measurement taken at the edge and zero inside and outside the hexagon (see panel e) for the zoom-in). This shows, that the rim initially created when the starting defect was fabricated by reactive ion etching (RIE) in an Ar/O_2 plasma does not contribute to the graphene D-band in the Raman spectrum. In Figure 4.8 f) we show the intensity profile of the 2D-peak, recorded along the red solid line in panel a). From this profile we extract a laser spot diameter of $\sim 860\,\text{nm}$. This

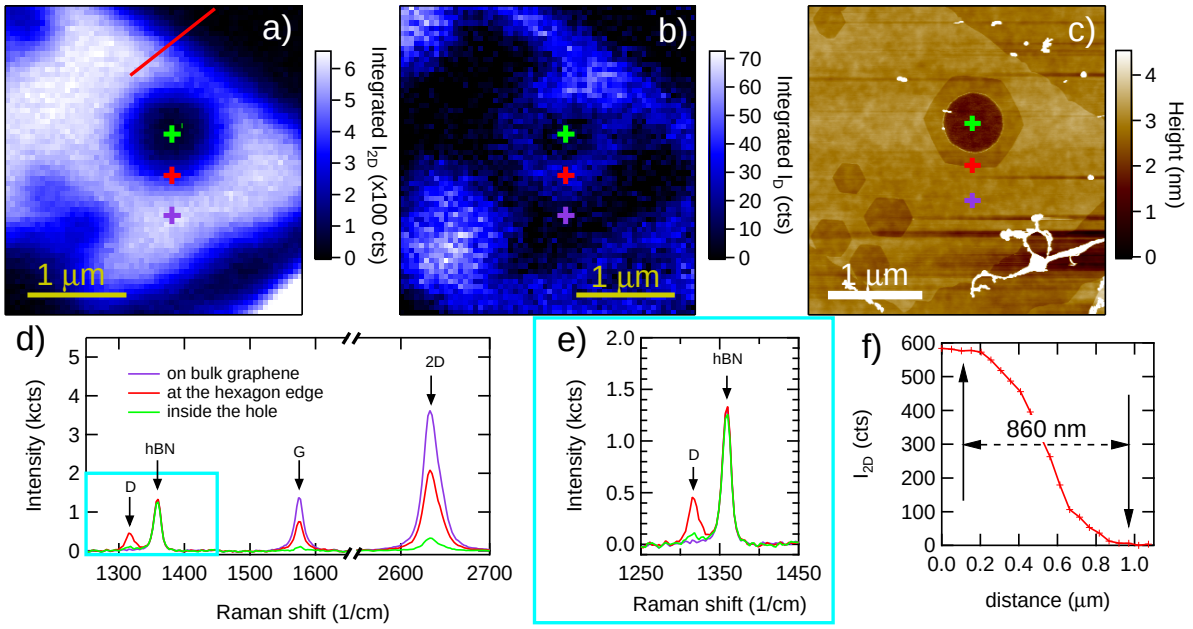

Figure 4.8: High quality bulk graphene after H plasma exposure Integrated 2D-intensity (a)) and integrated D-peak intensity (b)) of a section of a single layer (SL) graphene flake on a hexagonal boron nitride (hBN) substrate after 4 h of H plasma exposure. c) AFM height image of the region where the Raman maps in a) and b) were recorded. d) Raman spectra recorded at the locations indicated by the colored crosses in a) - c). e) Zoom-in on the region of the D-peak. f) 2D-peak intensity as a function of distance measured along the red solid line in panel a).

is well in agreement with the theoretically expected diffraction-limited spot diameter ($1.22{*}\lambda/NA = 858\,\text{nm}$, with the numerical aperture $NA = 0.9$ and the laser wavelength $\lambda = 633\,\text{nm}$).

4.6.2 Laser power test

A crucial condition for the investigation of the edge constitution by means of Raman spectroscopy is that the edge is not changed upon laser irradiation. Indeed it has been observed experimentally[186] that edge reconstruction due to laser annealing can happen at graphene edges. To ensure, that our graphene edges are not altered upon laser irradiation we performed a laser power test. In Figure 4.9 a) we show an AFM height image of the sample on which we performed the laser power test. In panel b) we plot the normalized D-peak intensities measured at different stages of the laser power test (measurement # 1 to 5).

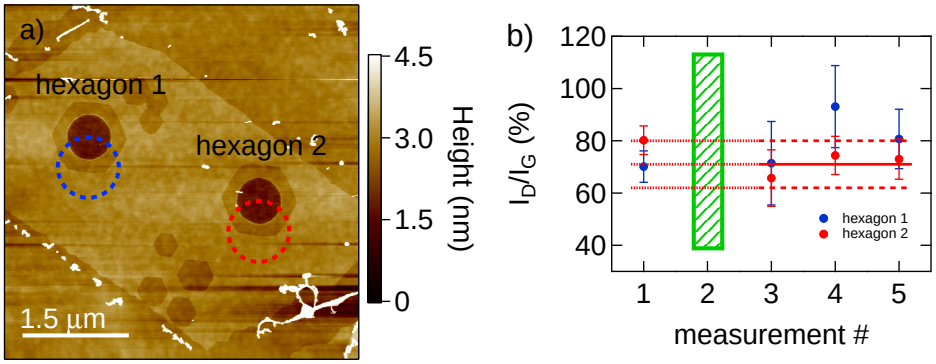

Figure 4.9: Laser power test a) AFM height image of a SL graphene flake on hBN after 4 h of remote H plasma exposure. The blue and red dashed circles indicate the laser spot where the Raman spectra shown in panel b) were recorded. b) Normalized D-peak intensity recorded at different stages of the laser power test. Measurement # 1, 3, 4 and 5 were acquired with a laser power of 0.5 mW. Only hexagon 2 was exposed to a laser power of 1.5 mW, see measurment # 2 (green dashed area indicates exposure to 1.5 mW). The red solid and dashed lines at measurement # 3 to 5 indicate the average and the standard deviations, respectively. They are prolonged to the left across measurement # 1 and 2 and show that the normalized D-peak intensities recorded before and after exposure to 1.5 mW are comparable. All data points are averages over five measurements and the error bars are the corresponding standard deviations.

First we measured at both hexagons with a laser power of 0.5 mW (measurement # 1). In a second step we measure at hexagon 2 with a laser power of 1.5 mW (measurement # 2). After this exposure to 1.5 mW we measure again at both hexagons with 0.5 mW (measurement # 3 to 5). Comparing the normalized D-peak intensities recorded before exposure to 1.5 mW (measurement # 1) with the intensities recorded afterwards (measurement # 3 to 5), it is indicated that measuring with a laser power of 1.5 mW does not change the recorded D-peak intensity significantly and hence the edge is not impaired. Hence we generally measured with a laser power of 1.5 mW to have a reasonable signal to noise ratio.

4.6.3 Extraction of the cavity length

In order to characterize the electronic quality of our H plasma exposed graphene samples, we extract a lower bound for the mean free path l_{mfp} of the charge carriers from the oscillation period of the Fabry-Pérot oscillations which are only visible if l_{mfp} exceeds the cavity length L. In particular, L can be calculated from the charge carrier

density values n of two consecutive oscillations:

$$L = \frac{\sqrt{\pi}}{\sqrt{n_{j+1}} - \sqrt{n_j}} \tag{4.1}$$

In Figure 4.10 we present electronic transport data recorded on the sample presented in Figure 5 in the main manuscript. Panel a) shows the conductance as a function of the inner (n_{in}) and outer (n_{out}) densities, where n_{in} is the density in the top gated area and n_{out} is the density in the graphene which is only influenced by the global back gate. The conductance map can be divided into four regimes: pnp, pp'p, npn and nn'n. In the two bipolar regimes (pnp and npn) pn-junctions are formed which build a cavity for the charge carriers and lead to Fabry-Pérot resonances (see panel b) for a cut along the blue line in a)). Using equation4.1 we extract values for L at different n_{out}, see panel c). The largest cavity sizes are reached for low values of n_{out} and large values of n_{in}. In particular, the values for L lay in the range of 160 nm to 330 nm.

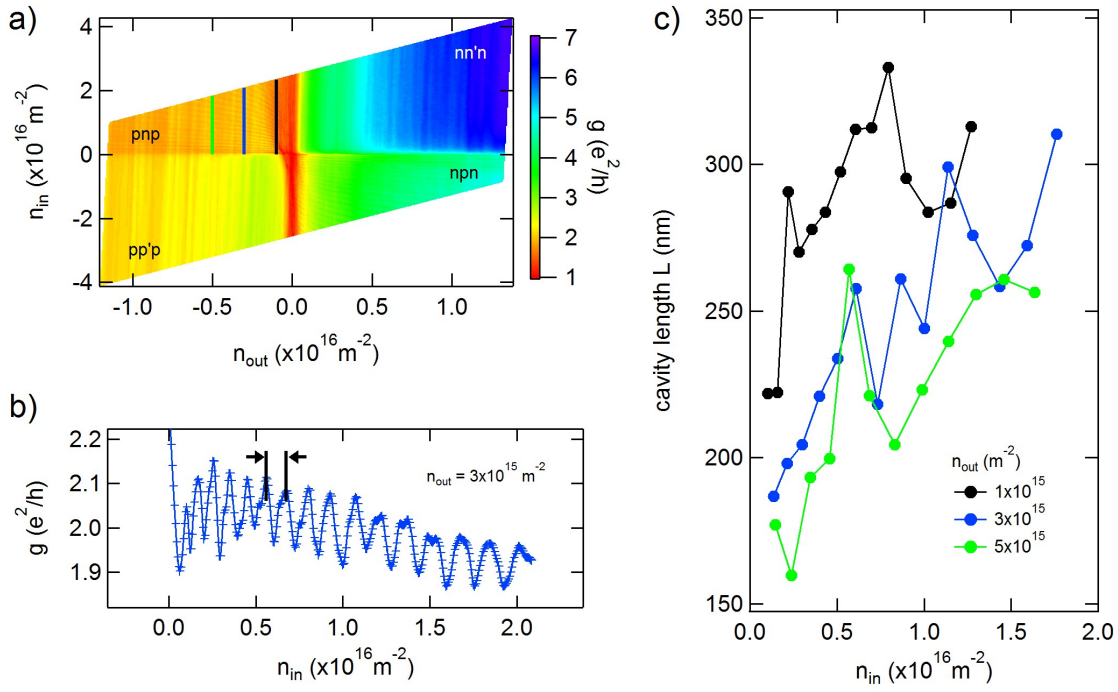

Figure 4.10: Extraction of the cavity length a) conductance as a function of n_{in} and n_{out}. b) cut along the blue solid line in a). Fabry-Pérot resonances are visible indicating ballistic transport between the pn-interfaces. c) Extracted cavity lengths L as a function of n_{in} for three different values of n_{out}.

4.6.4 Edge Reconstruction

Reconstruction of zigzag (ZZ) edges has been observed experimentally [193, 199] and predicted theoretically[194]. Among them, Xu et al.[193] proposed a reconstruction mechanism which leads to four types of edge reconstructions and has the following form:

$$I_D \propto \frac{1}{4} f_1 + f_2 + \frac{1}{2} f_1 cos^2(\theta + \phi) \tag{4.2}$$

where f_1 describes the relative weight of armchair (AC)-30° segments, f_2 are the point defects, f_3 are the ZZ-0° segments and f_4 are the ZZ-60° weights. θ denotes the polarization angle with respect to the edge and ϕ is an offset which could stem from an alignment error. Since only AC-30° segments and point defects are D-peak active, it is possible to learn about their relative abundance (f_1/f_2) by performing polarized Raman experiments. In Figure 4.11 a) we plot the normalized D-peak intensity as a function of θ which was measured at the edge of the hexagon shown in Figure fig:figure4 a) in the main manuscript. The blue curve is a fit to equation 4.2 from which we extract values for f_1 and f_2. The extracted values indicate that AC-30° segments are much more abundant than point defects and hence that the edge essentially consists only of AC-30° and ZZ segments.

In Figure 4.11 b) we plot the ratio of ZZ to AC-30° segments ρ_Z extracted at different stages of the etching process for two different hexagon edges. The extraction of ρ_Z was done following the procedure presented in Ref. [134] as also described in the main manuscript. Within the experimental error bars ρ_Z is similar for all investigated etching times.

4.6.5 Effect of the Hole Shape on the D-peak Intensity

As complementary to the discussion of the etching series presented in Figure 3 of the main manuscript, the geometrical change from the circular hole to the hexagonal hole

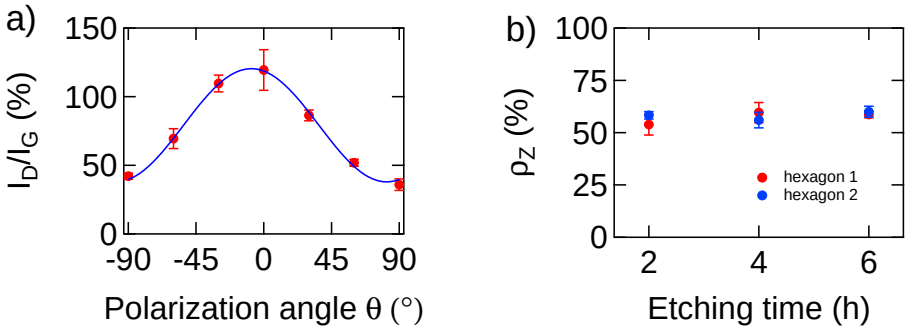

Figure 4.11: Edge reconstruction. a) Normalized D-peak intensity as a function of the polarization angle θ for the hexagon shown in Fig. 4 a) of the main manuscript. The blue curve is a fit to equation 4.2 yielding $f_1 = 165 \pm 6$, $f_2 = -3 \pm 3$ and $\phi = 8 \pm 1$. b) ρ_Z as a function of etching time for two different hexagon edges.

must be taken into account in order to interpret the increase of the D-peak intensity correctly. Naturally, a change in edge length effects the D-peak intensity and the graphene area enclosed in the laser spot affects the G-peak intensity. These geometrical changes must be normalized such that I_D/I_G only manifests the edge quality.

First, we look at the change of the shape from the RIE circular hole to the H plasma etched hexagonal hole. The total edge length enclosed in the laser spot for both shapes are almost equal to each other ($\sim$ 940 nm). But for the total D-peak intensity, it is crucial to consider the orientation of the edge, polarization direction and the position with respect to the center of the laser spot. These three properties determine the D-peak intensity together. We calculate an effective D-peak intensity by assuming that every point at the edge allows the second order scattering process which is responsible for the D-peak signal. This assumption assures that the following calculation only covers the geometrical changes from a circular shape to a hexagonal shape. Taken into account all these points, the D-peak intensity in a single spectrum measurement, when the laser is positioned as seen in Figure 4.12, is given by:

$$I_D \approx \int \int d\beta dr P(\beta) \cos^2(\theta + \beta) I(\vec{r}). \tag{4.3}$$

The first function in the integral is the polarization function $P(\beta)$, which gives the amplitude of the laser power at an angle β with respect to the horizontal axis, shown

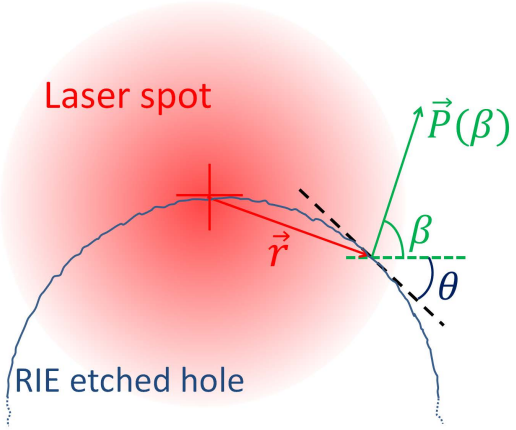

Figure 4.12: Schematic of the integral in equation 4.3 In order to calculate the D-peak intensity with an integral, the components of the integral must be identified while a single spectrum measurement is taken. The center of the laser spot is located at the circumference. For any point along the edge, the distance from the center of the laser spot is defined as $\vec{r}$, the direction of the polarization vector with respect to the horizontal axis is defined as β and the angle between the tangent line at that point and the horizontal axis is defined as θ.

in Figure 4.12. This function is written explicitly in equation 4.4, describing the full elliptical shape of the incident polarization:

$$|\vec{P}(\beta)| = P(\beta) = \sqrt{(2.5\cos\beta)^2 + \sin^2(\beta)}. \tag{4.4}$$

The coefficient (2.5) describes how much the polarization is deviated from a perfect circular polarization due to an asymmetry at the beam splitter. For the circular polarization, β is integrated from 0 to π. The second function $I(\vec{r})$ describes the Gaussian beam shape:

$$I(\vec{r}) = I_0 e^{-2\frac{r^2}{\omega_0^2}} \tag{4.5}$$

with $\vec{r}$ being the radial distance from the center of the laser spot to the respective point at the edge and ω_0 being the (Gaussian) beam waist, measured and calculated to be 430 nm. The third part is the cosine squared function which is a correction due to that the D-peak intensity is maximum (minimum) when the polarization direction is parallel (perpendicular) to the edge direction. The argument of this function is the

sum of the polarization angle β and the angle θ of the tangent line with respect to the horizontal axis, as shown in Figure 4.12.

In order to calculate the effective D-peak intensity at the RIE hole, we apply this integral onto the circumference that fits inside the laser spot, as drawn schematically in Figure 4.12. For ease-of-calculation, the full circular shape is approximated as a 60-edge-polygon which has an imperceptible effect on the calculation. It should also be noted that the integral in equation 4.3 is converted into a line integral for the actual calculation.

Secondly, we calculate the effective D-peak intensity for the hexagonal hole. This calculation is easier than the circular case since it includes only 3 edge segments with angles of 0 and ± 60 degrees. The lengths of the hexagonal hole edges are measured on AFM images. All the dimensions of the holes and the D-peak intensity calculations are given in Table 1.

Then we calculate the graphene area enclosed in the laser spot. Obviously, from the circular to the hexagonal case it is a different geometrical shape and area of graphene. Since we locate the center of the beam at the center of the top or bottom edge, half of the laser spot is always filled but only the side pieces around the hole are different after each etching step. At this point, we calculate the area by using simple geometry and write the result again in Table 1. As you can see the change in area is at most 14 %. In this calculation, we assume that the G-peak intensity is proportional to the amount of graphene enclosed in the area of the laser spot and we do not consider the Gaussian intensity profile. In fact, the effect of these side areas on the G-peak intensity is much less than the calculated values since they are further away from the center so that they are less excited due to the Gaussian beam shape. This approximation actually makes our argumentation bolder.

The resulting I_D/I_G ratios are given in Table 1. All the values in the table are normalized to the value for the RIE hole of the corresponding quantity. That is why in each column, the top row (RIE hole value) is always equal to 1 and the values for 2h etching

and 4h etching show the change from the RIE case. Apparently, the geometrical change of the edge length and the area does not correspond to the measured values of I_D/I_G in the main text. This means that the increase of the I_D/I_G values from the RIE hole to the H plasma etched hole is not due to that the edge is longer or the graphene area is less but it is due to a change in the atomic configuration at the edge. Namely, going from the RIE hole to the H plasma hole there are more edge segments contributing to the D-peak signal.

Etching (x)	Total edge length inside ω_0	Calculated I_D^x/I_D^{RIE}	Area inside ω_0 $\approx I_G^x/I_G^{RIE}$	Measured I_D^x/I_G^x (main text)	Calculated I_D^x/I_G^x (geometry)
RIE	$\sim 940nm$	1	1	1	1
2h H-plasma	$\sim 945nm$	1.03	0.89	2.4	1.16
4h H-plasma	$\sim 950nm$	1.04	0.86	2.4	1.21

Table 1: Calculations for the 600 nm hole with circularly polarized light

4.6.6 Electronic Mobility of Encapsulated Hall Bar

In this section we present transport data recorded on a SL graphene Hall bar encapsulated between two hBN flakes. In particular we are interested in the cleanliness of the encapsulated graphene and extract the mean free path l_{mfp} of the charge carriers to compare it with relevant length scales of the investigated graphene nano ribbon (GNR) devices discussed in the main manuscript (Fig. 6). In Figure 4.13 a) an optical microscopy image of the encapsulated Hall bar is shown with the electronic circuit drawn on top of it. In panel b) the conductivity σ as a function of the charge carrier density n is plotted. The blue and green curves are fits to the following equation:

$$\sigma(n) = \left(\frac{1}{\mu n e + \sigma_0} + \rho_s \right)^{-1} \tag{4.6}$$

where μ is the mobility, e the electronic charge, σ_0 the minimal conductivity caused by the residual doping and ρ_s a series resistivity which is composed of the contact resistances and the cryostat lead resistances. The fit to the electron side (green curve) gives

$\mu = 151'000\,\mathrm{Vs/cm^2}$ and the fit to the hole side (blue curve) gives $\mu = 90'000\,\mathrm{Vs/cm^2}$. In panel c) we plot σ as a function of n on a log-log scale. By looking at the position of the kink indicated by the black solid and dashed lines we extract an estimate of the residual disorder density which is $1.5 \cdot 10^{10}\,\mathrm{cm^{-2}}$ for the hole side and $4.6 \cdot 10^{10}\,\mathrm{cm^{-2}}$ for the electron side. Further, we calculate l_{mfp} of the charge carriers for the electron side by using the following formula:

$$l_{mfp}(\mu, n) = \frac{\hbar}{e} \cdot \mu \cdot \sqrt{\pi n} \tag{4.7}$$

where $\hbar$ is the Planck constant.

The mean free path reaches $1\,\mu$m at $n = 2.6{\cdot}10^{11}\,\mathrm{cm^{-2}}$ which clearly exceeds all relevant length scales in the GNR devices discussed in the main manuscript (Fig. 6).

4.6.7 Conversion of Backgate Voltage to the pn-interface Location

In order to interpret the valley-isospin oscillations in terms of the pn-interface locations it is necessary to convert gate voltages to the actual pn-interface locations. In Figure 4.14 a) a calculation of the electrostatics of the studied device is shown where the pn-interface position Δx_{pn} as a function of back gate and top gate voltages is plotted. In panel b) a cut along the red solid line in a) is shown. This curve was used to convert back gate voltage to Δx_{pn} for the curves presented in the main manuscript. Panel c) shows a schematic of the device where Δx_{pn} is indicated. Hence, Δx_{pn} denotes how far the left pn-interface moves to the left and the right pn-interface moves to the right.

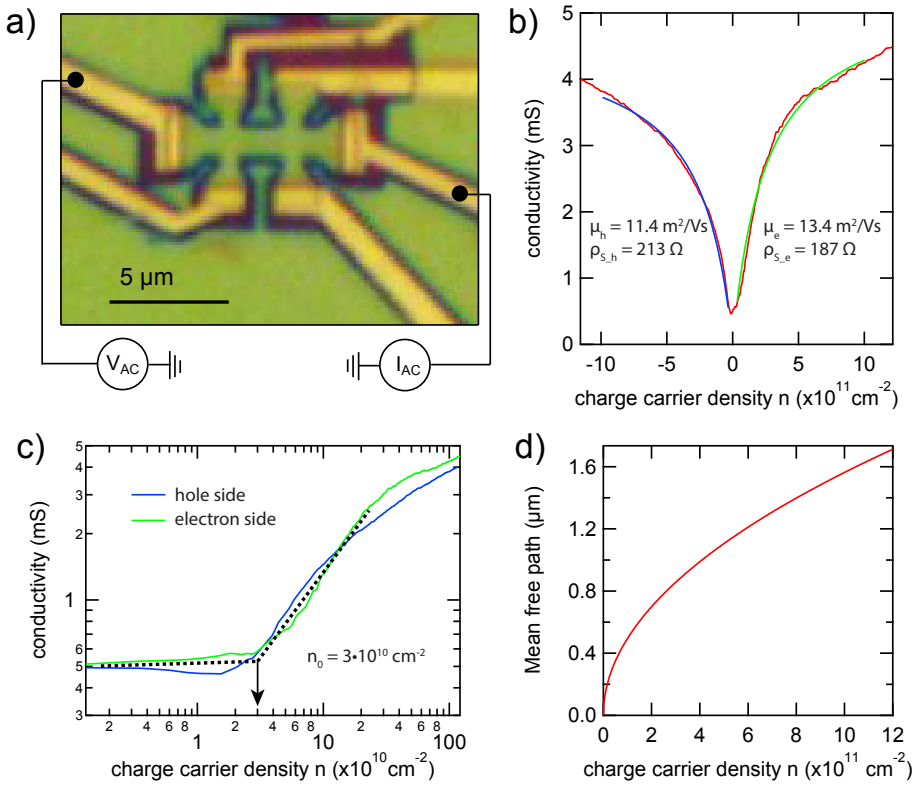

Figure 4.13: Mobility of an Encapsulated Hall Bar a) Optical microscopy image of the investigated SL graphene Hall bar encapsulated between two hBN flakes. The side contacts are yellow and the electronic circuit is indicated. b) Conductivity as a function of the charge carrier density. The green and blue curves are fits to equation 4.6. The following fitting parameters were obtained: electron side, $\mu = 1.51 \cdot 10^5 \pm 1 \cdot 10^3\,\mathrm{Vs/cm^2}$, $\rho_s = 192.3 \pm 0.6\,\Omega$, $\sigma_0 = 8 \cdot 10^{-21} \pm 3 \cdot 10^{-5}\,\mathrm{S}$; hole side: $\mu = 9 \cdot 10^4 \pm 7 \cdot 10^2\,\mathrm{Vs/cm^2}$, $\rho_s = 195.1 \pm 0.6\,\Omega$, $\sigma_0 = 2.3 \cdot 10^{-4} \pm 2 \cdot 10^{-5}\,\mathrm{S}$ c) Conductivity as a function of the absolute value of the charge carrier density plotted in a log-log representation. The locations of the kinks give the estimates of the residual disorder density which is $1.5 \cdot 10^{10}\,\mathrm{cm^{-2}}$ for the hole side and $4.6 \cdot 10^{10}\,\mathrm{cm^{-2}}$ for the electron side. d) Mean free path as a function of the charge carrier density for the mobility value obtained for the electron side.

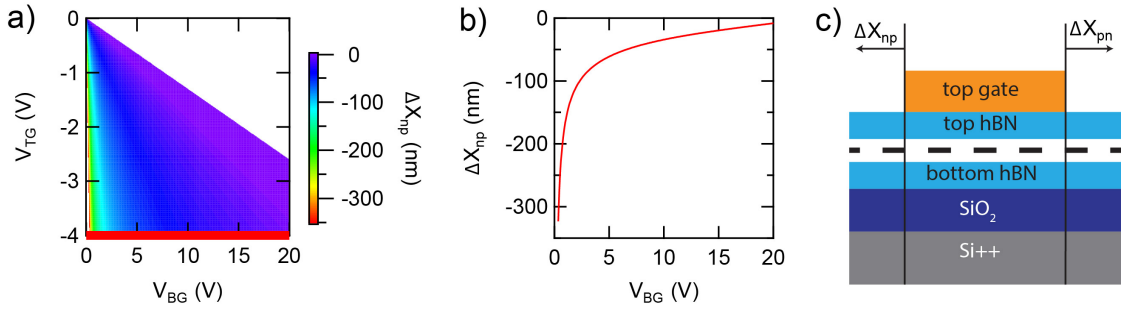

Figure 4.14: Conversion of Backgate Voltage to the pn-interface Location a) Electrostatic simulation of the device presented in Figure 5 in the main manuscript where the pn-interface location is plotted as function of top and back gate voltages. b) Cut along the red solid line in a). c) Schematic of the device with the pn-interface locations indicated.

5 Adiabatic Nuclear Demagnetization down to 1.8 mK

This chapter is concerned with experiments on cooling a Coulomb blockade thermometer (CBT) via adiabatic nuclear demagnetization (AND) in a cryogen free fridge. A CBT consists of an array of Al/AlO_x tunnel junctions with large Cu cooling fins which serve as nuclear spin reservoirs. The concept applied here is called on-and-off chip cooling [31]. In this concept, each measurement lead is cooled through its own nuclear refrigerator (NR) which reduces the heat leaking to the chip during the demagnetization process. On the other hand, to cool the electrons in the nanoelectronic device, AND is applied on the nuclear spin reservoirs of Cu islands deposited on the chip. The nanoelectronic device is a Coulomb blockade thermometer, from which one can determine the electron temperature via transport measurements.

Application of this concept resulted in electron temperatures down to 1.8 mK in a Coulomb blockade thermometer device. The previous experiments carried out in the same system reached electron temperatures of 2.8 mK in the same kind of a device and pointed out few mechanisms which prevent reaching lower temperatures [31]. Here further analysis will be done by investigating few other parameters such as sample orientation, ramp rate and precooling duration. An attempt is also made by stabilizing the inner shields of the cryostat with each other in order to reduce mechanical vibrations.

The following sections will explain the experimental set up, calibration of a Coulomb blockade thermometer and two AND cool-downs. Different experimental parameters will be investigated also together with a reported experiment by Palma et al. [31].

5.1 Experimental Setup: Cryo-free Refrigerator

The AND experiment is carried in a Bluefors dry fridge, equipped with a Cryomech Pulse Tube and two 9 T magnets for the sample and the nuclear stage. The schematic of the system is shown in Figure 5.1 A, representing the significant units. Starting from the top, 16 measurement leads come from the room temperature electronic equipment and reach down to the CBT chip going through several stages.

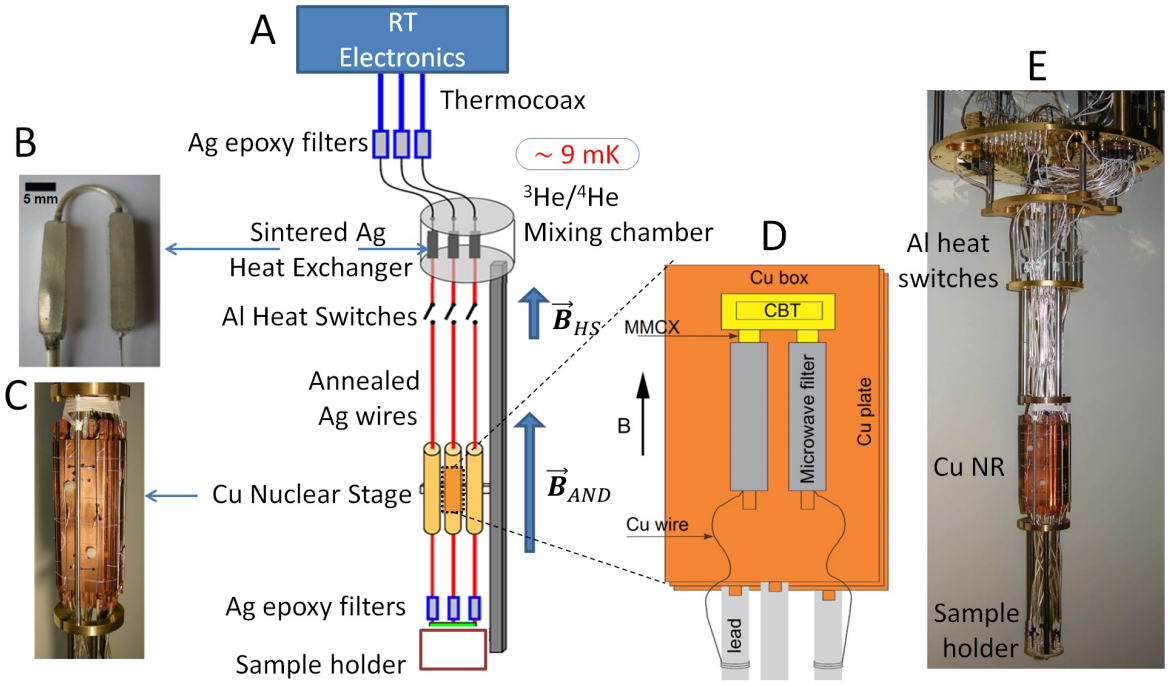

Figure 5.1: Figure of the experiment fridge with significant units. A) Stages of the cooling and filtering, starting from the room temperature electronics down to the sample. Thermocoaxes, Ag epoxy microwave filters and RC filters are the filtering units of the system for electronic noise. The leads are thermalized at each stage, starting from the pulse tube stage down to the mixing chamber and finally at the nuclear refrigerator. Heat switches and the magnetic field regions are also shown. B) Picture of sintered silver heat exchangers. C) Picture of the nuclear refrigerator network. D) Schematic of the copper box where the sample is placed with extra microwave filters right before the box. For better thermalization the copper box and the filters are glued to the side of one of the NRs. E) Picture of the whole system from mixing chamber to sample holder. Figure adapted from [200, 201]

First, the leads are filtered by lossy thermocoaxes until the mixing chamber (MC) stage (100 dB attenuation for f > 3 GHz) [146]. At the MC stage, additional filtering is managed via home-built silver epoxy microwave filters (100 dB f > 200 MHz) [137] and double RC filters (3 dB for f > 45 kHz). After the filtering stages, 16 leads go through

the mixing chamber to be well thermalized via heat exchangers made with sintered silver, see Figure 5.1 B. The silver sinters have huge surface areas (ca. m^2 per gram) to reduce the Kapitza boundary resistance between liquid Helium and the metal leads for greater thermalization. The base temperature of the mixing chamber is ~ 9 mK. After the mixing chamber, the measurement leads are made of annealed thick silver wires (diameter of 2.54 mm), going through Al heat switches with fused joints and spot welded to a nuclear refrigerator. At the MC temperature, Al is a superconductor which is a thermal insulator. Application of a small magnetic field (15 mT) breaks the superconductivity in aluminium, converting it to a thermal conductor. Hence, we can switch between thermally conducting and insulting state while keeping the link always electrically connected. Each measurement lead is spot-welded to its own nuclear refrigerator which is made of 2 mols of copper. This way a network of 16 nuclear refrigerators is established to assure AND cooling of the leads while maintaining electrical isolation from each other and ground.

After the NRs, the leads are extended to the chip carrier at the bottom as annealed silver wires. However, in this experiment, the chip carrier at the bottom was not used. Instead, the CBT chip was integrated (perpendicular to the magnetic field direction) in a small Cu box which is glued with silver epoxy at the side of one of the nuclear refrigerators for greater thermalization. The two leads used for measuring the CBT were filtered with additional microwave filters prior to entering the Cu box through MMCX connectors. The microwave filter used here are home-built by following the procedure in Ref. [137] with lots of patience and neat work. They are made of 2 m long, 0.3 mm thin copper wire wound around $\sim$2 mm thick copper rod which is also demagnetized during AND to provide cooling.

At the mixing chamber flange, a Magnetic Field Fluctuation Thermometer (MFFT) is mounted, which can measure down to 0.120 mK where it hits the SQUID noise floor. The thermal motion of electrons creates current fluctuations in a metal. In order to measure the electron temperatures in the NRs, the magnetic fields priduced by

these current fluctuations are inductively measured by a superconducting gradiometer and then amplified by a SQUID mounted at 4 K [202–205]. The working principles, calibration and implementation of these thermometers to our system are explained elsewhere [25, 31, 200, 206].

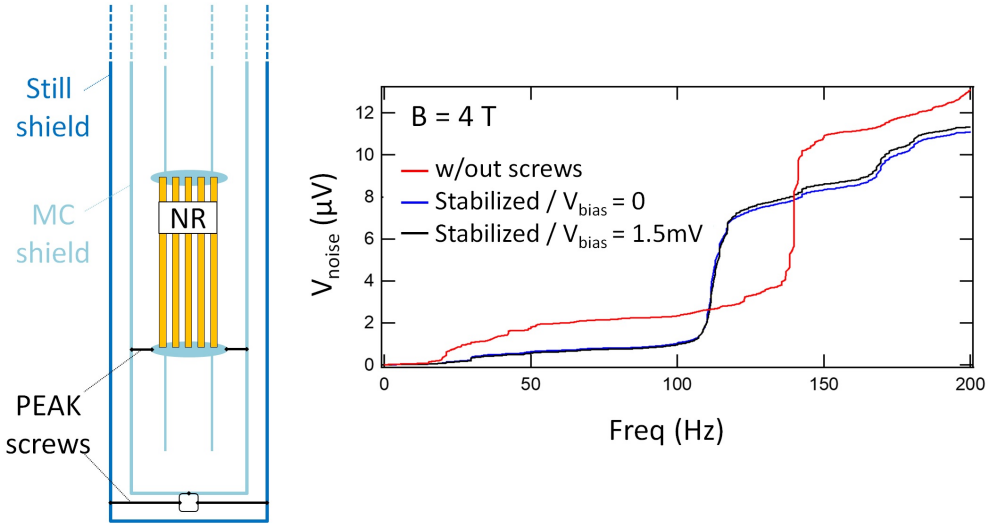

Figure 5.2: Schematic of the MC and the still shields with the NRs in the middle. Black lines indicate the locations where the shields are bolted with PEAK screws for stabilizing the inner parts with each other against the mechanical vibrations. The right panel shows the integrated voltage noise across the CBT as a function of frequency at B = 4 T. As a result of the fixing, the resonance frequency of the structure shifts to a lower frequency. The red curve is adopted from a previous experiment performed in the same system, reported in Ref. [31].

As discussed in the background chapter, mechanical vibrations in the system are one main reason of heat leaks in the presence of magnetic fields due to eddy currents. As an attempt to stabilize the NRs and the CBT sample against the vibrations, the inner cold structure which holds the NRs is screwed to mixing chamber shield via three screws made of Polyether Ether Keton (PEAK), see Figure 5.2. The mixing chamber shield is also screwed to the still shield with same type of screws at the bottom. Even tough PEAK has very low thermal conductivity, the solid connection between separate parts of the system created a higher base temperature (~ 9 mK) compared to the base temperature without screws (~ 6.5 mK) [200, 201]. The idea behind is that the shields are rigidly attached to MC and still flanges, whereas NRs are not, and carry a larger mass which could lead to larger vibrations. Hence, fixing these parts would lead to

stabilization. As a result of this fixation, the resonance frequency of vibrations have been shifted as can be seen in the integrated voltage noise spectra across the CBT in Figure 5.2.

5.2 Coulomb Blockade Thermometry

A Coulomb blockade thermometer makes use of the Coulomb blockade effect of charge carriers tunneling through an insulating barrier between two large metallic reservoirs [29, 30].

The device consists of linear arrays of $Al/AlO_x/Al$ tunnel junctions with large metallic islands in between them as shown in Figure 5.3. On top of 40 nm thick Al top layer, 200 nm of copper is also deposited. This thick layer of copper provides the necessary nuclear spin reservoir on the chip. During AND process, the nuclear spins of the copper layer are demagnetized and supply cooling to the conduction electrons. The total array comprises of 32 tunnel junctions with 16 large copper islands in between them.

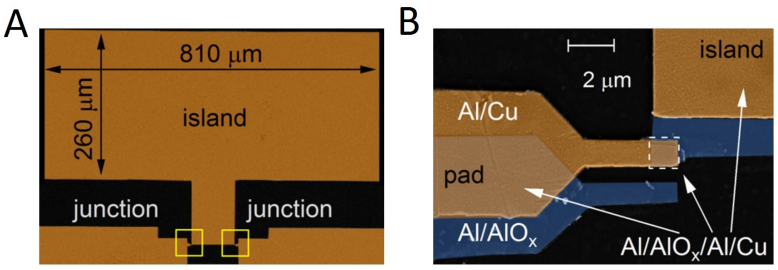

Figure 5.3: False color electron micrographs of the CBT sample. A) The large copper island (volume $\approx 42'000\,\mu m^3$) with two tunnel junctions (yellow boxes). B) Close up image of a tunnel junction shown in the yellow box in left panel. Details of fabrication of such samples are explained in Ref. [152]. Figure taken from [31].

The electronic temperature is obtained by measuring 2-wire differential conductance g of the CBT as a function of bias voltage V_{bias}. The measurement is done by applying few μV AC excitation with a lock-in amplifier at a frequency of 7 Hz. In Figure 5.4 A, typical conductance traces are shown for different temperatures. The zero bias conductance, g_0, is suppressed compared to the high bias asymptotic value g_T, due to environmental Coulomb blockade effects, creating the zero bias dip [29]. As repre-

sented by the colour coding in Figure 5.4 A, the dip gets narrower and lower with the decreasing temperature. Both the width or depth of the conductance dip can be used to determine electron temperature. The full width at half maximum is directly related to temperature which can be used as a primary thermometer [30]:

$$\mathrm{V_{1/2}} \simeq 5.439\,\frac{\mathrm{N k_B T}}{\mathrm{e}} \tag{5.1}$$

where N is the number of junctions in the array and e is the electron charge. This direct relationship with temperature assumes no overheating effects and all junctions to be in thermal equilibrium. The width can be obtained with a bias sweep measurement, which in turn causes overheating of the device. In Figure 5.4 A, a conductance trace at zero bias and at MC temperature is appended (as a function of time, top axis). As seen, the conductance value is lower than the value the dip reaches for the same temperature. Therefore, the width of the dip would give a higher temperature reading due to overheating. Hence, instead of the width, the depth of the dip, i.e. conductance value at zero bias, is a more accurate measure of the temperature. However, it is a secondary thermometer and requires calibration to directly deduce the temperature.

For the calibration, we measure 2-wire conductance at different temperatures and obtain zero bias conductance g_0 and high-bias conductance g_T values. Then, we plot the normalized conductance dip δg as a function of temperature as in Figure 5.4 B. The normalized zero bias dip δg is given by [30]:

$$\delta \mathrm{g} = 1 - \frac{\mathrm{g_0}}{\mathrm{g_T}} = \frac{\mathrm{u}}{6} - \frac{\mathrm{u}^2}{60} + \frac{\mathrm{u}^3}{630}, \qquad \mathrm{u} = \frac{\mathrm{E_c}}{\mathrm{k_B T_{CBT}}}, \tag{5.2}$$

where k_B is the Boltzman constant, E_C is the charging energy of the tunnel junction and T_{CBT} is the electronic temperature in CBT. We fit the Equation 5.2 to data in Figure 5.4 B while keeping the charging energy E_C as a free parameter. The fitting is applied at higher temperatures, $T_{CBT} \geq 30\,\mathrm{mK}$ where the device is well thermalized with the system. The deviation of the fit from the actual values of δg is visible at lower

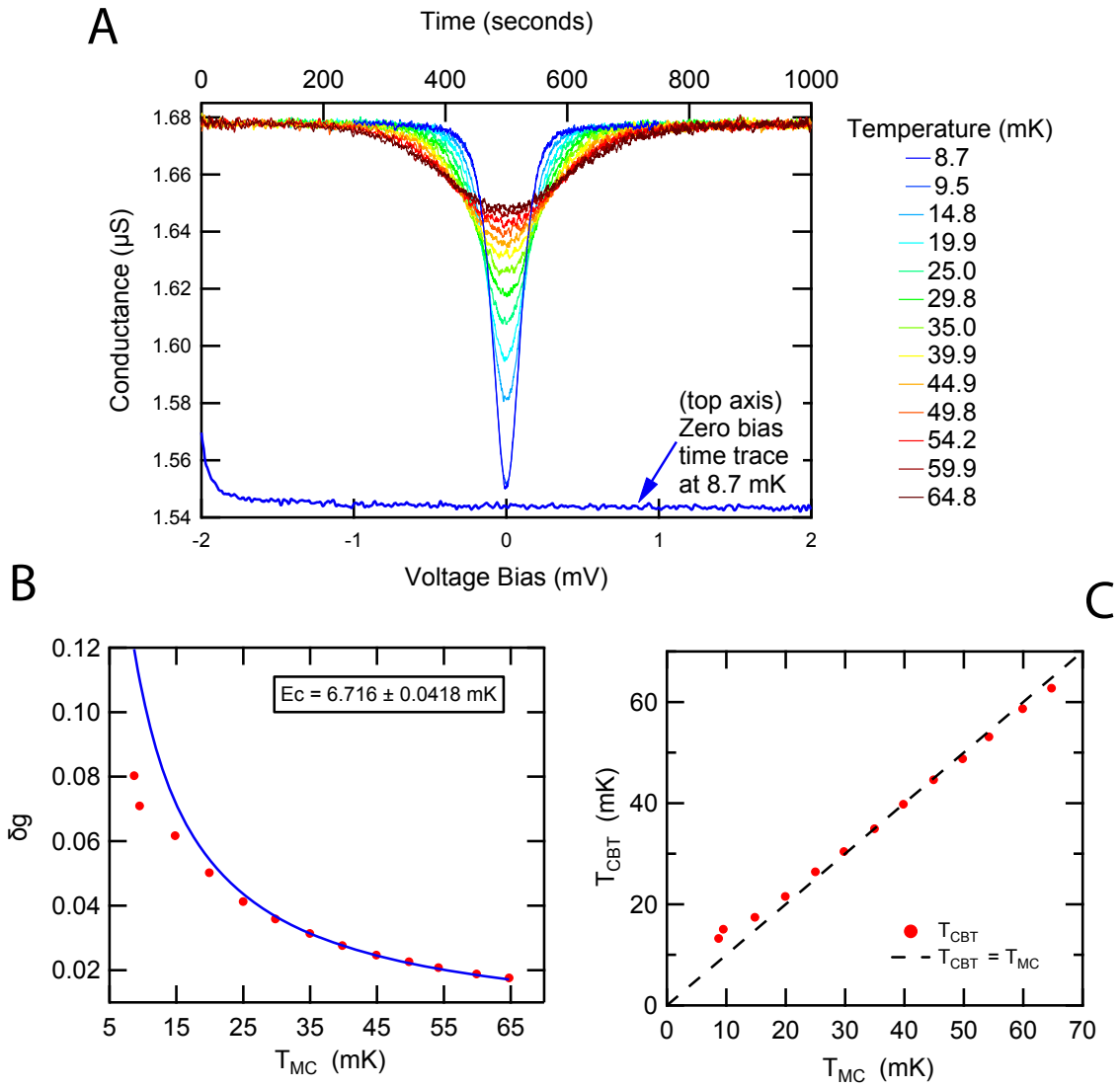

Figure 5.4: Calibration of the CBT against the MC temperature A) The 2-wire conductance of the CBT (lead resistance subtracted) as a function of voltage bias at various temperatures. As the temperature decreases, the conductance dip at zero bias gets deeper and narrower. The top axis belongs to the zero bias time trace at 8.7 mK, showing the overheating effect of bias sweep at the same temperature (dark blue curve) B) Normalized conductance dip as a function of temperature (red dots). The red curve is the fit to the Equation 5.2, giving the charge energy of the device as 6.71 mK. C) CBT temperature against the MC temperature, calculated with charging energy obtained in panel B.

temperatures due to heat leaks.

As a result of the fit, charging energy of the CBT tunnel junctions, $E_C = 6.71 \pm 0.04$ mK, is extracted. The extracted value of charging energy is then used for determining the electron temperature from the measured g_0 values during the AND process via Equation 5.2. During the demagnetization step, the differential conductance, g_0, will

be constantly measured at the exact dip location with effectively zero bias to prevent overheating.

The validity of Equation 5.2 depends on the ratio u and was investigated in Ref. [29, 207]. The range of a CBT device for accurate temperature reading is when $E_C \sim k_B T$. For $E_C > k_B T$, the temperature reading will lose its accuracy since the single electron charging effects dominate at this regime rather than temperature dependency of conductance through the tunnel junctions. In particular with our sample, electron temperatures down to roughly 2 mK can be measured with an accuracy of about 15% [207].

5.3 Adiabatic Nuclear Demagnetization

In principle, the final temperature of the AND process is determined only by the magnetic field reduction. However, the heat leaks in the system break the adiabatic process and increase the final temperature. Since these heat leaks are related to the experimental environment, it is possible to tune experimental parameters in order to minimize the heat leaks. Previous studies have already investigated some of these structural and experimental parameters and have reached electronic temperature of 2.8 mK in the same system where the CBT sample is mounted parallel to the magnetic field direction [31, 200, 201, 206]. Here we implemented the CBT chip in perpendicular to the magnetic field to be able to demagnetize to lower final fields and performed two cool-downs (CD) with different ramp rates, voltage excitations and precooling durations.

Below, these two cool-downs will be compared with each other and also with a previous cool-down reported in Ref. [31]. As mentioned, the parallel sample configuration in Ref. [31] allows to reduce the magnetic field down to 375 mT, whereas it can be reduced to 80 mT for perpendicular configuration. These final fields are determined such that Al is in metallic phase and not in the superconducting phase i.e. higher than the critical field for Al thin film in perpendicular and parallel configurations. A structural difference

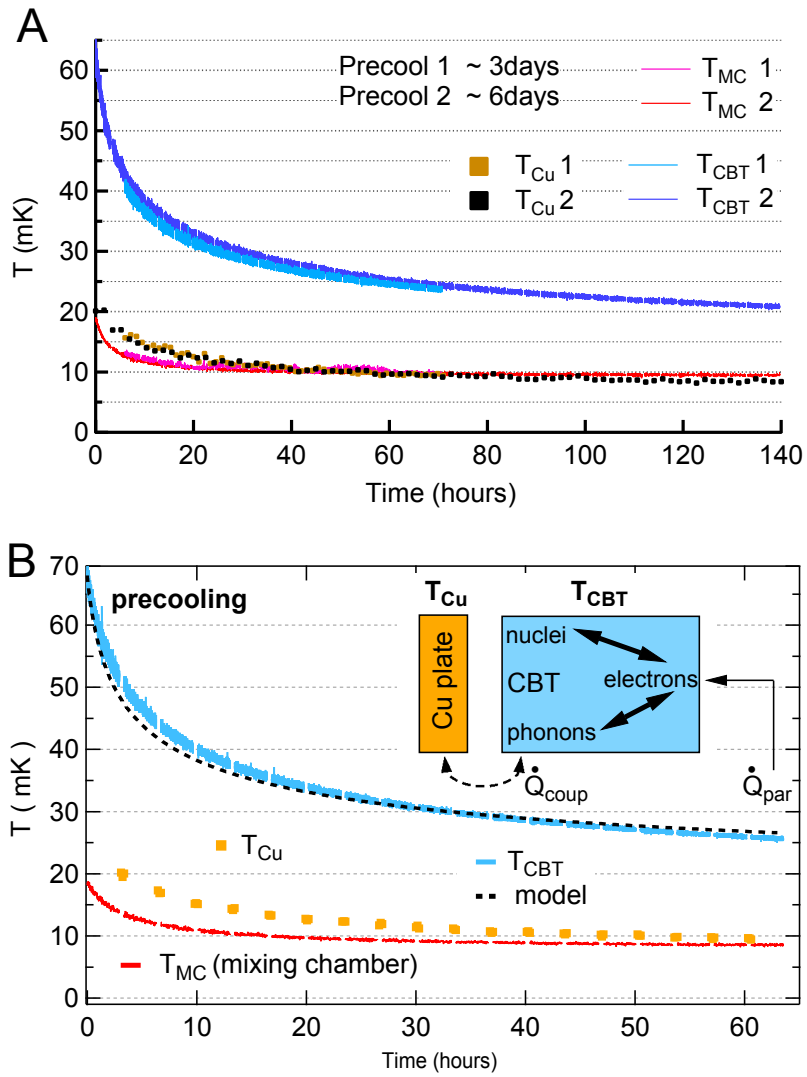

Figure 5.5: The first step of the AND process, *precooling*. Graphs show the temperature of the DR and the CBT after the field is ramped to 9 T. Panel A shows the data for perpendicular configuration and panel B is the parallel configuration reported in [31]. The precooling data of the second cool-down is shifted to match the time-scale of the second cool-down since the data for first cool-down is recorded ~ 6 hours after the field is ramped. During precooling the heat of magnetization created after ramping the field is drained into the DR. See the text for details.

compared to previous study is the implementation of PEAK screws as explained above.

Once the system is well thermalized at the base temperatue ($T_{MC} = 9\,mK$), AND process is started. First, an initial magnetic field of $B_i = 9\,T$ is applied in order to magnetize the nuclear spins in NRs and in the CBT sample. As the nuclear spins are polarized, large heat of magnetization is produced, which should be drained into the mixing chamber. This process is called *precooling* and takes couple of days. In

Figure 5.5, the temperatures of the CBT and mixing chamber are plotted with respect to time. As seen, at the beginning of precooling, the system is much warmer than base temperature. As the mixing chamber supplies the cooling power, T_{CBT} gets closer to mixing chamber temperature but can only reach down to 24 mK after 3 days of precooling for the first cool-down and to 21 mK after 6 days of precooling for the second cool-down. At the same time, temperature of the mixing chamber saturates at 9 mK for both cool-downs. In Figure 5.5 B, data from [31] is shown, where the CBT reaches 24 mK after 3 days.

The discrepancy between T_{CBT} and T_{MC} at the end of precooling indicates heat leaks, especially due to eddy currents created in the presence of magnetic field due to pulse tube vibrations and a weak thermal link between these two parts of the system which are physically in contact with each other. These effects will be discussed further in the following section.

Before starting the nuclear demagnetization, the thermal link between the MC and the NRs are cut by running Al heat switches into the superconducting (or thermally insulating) phase by removing externally applied magnetic field (15 mT). In this way, we prevent the loss of cooling power created in NRs into the MC and the other high temperature parts of the system and reduce the heat leaking into the NR from the warmer upper parts of the system. Then the magnetic field is slowly reduced from $B_i = 9$ T to final field of $B_f = 80$ mT for the perpendicular case, as shown in Figure 5.6 A and 375 mT for the parallel case in Figure 5.6 C.

Another parameter for the demagnetization which we can tune is the ramp rate which should be determined considering the heat leaks to the system. A fast ramp rate creates large eddy current heating since $\dot{Q}_{eddy} \propto \dot{B}^2$. However, the heat leak during the magnetic field sweeps have been observed to be independent of ramp rate in previous experiments carried out in the same system [31, 206]. On the other hand a slow ramp rate will result in a longer process where the system will be exposed to heat leaks for longer duration. For the perpendicular case, different ramp-rates were attempted. The

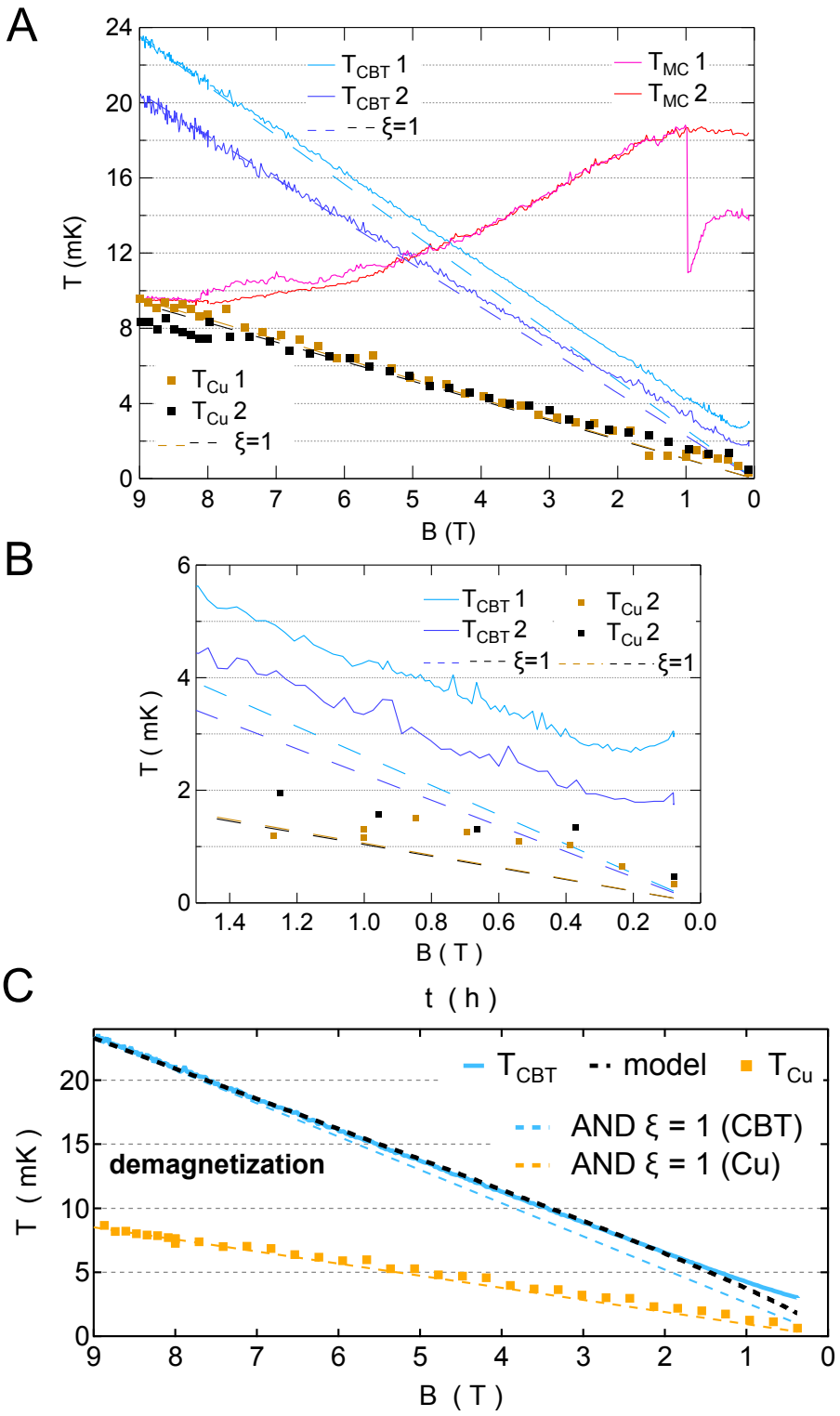

Figure 5.6: *Demagnetization* step of the AND process. A) The temperatures of CBT and NR are shown with respect to magnetic field. The temperature reduction for ideal adiabatic process is also drawn as dashed lines with respective colors. The jump in $T_{MC,1}$ is due to the switching of ramp rate. B) Zoom-in of the plot in A, at the end of demagnetization. C) The demagnetization data taken from [31].

second cool-down is ramped faster (1 T/h from 9 T to 8 T and 2 T/h from 8 T to 80 mT) as opposed to the first cool-down where the ramp rate is slower for the last part of the demagnetization (1 T/h from 1 T to 80 mT).

Also, a lower AC excitation voltage of 4μV is applied in the second cool-down for the conductance measurements as opposed to 10μV in the first cool-down. This is reflected as slightly noisier data for the second cool-down. We note that the applied bias for each island is divided by the number of islands in the array.

	Prec. time days	Prec. Temp. T_i (mK)	Final Field B_f (mT)	Final Temp. for $\xi = 1$ (mK)	Final Temp. T_f (mK)	Efficiency ξ
CBT 1	3	24	80	0.2	2.7	0.08
CBT 2	6	21	80	0.19	1.8	0.10
CBT [31]	3	24	375	1	2.8	0.36
NR 1	3	9	80	0.08	0.15	0.55
NR 2	6	9	80	0.08	0.13	0.61
NR [31]	3	10	375	0.42	0.45	0.93

Table 2: CBT and AND temperatures for the AND experiments for three different cool-downs.

Figure 5.6 shows the temperature of CBT and NRs during the demagnetization process. The temperature reduction in an ideal adiabatic process is also plotted as dashed lines for NRs and CBT. At the end of the demagnetization, the final temperature for an ideal adiabatic process is given by Equation 5.3 and written in Table 2. However, due to heat leaks, the measured final temperatures are higher than the ideal values: $T_{CBT,f,1} = 2.7$ mK and $T_{Cu,f,1} = 0.15$ mK for the first cool-down and $T_{CBT,f,2} = 1.8$ mK and $T_{Cu,f,2} = 0.13$ mK.

Comparing the values in Table 2 can manifest the effect of different parameters employed in different cool-downs. In the perpendicular case (CD 1 and CD 2), the final magnetic field (80 mT) is much lower than the parallel case (CD [31] 375 mT) which, in principle, could lead to lower final temperatures for the same initial temperature. As seen in Figure 5.6 B, at the end of demagnetization, $T_{CBT,1}$ does not decrease until the final field but slightly increases.

Note that the heat capacity becomes very low ($\sim B^2$) at low magnetic fields and so the cooling power from the nuclei is not enough to cool the electrons further. The heat leak in the system takes over against the cooling power and starts to increase the electron temperature of the CBT slightly before demagnetization is finished. This leads to final temperatures higher than otherwise they could reach, see Figure 5.6 A.

Precooling duration obviously has an effect on the initial and final temperatures as can be clearly seen by comparing CD 1 and CD 2. Longer precooling results in lower electron temperatures for CD 2 than CD 1. Since the magnetic field reduction are the same for both cool-downs; equal temperature reduction ratios are expected for both cool-downs, leading to lower final temperatures, as observed. Additionally, CD 2 shows a slightly higher efficiency compared to CD 1, pointing towards an effect of reduced excitation voltage.

It should be also noted that, longer precooling does not necessarily result in lower initial temperatures since T_{CBT} would saturate at a temperature well above T_{MC} due to weak thermal links between the CBT and the DR.

After the demagnetization, temperatures of the system are monitored (without applying any external heat and keeping the heat switches insulating) to learn about their warm up behaviour as plotted in Figure 5.7.

The CBT stays at the lowest temperature for a short amount of time and quickly warms up to 8 mK (6.5 mK) in 2 hours (5 hours) for the first (second) cool-down.

Then a sudden jump in CBT temperature to about 40 mK occurs and is maintained while the copper NRs stay below 1mK for much longer time ($\sim$ 15 hours) due to the much larger spin reservoir. Presumably, this sudden jump to 40 mK occurs when the Cu box or the Cu plate, to which Cu box is glued, warms up while the monitored Cu plate is still cold. This certainly effects the temperature of the monitored Cu plate since a slight increase in T_{Cu} is visible when T_{CBT} jumps to 40 mK, see Figure 5.7. Here, the weak thermal link between the monitored NR and the CBT is again visible as huge temperature difference is sustained. After about 15 hours, the monitored Cu

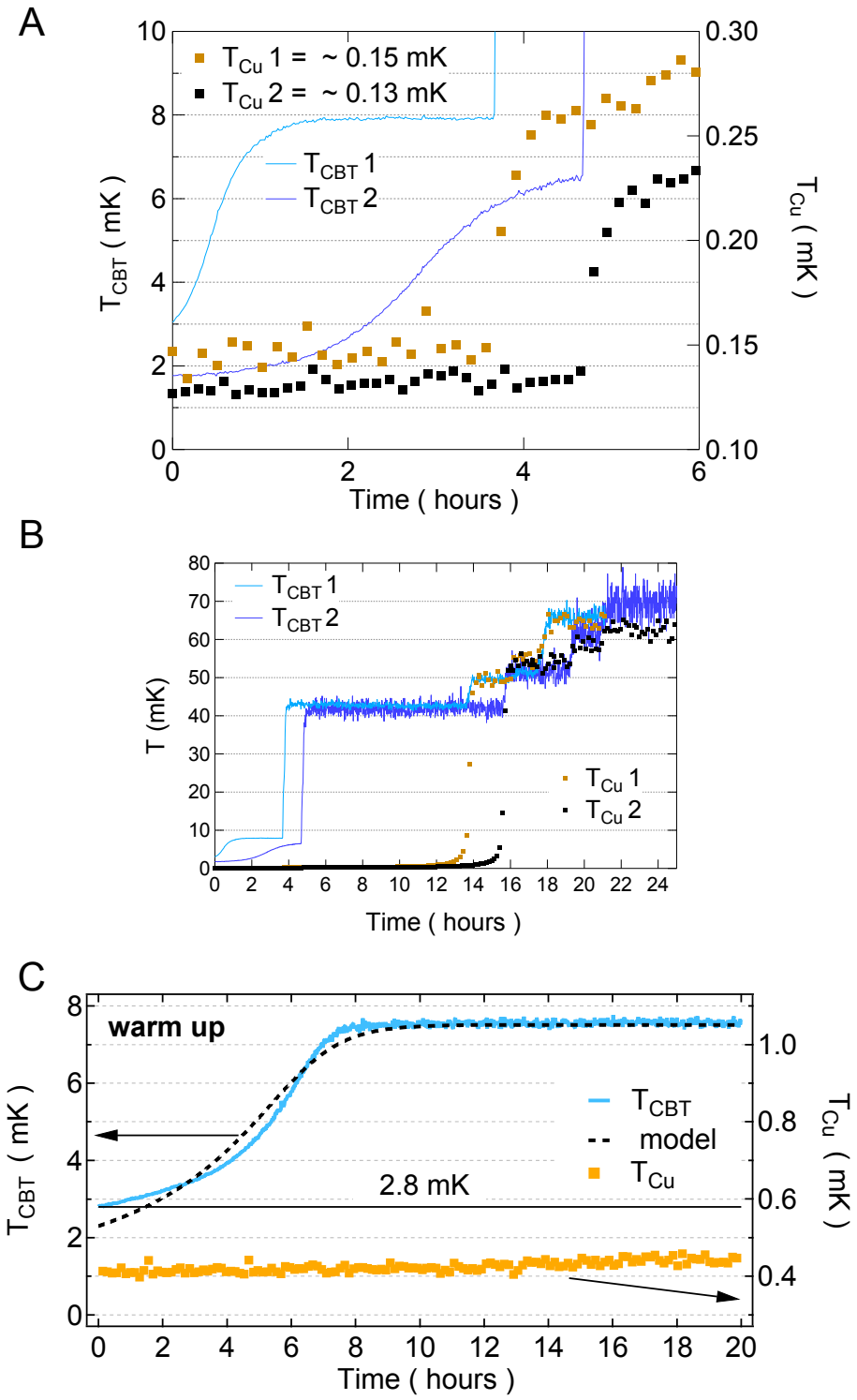

Figure 5.7: *Warm-up* of the CBT and NRs after demagnetization. A) First 6 hours after the system reaches the lowest temperature. CBTs start to warm up slowly while NRs stay at the lowest temperature for about 5 hours. then the sudden jump in CBT temperature occurs, followed by an increase in NR temperature. B) Same data as in A for a longer period of time C) Corresponding warm-up data from [31].

plate and the CBT thermalize with each other and their temperatures are equal. The further stepwise increase in temperature can be attributed to the warming-up of other Cu plates.

5.4 Thermal Dynamics

To get a better insight on the cooling mechanisms and possible heat leaks in the AND process, a simple thermal model will be represented, similar to previous CBT experiments as explained in Ref. [31, 151, 206]. This model tries to explain the thermalizations of the subsystems of the CBT (nuclei, electrons and phonons) and the thermal links between the CBT and the NR.

Figure 5.8 is a schematic showing the subsystems of the CBT and its links to Cu NRs. The electrons are linked to nuclei via Hyperfine Coupling and to phonons via electron-phonon interactions. An important parameter for comparison of these three systems is their heat capacities [25]:

$$\begin{aligned} C_n &\sim \frac{B^2}{T^2} \text{ for Nuclei,} \\ C_{el} &\sim T \text{ for Electrons,} \\ C_{ph} &\sim \frac{T^3}{\Theta_D^3} \text{ for Phonons,} \end{aligned} \tag{5.3}$$

where Θ_D is the Debye temperature.

Among these subsystems, the nuclei have the largest heat capacity at low temperatures. This means that a large cooling power (or heat leak) is necessary to cool down (or warm up) the nuclei. Also, due to their much smaller heat capacity, electrons and phonons come to thermal equilibrium very quickly even tough their coupling is very weak at low temperatures ($\dot{Q}_{el-ph} \sim T^5$).

The thermalization of nuclei with conduction electrons is given by the Koringa law [25]:

$$\tau_1 \mathrm{T_e} = \kappa, \tag{5.4}$$

where τ_1 is the time constant for thermalization of electrons with nuclei due to hyperfine interaction, T_e is the electron temperature and κ is a material dependent value which is a measure of the hyperfine coupling strength. The time constant, τ_1, is defined through:

$$\frac{\mathrm{dT_n^{-1}}}{\mathrm{dt}} = \frac{\mathrm{T_n - T_e}}{\kappa \mathrm{T_n}} = -\frac{\mathrm{T_n^{-1} - T_e^{-1}}}{\tau_1}, \tag{5.5}$$

where T_n is the temperature of the nuclei. For the case of AND where $T_n < T_e$, the nuclei absorb heat from the electrons:

$$\dot{\mathrm{Q}} = \mathrm{nC_e\dot{T}_e} = -\mathrm{nC_n\dot{T}_n}. \tag{5.6}$$

By combining Equations 5.4, 5.5 and 5.6, the rate of change of electronic temperature can be derived:

$$\dot{\mathrm{T}}_\mathrm{e} = -(\mathrm{T_e - T_n})\frac{\mathrm{T_n C_n}}{\kappa \mathrm{C_e}}. \tag{5.7}$$

At low temperatures where $C_e \ll C_n$, Equation 5.7 implies fast cooling of electrons due to cold nuclei.

The copper nuclear refrigerators and the CBT sample are connected to each other in two paths. One of them is the electronic leads which transport heat via Wiedemann-Franz (WF) law and depends on the temperature squared. It should be noted that the WF-cooling is inefficient for arrays of resistive tunnel junctions, meaning that the charge carriers flowing from large copper NRs to the CBT can weakly transfer the cooling power. The MFFT measures the electron temperature at one of the copper NRs which is at the same time one of the measurement leads of the CBT sample. As observed, electron temperature at the NRs are lower than what is measured in the CBT, pointing towards a weak heat transport via conduction electrons. Joule heating ($\sim \mathrm{V^2/R_{junc}}$) at the tunnel junctions of the CBT array is another effect creating heat inside the CBT.

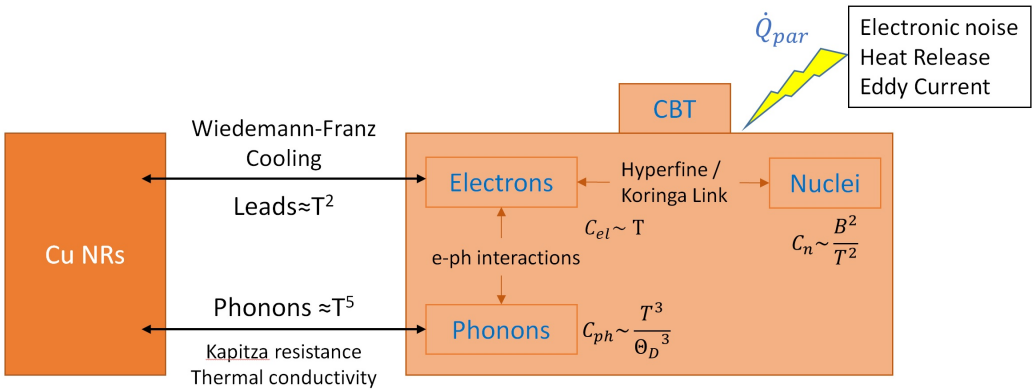

Figure 5.8: The schematic showing the subsystems of the CBT sample and two thermal paths linking it to Cu NRs. Nuclei, electrons and phonons are coupled to each other with different couplings but well thermalized with each other (see main text). On the other hand CBT is coupled to Cu NR via metal leads and through the insulating substrate. A parasitic heat leak is also present, effecting the temperature of the system.

The second path connecting the CBT and the NRs is through the CBT substrate. As explained in subsection 5.1, the CBT sample is placed inside a small copper box which is glued to one of the copper plates at the side of a nuclear refrigerator. This path provides heat transport through phonons which is quite weak at this low temperature regime ($\sim T^3$) and is hindered by Kapitza boundary resistance ($\sim 1/T^3$) at interfaces between copper islands, substrate, copper box and silver epoxy.

This weak coupling between the Cu NRs and the CBT is the reason behind the large temperature differences between the two systems since the CBT sample can not be cooled via the much larger nuclear spin reservoir of NRs. During demagnetization, both systems are demagnetized and are cooled, however, they come into balance at different temperatures depending on the heat leak onto those effectively separate systems and size of their nuclear spin reservoir. On the other hand, during the warm-up, we observe that NRs stay at the lowest temperature for much longer time whereas the CBT slowly warms up and suddenly jumps to 40 mK. Larger spin reservoir of the NRs and the weak link between two systems stand as the reason for T_{NR} to lag behind.

A parasitic heat leak is also introduced in the model due to eddy current heating, electronic noise from the measurement leads and heat release from the materials. Among them, the eddy current heating is quite substantial and can not be easily overcome.

During the precooling stage, the CBT sample and NRs are inside the high magnetic field. The pulse tube of the cryostat continuously creates mechanical oscillations due to large pressure differences in the cold-head at the frequency of pulse tube remote motor (1.4 Hz). In the presence of small inhomogeneities in magnetic field on lateral axis, this oscillations will induce eddy current heating ($\dot{Q}_{eddy} \sim \dot{B}^2 = (dB/dr)^2 * (dr/dt)^2$, where r is displacement). During the demagnetization, the changing magnetic field creates the eddy current heating, resulting in lower efficiencies. Note that the effect of eddy current is different for perpendicular and parallel configurations since the orientations of the CBT chips are different.

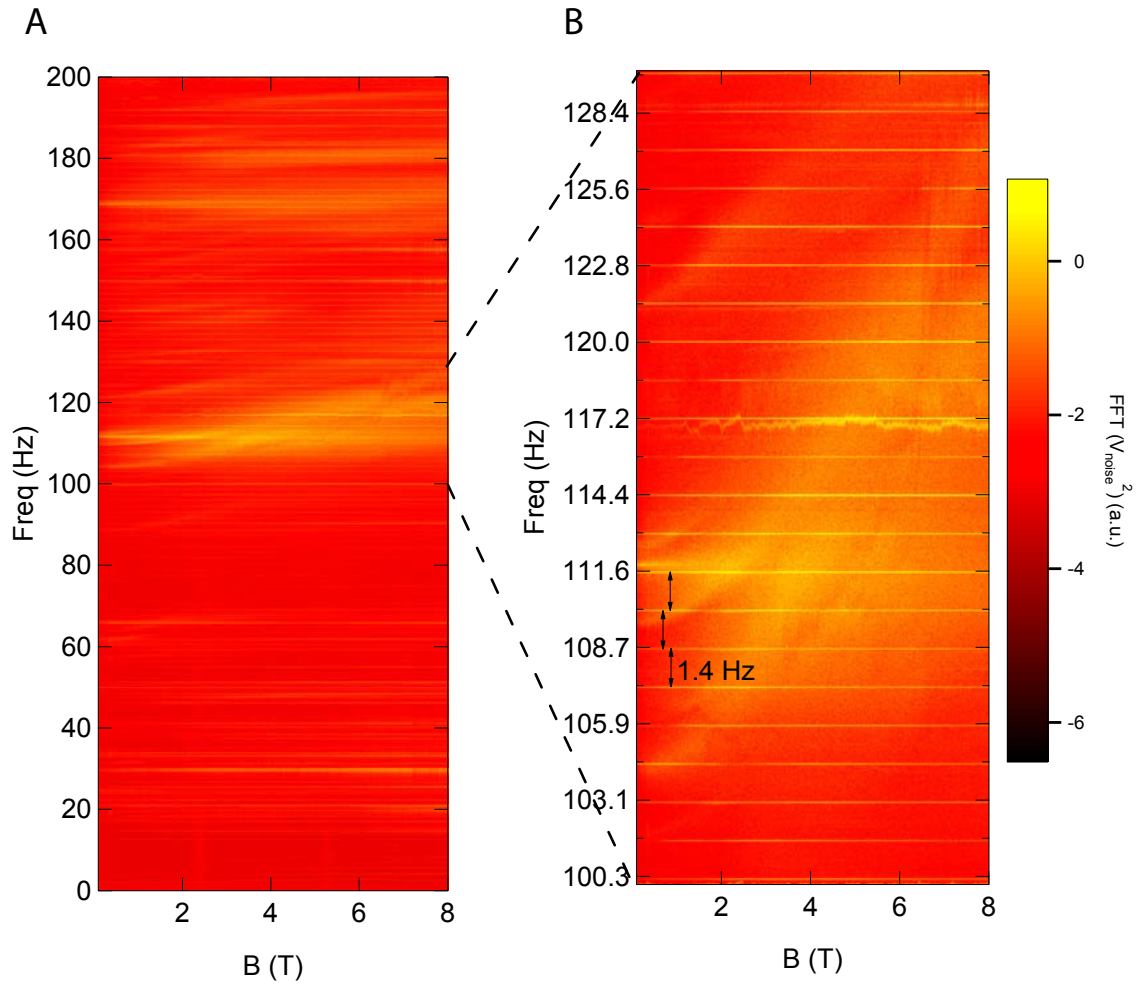

Figure 5.9: FFT spectra of voltage noise across the CBT as a function of magnetic field after fixing the cold tail with PEAK screws. A) Full spectra, showing the increased noise level around 110 Hz B) Zoom-in of the marked region, clearly showing the substructure with intervals of 1.4 Hz.

Figure 5.9 shows the FFT spectra of voltage noise across the CBT as a function of magnetic field, visualizing the relation between the electrical noise and pulse tube vibrations. A clear increase in the noise level is seen around 110 Hz. Besides, a substructure spans the whole frequency range with sharp noise peaks with a separation of 1.4 Hz, which corresponds to the pulse tube frequency. Note that, the same substructure also existed in Ref. [31] but with an eigenfrequency of 140 Hz as shown in Figure 5.2.

5.5 Conclusions

Here in this chapter, two AND cool-downs are performed and CBT temperatures of 2.8 mK and 1.8 mK are measured. Two cool-downs are carried out to compare the effect of experimental parameters in the efficiency of AND process and in the final temperature. A previous study reported by Palma et al. [31] is also taken as a reference for comparison of experimental parameters.

By comparing the cool-downs we can conclude that, longer precooling time results in colder CBT temperatures with similar AND efficiency. We have also observed a slighly higher efficieny for CD 2 compared to CD 1 which may be related to ramp rate difference as opposed to previous observations [31, 206]. It has to be noted that the ideal ramp rate is related to parasitic heat leaks in the system, whether they are time-varying or not and should be determined for each particular system [25, 200].

The weak thermal link between the NRs and the CBTs leads to temperature difference in all stages of the AND process. The CBT can not be cooled with the external Cu NRs but with the nuclear spin reservoirs of copper islands deposited on the chip. Since it is a challenge to better couple the CBT and the NRs at these lowest temperatures, it is favorable to improve the cooling power of the on-chip nuclear refrigerants by using other metals as nuclear refrigerants such as Indium [208]. An alternative device design without tunnel junction arrays would also help to assure better coupling between two systems.

The voltage noise spectra measured through the CBT device shows electrical noise in the system due to mechanical vibrations induced by the pulse tube. To further improve the coldest temperature, one should try to eliminate these vibrations by, for example, decoupling the pulse tube cold head from the cryostat or by using a wet fridge. Plus, the Ag epoxy microwave filters are coils with about 1000 turns which pick up these vibrations and create electrical noise at low frequencies. A cool-down without the filters should also be tried to see their effect.

6 Conclusion

In the course of this thesis, two branches of experiments have been carried out for the prospect of achieving magnetically ordered states in semiconducting condensed matter systems. One of them was to investigate the hydrogen plasma etching in graphene and characterize the etched edges with a view to fabricating high quality zigzag edge graphene nanoribbons, which could support ferromagnetic edges states in their electronic ground state. The second branch was to improve the efficiency of adiabatic nuclear demagnetization in a coulomb blockade thermometer, in order to reach below miliKelvin electron temperatures in a nanoelectronic device.

In chapter 3, the anisotropic etching in graphite and graphene flakes was studied in a hydrogen plasma formed in a high purity quartz tube with an RF power source (13.56 MHz, 30 W). It was known that hydrogen radicals etch graphene starting from defective sites, creating hexagonal etch-pits [15, 116, 117]. Here, we studied the etching parameters and substrate dependence in order to characterize the process. Atomic force microscopy was used extensively to image the etched graphene surfaces.

First, distance, pressure, and temperature dependence was studied on graphite flakes and, as a result, two distinct plasma regimes were defined by comparing the number of etch-pits in a unit area and etching speed. The *direct* plasma regime contains many hydrogen radicals as well as many energetic ions which continuously induce defects on the graphene surface, resulting in perforated surfaces. On the other hand, in the *remote* plasma regime, where the sample is placed in the downstream end, away from the glowing region, the graphene is etched exclusively from pre-existing defects. By performing the etching in this remote plasma regime, it is possible to have the process under control in order to fabricate graphene nanostructures.

The maximum etching speed is determined to be at a temperature of 450 °C and it is revealed that the tube (plasma chamber) material should have a low H recombination coefficient and impurity density as low as possible, since the recombination of H radicals

occurs only at the tube surfaces. Quartz or pyrex tubes serve well for these purposes.

The substrate dependence of the process is also examined by etching single layer and bilayer graphene flakes on SiO_2 and on hBN. Isotropic etching is observed for single layer graphene flakes on SiO_2, whereas highly anisotropic etching with very regular and symmetric edges is observed on hBN.

The precise control of the etching parameters and the location of the hexagonal etch-pits by introducing artificial defects present the opportunity for fabricating graphene nanoribbons with well-defined edges. The advantages of this method compared to others for fabricating graphene nanoribbons (see Chapter 2) are numerous: H-plasma etching creates very clean graphene surfaces without any chemicals involved in the process, it allows the use of hBN as a substrate, and for encapsulation afterwards, which is the ideal graphene device structure for electronic transport measurements, and it makes contacting easier, since a ribbon can be enlarged into larger graphene areas.

The following chapter examined the quality of H-plasma etched edges of graphene flakes to determine whether the edges are of high quality. First, atomic resolution atomic force microscopy was used to image the graphene surfaces. AFM images revealed that the edges of hexagonal etch-pits are parallel to the zigzag crystallographic direction. Plus, the absence of a disorder-related D-peak in the Raman spectrum ($I_D/I_G \sim 0$) of graphene edges revealed high quality zigzag edges for graphite flakes.

However, the Raman microscopy on the etched edges of single layer graphene on hBN showed substantial D-peaks ($I_D/I_G \sim 60\%$) which indicate poor quality. To further elucidate the case, polarization dependent Raman spectroscopy was done, which yielded that for etching in SL graphene on hBN, the edges consist of a mixture of armchair and zigzag edges, with a ratio of 40% to 60%, respectively. Indeed, the edge runs along the zigzag direction but is interrupted by many symmetric armchair segments.

Low-temperature transport measurements were also conducted in two different types of hBN encapsulated samples, one of which is long and wide ($L = 1.6\,\mu m, W = 600\,nm$)

and another which is narrow and short ($L \sim 300\,nm, W \sim 300\,nm$). It turned out that the graphene nanoribbons fabricated with the H-plasma method are of high quality in the bulk but disordered at the edges, which suppresses the edge effects. Comparison of a similar dimension nanoribbon etched with Ar/O_2 plasma presented no qualitative difference with H-plasma etched nanoribbons. Tight-binding calculations for a zigzag edge with armchair segments also supported our experimental findings.

In chapter 5, we shifted gears to the second part of the thesis and cooled down a Coulomb blockade thermometer via adiabatic nuclear demagnetization. The concept applied here is to have a separate nuclear refrigerator for each measurement lead and large copper islands as nuclear spin reservoirs on the chip for efficient cooling of the nanoelectronic device. The electron temperature of 1.8 mK was measured which stands as an improvement to the previously reported result of 2.8 mK

Two different ramp rates and precooling times were tested to obtain a lower electron temperature. A simple thermal model was also given in order to understand the cooling mechanism. We concluded that the cooling of conduction electrons in the CBT device comes from the copper nuclear spin reservoirs deposited on the chip and the external NRs are inefficient for cooling the CBT but helps to reduce heat leaking from the measurement leads to the chip. As a last part, we speculated about the limitations which impede reaching sub-mK temperatures.

6.1 Outlook

One clear conclusion from Chapter 4 is that the H-plasma etching method should be improved in order to obtain high-quality zigzag edges. It would be highly beneficial if the etching process i.e. the dissociation of carbon atoms at the edges is clearly understood on the atomic level. This, in turn, would help to learn what steps should be taken to improve the process.

From an experimental perspective, the etching process can be further tested by tuning

the etching parameters and checking the quality of edges in the same way. Since the temperature plays an active role [193, 194, 199] in formation and reconstruction of edges, the quality of the edges which are etched at different temperatures, can be examined.

In our experiments, the etching was done at 450°C where we obtain the maximum etching speed. The etching speed may also have an effect on the edge structure. A recent study has revealed that different crystallographic directions have different etching speeds, resulting in various geometrical etch-pits depending on the total etch time [113]. So, the process can be further tested to fine tune the etching speed by either changing process temperature or by placing the sample further away in the remote plasma regime where there are fewer hydrogen radicals.

Since the substrate has a major effect in the etching process, i.e., determining whether the process is anisotropic or not, other insulating substrates can also be tested to see if hydrogen plasma etches graphene anisotropically on different materials. A promising avenue of materials to try out is 2D van der Waals materials which recently attracted attention [209]. Besides, it is as well worth to test a similar etching process in other 2D materials, since the field of research in 2D materials is looking forward to fabricating heterostructures out of layered materials in various geometries.

Despite the limitations going below 1 mK in electron temperatures in nanoelectronic devices, certain experiments in semiconductor devices were proposed to benefit from low miliKelvin temperatures. Back action effects in charge sensing [210], fractional quantum hall states [211, 211–213] or strip of stripes model [214, 215] can be explored experimentally at these low temperatures.

In order to accomplish this, the cryostat should modified in such a way to allow mounting semiconducting chips easily with a chip carrier. In the current configuration it is not feasible to mount any kind of sample inside a copper box with limited amount of measurement leads.

It is still quite a challenge to modify the system since the NRs must be coupled very

efficiently to the chip carrier and hold time at the lowest temperatures must be extended. To extend the duration to conduct experiments at the lowest temperature, the heat leaks in the system must be minimized. Currently, an attempt is being made to decouple cold head induced vibrations in the system in order to reduce the heat leaks.

6.2 Pulse Tube Cold Head Suspension

Eddy currents and electrical noise are the two prominent reasons for heat leaks in magnetic refrigeration cryostats. These can be created if the conducting parts of the system (e.g. measurement leads, nuclear refrigerators, Ag epoxy filters made with coils) moves in the presence of inhomogeneous magnetic field. In a dry fridge, the mechanical vibrations induced by the pulse tube cold head can be responsible for this kind of an effect.

Even though the cold head has no moving parts, the high pressure gas pulses from the remote motor are transferred to the cold head via flexible tubes. In order to damp these impulses, the cold head is mounted to the room temperature flange of the cryostat with a bellow. The cold stages of the cold head are also mounted to 50 K and 4 K flanges with soft large area copper braids. Plus, the magnet leads are bolted to the cold head stages for efficient cooling.

Due to these connections between cold head and the cryostat, the impulses at the pulse tube frequency of 1.4 Hz are transferred down to the lower stages of the cryostat where the sample is mounted. An attempt to decouple the cold head from the cryostat is to rigidly suspend the pulse tube from above with a separate structure. This separate structure extends outside of the cryostat table and rigidly fixed to the ground, see Figure 6.1.

The key point of this structure is to make rigid contacts to the cold head, such that the mechanical energy from the remote motor pulses are carried away to the separate structure and to the lab ground, rather than being transferred to the cryostat through

the bellow.

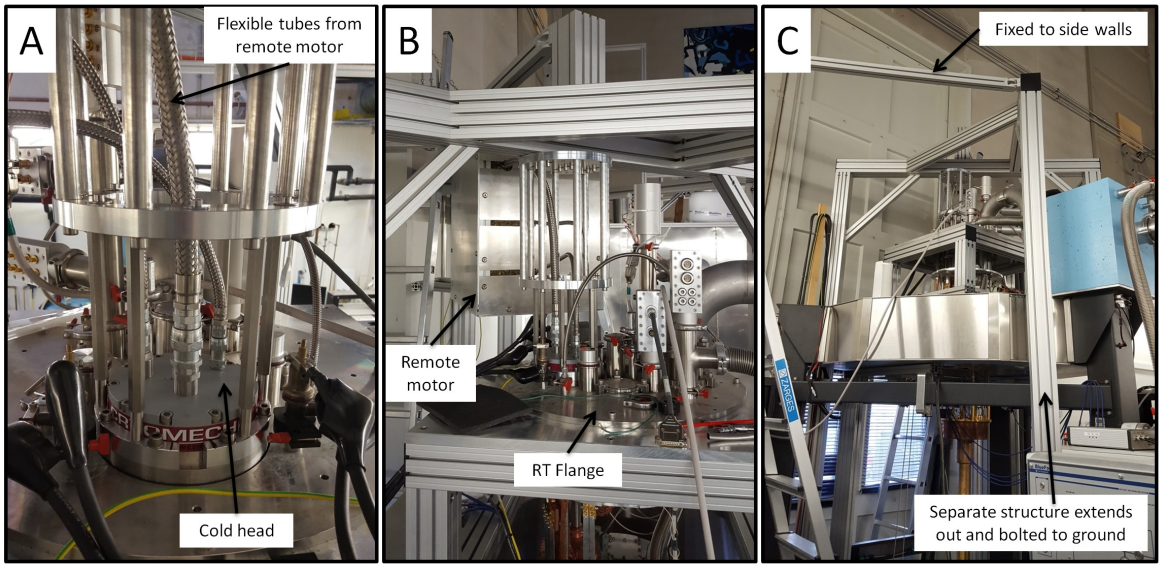

Figure 6.1: Decoupling of the pulse tube with a rigid suspension. A) The cold head is mounted to the cage which is hold tightly by an upper cage to allow rotational alignment when the system is set up. B) The cages are firmly screwed to a separate structure which also allows fine alignment in lateral directions. Remote motor which stand on a separate structure is visible in the picture. C) Large scale picture of the separate structure, which is fixed to the side walls from the top. It extends outside the cryostat table and bolted to the ground.

Other than the cold head suspension, the magnet leads which were connected to the pulse tube stages are also replaced and mounted on the flanges, so that one direct mechanical connection from cold head to the cryostat is also removed.

Before and after these structural changes, the mechanical vibrations in the system are monitored with a vibration analyser. In Figure 6.2, the integrated displacement is plotted as a function of frequency at the mixing chamber flange and at the room temperature flange for both the standard frame and the separate frame. The displacements are recorded in three dimensions separately. It is clear that the effect of decoupling pulse tube is different for different directions and at different stages. For the mixing chamber flange, the vibrations are reduced in the vertical direction, whereas they are increased in the horizontal directions. On the other hand, at the room temperature flange, the vibrations are reduced only in one lateral direction. In the figure, the x-axis grids are adjusted to show the multiples of pulse tube frequency of 1.4 Hz. Clearly, the

integrated displacement increases step by step at these harmonics, especially at lower frequencies. A substantial increase at around 5 Hz is also visible for lateral directions, which is not related to the pulse tube vibrations.

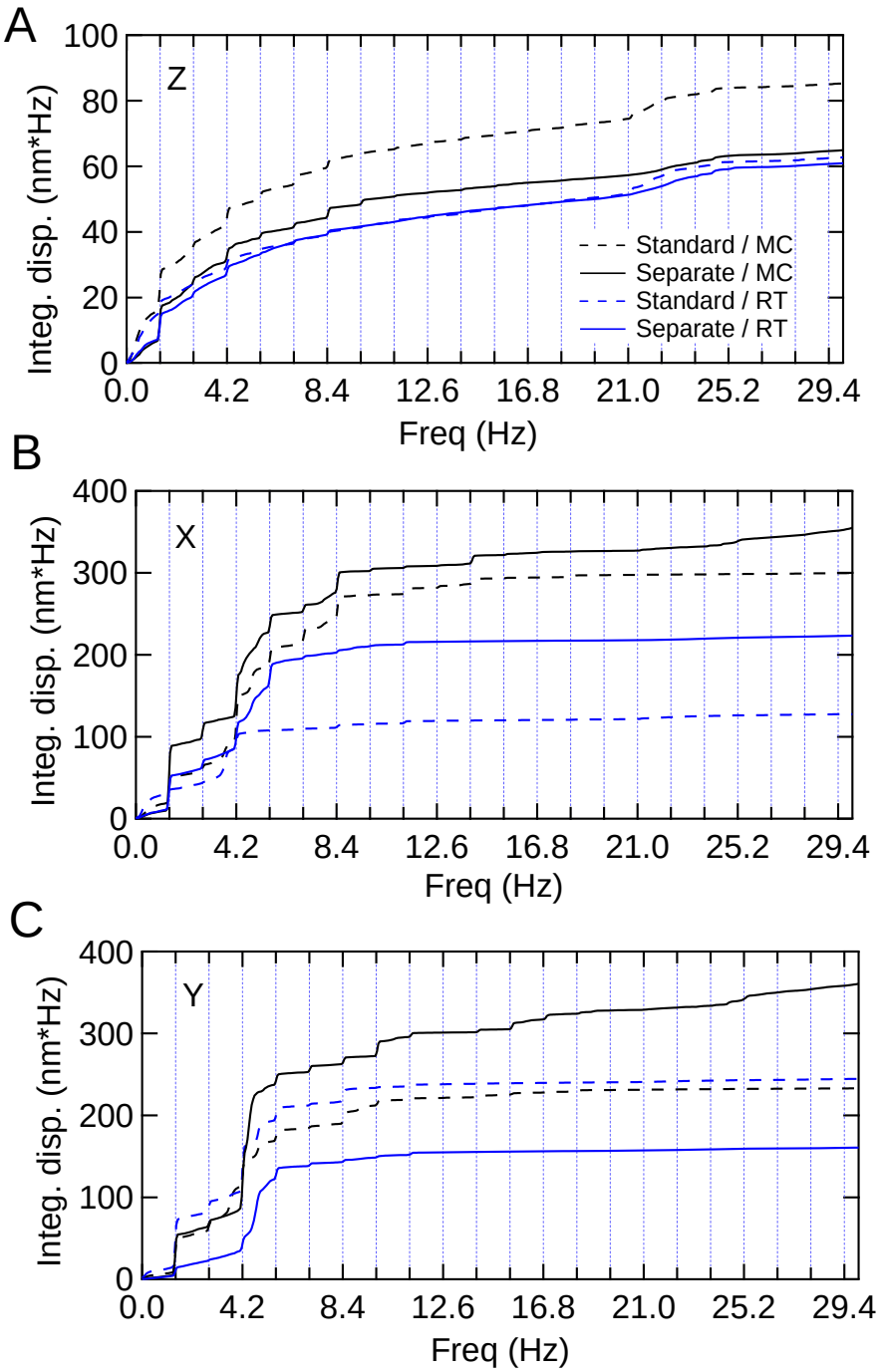

Figure 6.2: Integrated displacement spectra of mechanical vibrations at mixing chamber (black curves) and at room temperature (blue curves) flanges before (dashed curves) and after (solid curves) the cold head suspension in A) vertical direction, B-C) lateral directions. The vertical grids show the multiples 1.4 Hz, the pulse tube frequency harmonics.

In Figure 6.3, the displacement is shown as a function of frequency at the mixing chamber flange. Here, the peaks correspond to the main pulse tube frequency and its harmonics up to 100 Hz. When the pulse tube is turned off (blue curves), the vibrations are in the lab floor level, except some structural resonances at certain bands, which are different for vertical (~ 25 Hz) and lateral (~ 5 Hz and ~ 25 Hz) directions.

It should be noted that, the main peaks at 1.4 Hz in the displacement spectra have very similar amplitudes before and after suspending the pulse tube but the amplitudes for higher harmonics are either damped or amplified, leading to lower or higher values in the integrated spectra, respectively. The resonance band around (25 Hz) seems to be amplified due to the separate structure.

A similar separate structure to suspend the cold head was tested elsewhere [216], and has been shown to reduce vertical vibrations to lab floor level and horizontal vibrations drastically. However, the effect of the suspension structure may differ depending on the lab environment, the mass of the system and the performance of the remote motor.

Vibration measurements are also done when the mechanical connections between the cold head and the cryostat (bellow, copper braids, magnet leads etc.) are removed one by one. As long as there is a physical connection with any of these parts, vibrations at the mixing chamber flange are observed with more or less equal amplitude.

Still, a cool-down with the suspended cold-head should be done to see the AND performance. Note that, the vibration measurements are conducted when the fridge is open, meaning that the heavy magnets and shields are not mounted. Naturally, a heavy load in the system would make a difference in the mechanical vibrations. However, it is not possible to make vibration measurements at the mixing chamber level when the magnets are mounted and the system is closed and cold.

As a conclusion, in order to damp the vibrations, further actions are necessary. An alternative method such as active damping can be tried [217]. However, it would require a more sophisticated structure since an active damper must be specially designed for the cold head. Another alternative action may be damping vibrations on the remote

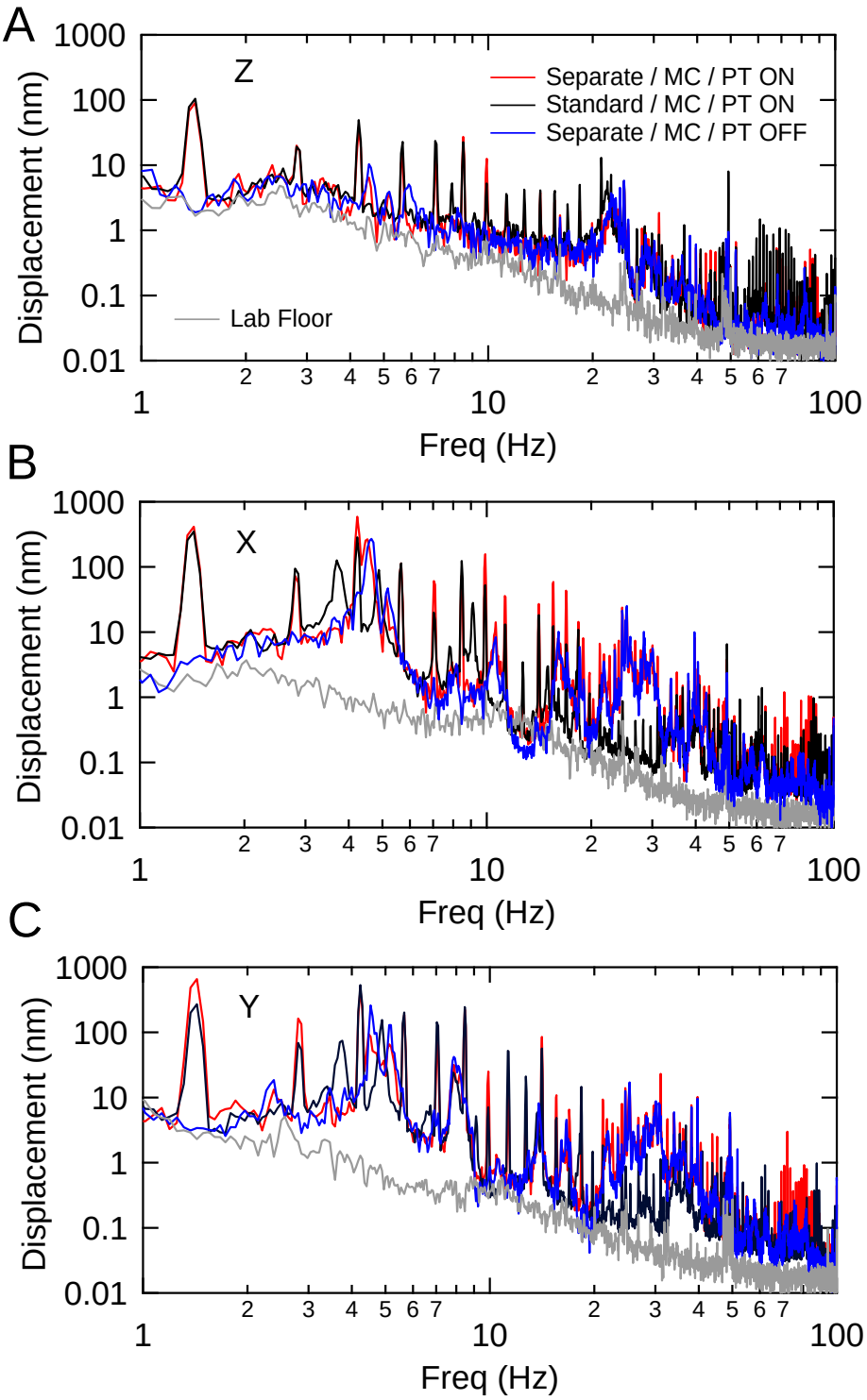

Figure 6.3: Displacment spectra of mechanical vibrations at the mixing chamber flange before (black) and after (red) the cold head suspension. The displacements when the pulse tube is off is also shown (blue). The peaks correspond to pulse tube frequency and its higher harmonics. A) Displacements in vertical direction. B-C) Displacement in lateral directions.

motor side. Since it is the source which transfer high pressure pulses to the cold head, it would be more efficient to damp the vibrations before they reach to cold head.

References

[1] W. Gilbert. *De Magnete, Magneticisque Corporibus, et de Magno Magnete Tellure* (Courier Corporation, 1628).

[2] J. C. Maxwell. *VIII. A dynamical theory of the electromagnetic field.* Philosophical transactions of the Royal Society of London **155**, 459 (1865).

[3] A. Einstein. *On the electrodynamics of moving bodies.* Annalen der Physik **17**, 50 (1905).

[4] I. Žutić, J. Fabian, and S. D. Sarma. *Spintronics: Fundamentals and applications.* Reviews of Modern Physics **76**, 323 (2004).

[5] S. Datta and B. Das. *Electronic analog of the electro-optic modulator.* Applied Physics Letters **56**, 665 (1990).

[6] K. S. Novoselov, A. K. Geim, S. V. Morozov, D. Jiang, Y. Zhang, S. V. Dubonos, I. V. Grigorieva, and A. A. Firsov. *Electric field effect in atomically thin carbon films.* Science **306**, 666 (2004).

[7] K. S. Novoselov, A. K. Geim, S. Morozov, D. Jiang, M. Katsnelson, I. Grigorieva, S. Dubonos, Firsov, and AA. *Two-dimensional gas of massless Dirac fermions in graphene.* Nature **438**, 197 (2005).

[8] C. Lee, X. Wei, J. W. Kysar, and J. Hone. *Measurement of the elastic properties and intrinsic strength of monolayer graphene.* Science **321**, 385 (2008).

[9] Y. Cao, V. Fatemi, S. Fang, K. Watanabe, T. Taniguchi, E. Kaxiras, and P. Jarillo-Herrero. *Unconventional superconductivity in magic-angle graphene superlattices.* Nature **556**, 43 (2018).

[10] M. Katsnelson, K. Novoselov, and A. Geim. *Chiral tunnelling and the Klein paradox in graphene.* Nature Physics **2**, 620 (2006).

[11] H. Aoki and M. S. Dresselhaus. *Physics of graphene* (Springer Science & Business Media, 2013).

[12] O. V. Yazyev. *Emergence of magnetism in graphene materials and nanostructures.* Reports on Progress in Physics **73**, 056501 (2010).

[13] Y. W. Son, M. L. Cohen, and S. G. Louie. *Half-metallic graphene nanoribbons.* Nature **444**, 347 (2006).

[14] H. Shen, Y. Shi, and X. Wang. *Synthesis, charge transport and device applications of graphene nanoribbons.* Synthetic Metals **210**, 109 (2015).

[15] B. McCarroll and D. McKee. *Interaction of atomic hydrogen and nitrogen with graphite surfaces.* Nature **225**, 722 (1970).

[16] D. Loss and D. P. DiVincenzo. *Quantum computation with quantum dots.* Physical Review A **57**, 120 (1998).

[17] G. Burkard and D. Loss. *Electron spins in quantum dots as qubits for quantum information processing.* In *Semiconductor Spintronics and Quantum Computation*, 229–276 (Springer, 2002).

[18] R. Hanson, L. P. Kouwenhoven, J. R. Petta, S. Tarucha, and L. M. Vandersypen. *Spins in few-electron quantum dots.* Reviews of Modern Physics **79**, 1217 (2007).

[19] C. Kloeffel and D. Loss. *Prospects for spin-based quantum computing in quantum dots.* Annu. Rev. Condens. Matter Phys. **4**, 51 (2013).

[20] P. Simon, B. Braunecker, and D. Loss. *Magnetic ordering of nuclear spins in an interacting two-dimensional electron gas.* Physical Review B **77**, 045108 (2008).

[21] P. Simon and D. Loss. *Nuclear spin ferromagnetic phase transition in an interacting two dimensional electron gas.* Physical Review Letters **98**, 156401 (2007).

[22] B. Braunecker, P. Simon, and D. Loss. *Nuclear magnetism and electron order in interacting one-dimensional conductors.* Physical Review B **80**, 165119 (2009).

[23] C. Scheller, T.-M. Liu, G. Barak, A. Yacoby, L. Pfeiffer, K. West, and D. Zumbühl. *Possible evidence for helical nuclear spin order in gaas quantum wires.* Physical Review Letters **112**, 066801 (2014).

[24] H. London, G. Clarke, and E. Mendoza. *Osmotic pressure of He 3 in liquid He 4, with proposals for a refrigerator to work below 1 K.* Physical Review **128**, 1992 (1962).

[25] F. Pobell. *Matter and methods at low temperatures* (Springer, 2007).

[26] N. Kurti, F. H. Robinson, F. Simon, and D. Spohr. *Nuclear cooling.* Nature **178**, 450 (1956).

[27] N. Kurti. *Cooling by adiabatic demagnetization of nuclear spins.* Cryogenics **1** (1960).

[28] P. Berglund, G. Ehnholm, R. Gylling, O. Lounasmaa, and R. Søvik. *Nuclear refrigeration of copper.* Cryogenics **12**, 297 (1972).

[29] J. Pekola, K. Hirvi, J. Kauppinen, and M. Paalanen. *Thermometry by arrays of tunnel junctions.* Physical Review Letters **73**, 2903 (1994).

[30] M. Meschke, J. Pekola, F. Gay, R. Rapp, and H. Godfrin. *Electron thermalization in metallic islands probed by coulomb blockade thermometry.* Journal of Low temperature Physics **134**, 1119 (2004).

[31] M. Palma, C. P. Scheller, D. Maradan, A. V. Feshchenko, M. Meschke, and D. Zumbühl. *On-and-off chip cooling of a Coulomb blockade thermometer down to 2.8 mK.* Applied Physics Letters **111**, 253105 (2017).

[32] C. Enss and S. Hunklinger. *Low-Temperature Physics* (2005).

[33] A. C. Neto, F. Guinea, N. M. Peres, K. S. Novoselov, and A. K. Geim. *The electronic properties of graphene.* Reviews of Modern Physics **81**, 109 (2009).

[34] K. Nakada, M. Fujita, G. Dresselhaus, and M. S. Dresselhaus. *Edge state in graphene ribbons: Nanometer size effect and edge shape dependence.* Physical Review B **54**, 17954 (1996).

[35] V. Barone, O. Hod, and G. E. Scuseria. *Electronic structure and stability of semiconducting graphene nanoribbons.* Nano Letters **6**, 2748 (2006).

[36] L. Brey and H. Fertig. *Electronic states of graphene nanoribbons studied with the Dirac equation.* Physical Review B **73**, 235411 (2006).

[37] M. Ezawa. *Peculiar width dependence of the electronic properties of carbon nanoribbons.* Physical Review B **73**, 045432 (2006).

[38] Y. W. Son, M. L. Cohen, and S. G. Louie. *Energy gaps in graphene nanoribbons.* Physical Review Letters **97**, 216803 (2006).

[39] K. Ariga and M. Ebara. *Materials Nanoarchitectonics* (John Wiley & Sons, 2018).

[40] M. Fujita, K. Wakabayashi, K. Nakada, and K. Kusakabe. *Peculiar localized state at zigzag graphite edge.* Journal of the Physical Society of Japan **65**, 1920 (1996).

[41] N. Peres, A. C. Neto, and F. Guinea. *Conductance quantization in mesoscopic graphene.* Physical Review B **73**, 195411 (2006).

[42] K. Wakabayashi, K.-i. Sasaki, T. Nakanishi, and T. Enoki. *Electronic states of graphene nanoribbons and analytical solutions.* Science and Technology of Advanced Materials **11**, 054504 (2010).

[43] E. H. Lieb. *Two theorems on the Hubbard model.* Physical Review Letters **62**, 1201 (1989).

[44] J. Fernández-Rossier. *Prediction of hidden multiferroic order in graphene zigzag ribbons.* Physical Review B **77**, 075430 (2008).

[45] J. Jung and A. MacDonald. *Carrier density and magnetism in graphene zigzag nanoribbons.* Physical Review B **79**, 235433 (2009).

[46] F. Sols, F. Guinea, and A. C. Neto. *Coulomb blockade in graphene nanoribbons.* Physical Review Letters **99**, 166803 (2007).

[47] B. Huang, F. Liu, J. Wu, B.-L. Gu, and W. Duan. *Suppression of spin polarization in graphene nanoribbons by edge defects and impurities.* Physical Review B **77**, 153411 (2008).

[48] D. A. Areshkin, D. Gunlycke, and C. T. White. *Ballistic transport in graphene nanostrips in the presence of disorder: Importance of edge effects.* Nano Letters **7**, 204 (2007).

[49] S. M.-M. Dubois, A. Lopez-Bezanilla, A. Cresti, F. Triozon, B. Biel, J.-C. Charlier, and S. Roche. *Quantum transport in graphene nanoribbons: Effects of edge reconstruction and chemical reactivity.* ACS Nano **4**, 1971 (2010).

[50] E. R. Mucciolo, A. C. Neto, and C. H. Lewenkopf. *Conductance quantization and transport gaps in disordered graphene nanoribbons.* Physical Review B **79**, 075407 (2009).

[51] J. Klinovaja and D. Loss. *Giant spin-orbit interaction due to rotating magnetic fields in graphene nanoribbons.* Physical Review X **3**, 011008 (2013).

[52] J. Martin, N. Akerman, G. Ulbricht, T. Lohmann, J. v. Smet, K. Von Klitzing, and A. Yacoby. *Observation of electron–hole puddles in graphene using a scanning single-electron transistor.* Nature Physics **4**, 144 (2008).

[53] J. Bai, X. Duan, and Y. Huang. *Rational fabrication of graphene nanoribbons using a nanowire etch mask.* Nano Letters **9**, 2083 (2009).

[54] L. Jiao, L. Xie, and H. Dai. *Densely aligned graphene nanoribbons at 35 nm pitch.* Nano Research **5**, 292 (2012).

[55] V. Abramova, A. S. Slesarev, and J. M. Tour. *Meniscus-mask lithography for narrow graphene nanoribbons.* ACS Nano **7**, 6894 (2013).

[56] M. Y. Han, J. C. Brant, and P. Kim. *Electron transport in disordered graphene nanoribbons.* Physical Review Letters **104**, 056801 (2010).

[57] P. Gallagher, K. Todd, and D. Goldhaber-Gordon. *Disorder-induced gap behavior in graphene nanoribbons.* Physical Review B **81**, 115409 (2010).

[58] C. Stampfer, J. Güttinger, S. Hellmüller, F. Molitor, K. Ensslin, and T. Ihn. *Energy gaps in etched graphene nanoribbons.* Physical Review Letters **102**, 056403 (2009).

[59] D. Querlioz, Y. Apertet, A. Valentin, K. Huet, A. Bournel, S. Galdin-Retailleau, and P. Dollfus. *Suppression of the orientation effects on bandgap in graphene nanoribbons in the presence of edge disorder.* Applied Physics Letters **92**, 042108 (2008).

[60] D. Gunlycke, D. Areshkin, and C. White. *Semiconducting graphene nanostrips with edge disorder.* Applied Physics Letters **90**, 142104 (2007).

[61] Y. Yoon and J. Guo. *Effect of edge roughness in graphene nanoribbon transistors.* Applied Physics Letters **91**, 073103 (2007).

[62] N. Tombros, A. Veligura, J. Junesch, M. H. Guimarães, I. J. Vera-Marun, H. T. Jonkman, and B. J. Van Wees. *Quantized conductance of a suspended graphene nanoconstriction.* Nature Physics **7**, 697 (2011).

[63] B. Özyilmaz, P. Jarillo-Herrero, D. Efetov, and P. Kim. *Electronic transport in locally gated graphene nanoconstrictions.* Applied Physics Letters **91**, 192107 (2007).

[64] K. I. Bolotin, K. Sikes, Z. Jiang, M. Klima, G. Fudenberg, J. Hone, P. Kim, and H. Stormer. *Ultrahigh electron mobility in suspended graphene.* Solid State Communications **146**, 351 (2008).

[65] T. Ando. *Screening effect and impurity scattering in monolayer graphene.* Journal of the Physical Society of Japan **75**, 074716 (2006).

[66] M. Ishigami, J. Chen, W. Cullen, M. Fuhrer, and E. Williams. *Atomic structure of graphene on SiO_2.* Nano Letters **7**, 1643 (2007).

[67] S. Morozov, K. Novoselov, M. Katsnelson, F. Schedin, D. Elias, J. A. Jaszczak, and A. Geim. *Giant intrinsic carrier mobilities in graphene and its bilayer.* Physical Review Letters **100**, 016602 (2008).

[68] S. Fratini and F. Guinea. *Substrate-limited electron dynamics in graphene.* Physical Review B **77**, 195415 (2008).

[69] J.-H. Chen, C. Jang, S. Xiao, M. Ishigami, and M. S. Fuhrer. *Intrinsic and extrinsic performance limits of graphene devices on SiO_2.* Nature Nanotechnology **3**, 206 (2008).

[70] C. R. Dean, A. F. Young, I. Meric, C. Lee, L. Wang, S. Sorgenfrei, K. Watanabe, T. Taniguchi, P. Kim, K. L. Shepard, and J. Hone. *Boron nitride substrates for high-quality graphene electronics.* Nature Nanotechnology **5**, 722 (2010).

[71] G. Giovannetti, P. A. Khomyakov, G. Brocks, P. J. Kelly, and J. Van Den Brink. *Substrate-induced band gap in graphene on hexagonal boron nitride: Ab initio density functional calculations.* Physical Review B **76**, 073103 (2007).

[72] C. H. Lui, L. Liu, K. F. Mak, G. W. Flynn, and T. F. Heinz. *Ultraflat graphene.* Nature **462**, 339 (2009).

[73] L. Wang, I. Meric, P. Huang, Q. Gao, Y. Gao, H. Tran, T. Taniguchi, K. Watanabe, L. Campos, D. Muller, J. Guo, P. Kim, K. Shepard, and C. Dean. *One-dimensional electrical contact to a two-dimensional material.* Science **342**, 614 (2013).

[74] D. Bischoff, T. Krähenmann, S. Dröscher, M. A. Gruner, C. Barraud, T. Ihn, and K. Ensslin. *Reactive-ion-etched graphene nanoribbons on a hexagonal boron nitride substrate.* Applied Physics Letters **101**, 203103 (2012).

[75] B. Terrés, L. Chizhova, F. Libisch, J. Peiro, D. Jörger, S. Engels, A. Girschik, K. Watanabe, T. Taniguchi, S. Rotkin, J. Burgdoerfer, and C. Stampfer. *Size quantization of Dirac fermions in graphene constrictions.* Nature Communications **7**, 11528 (2016).

[76] S. Tian, P. Wang, X. Liu, J. Zhu, H. Fu, T. Taniguchi, K. Watanabe, J.-H. Chen, and X. Lin. *Nonlinear transport of graphene in the quantum Hall regime.* 2D Materials **4**, 015003 (2016).

[77] L. Banszerus, M. Schmitz, S. Engels, M. Goldsche, K. Watanabe, T. Taniguchi, B. Beschoten, and C. Stampfer. *Ballistic transport exceeding 28 μm in CVD grown graphene.* Nano Letters **16**, 1387 (2016).

[78] X. Li, X. Wang, L. Zhang, S. Lee, and H. Dai. *Chemically derived, ultrasmooth graphene nanoribbon semiconductors.* Science **319**, 1229 (2008).

[79] X. Wang, Y. Ouyang, X. Li, H. Wang, J. Guo, and H. Dai. *Room-temperature all-semiconducting sub-10-nm graphene nanoribbon field-effect transistors.* Physical Review Letters **100**, 206803 (2008).

[80] J. M. Poumirol, A. Cresti, S. Roche, W. Escoffier, M. Goiran, X. Wang, X. Li, H. Dai, and B. Raquet. *Edge magnetotransport fingerprints in disordered graphene nanoribbons.* Physical Review B **82**, 041413 (2010).

[81] D. V. Kosynkin, A. L. Higginbotham, A. Sinitskii, J. R. Lomeda, A. Dimiev, B. K. Price, and J. M. Tour. *Longitudinal unzipping of carbon nanotubes to form graphene nanoribbons.* Nature **458**, 872 (2009).

[82] L. Jiao, L. Zhang, X. Wang, G. Diankov, and H. Dai. *Narrow graphene nanoribbons from carbon nanotubes.* Nature **458**, 877 (2009).

[83] L. Jiao, X. Wang, G. Diankov, H. Wang, and H. Dai. *Facile synthesis of high-quality graphene nanoribbons.* Nature Nanotechnology **5**, 321 (2010).

[84] A. L. Elías, A. R. Botello-Méndez, D. Meneses-Rodríguez, V. JehovaÌ GonzaÌlez, D. Ramírez-González, L. Ci, E. Muñoz-Sandoval, P. M. Ajayan, H. Terrones, and M. Terrones. *Longitudinal cutting of pure and doped carbon nanotubes to form graphitic nanoribbons using metal clusters as nanoscalpels.* Nano Letters **10**, 366 (2009).

[85] D. Wei, L. Xie, K. K. Lee, Z. Hu, S. Tan, W. Chen, C. H. Sow, K. Chen, Y. Liu, and A. T. S. Wee. *Controllable unzipping for intramolecular junctions of graphene nanoribbons and single-walled carbon nanotubes.* Nature Communications **4**, 1374 (2013).

[86] C. Tao, L. Jiao, O. V. Yazyev, Y.-C. Chen, J. Feng, X. Zhang, R. B. Capaz, J. M. Tour, A. Zettl, S. G. Louie, H. Dai, and M. Crommie. *Spatially resolving edge states of chiral graphene nanoribbons.* Nature Physics **7**, 616 (2011).

[87] D. V. Kosynkin, W. Lu, A. Sinitskii, G. Pera, Z. Sun, and J. M. Tour. *Highly conductive graphene nanoribbons by longitudinal splitting of carbon nanotubes using potassium vapor.* ACS Nano **5**, 968 (2011).

[88] T. Shimizu, J. Haruyama, D. Marcano, D. Kosinkin, J. Tour, K. Hirose, and K. Suenaga. *Large intrinsic energy bandgaps in annealed nanotube-derived graphene nanoribbons.* Nature Nanotechnology **6**, 45 (2011).

[89] M.-W. Lin, C. Ling, L. A. Agapito, N. Kioussis, Y. Zhang, M. M.-C. Cheng, W. L. Wang, E. Kaxiras, and Z. Zhou. *Approaching the intrinsic band gap in suspended high-mobility graphene nanoribbons.* Physical Review B **84**, 125411 (2011).

[90] M. W. Lin, C. Ling, Y. Zhang, H. J. Yoon, M. M.-C. Cheng, L. A. Agapito, N. Kioussis, N. Widjaja, and Z. Zhou. *Room-temperature high on/off ratio in suspended graphene nanoribbon field-effect transistors.* Nanotechnology **22**, 265201 (2011).

[91] X. Wang, Y. Ouyang, L. Jiao, H. Wang, L. Xie, J. Wu, J. Guo, and H. Dai. *Graphene nanoribbons with smooth edges behave as quantum wires.* Nature Nanotechnology **6**, 563 (2011).

[92] L. Xie, H. Wang, C. Jin, X. Wang, L. Jiao, K. Suenaga, and H. Dai. *Graphene nanoribbons from unzipped carbon nanotubes: atomic structures, Raman spectroscopy, and electrical properties.* Journal of the American Chemical Society **133**, 10394 (2011).

[93] J. Cai, P. Ruffieux, R. Jaafar, M. Bieri, T. Braun, S. Blankenburg, M. Muoth, A. P. Seitsonen, M. Saleh, X. Feng, K. Muellen, and R. Fasel. *Atomically precise bottom-up fabrication of graphene nanoribbons.* Nature **466**, 470 (2010).

[94] P. Ruffieux, J. Cai, N. C. Plumb, L. Patthey, D. Prezzi, A. Ferretti, E. Molinari, X. Feng, K. MuÌˆllen, C. A. Pignedoli, and R. Fasel. *Electronic structure of atomically precise graphene nanoribbons.* ACS Nano **6**, 6930 (2012).

[95] H. Huang, D. Wei, J. Sun, S. L. Wong, Y. P. Feng, A. C. Neto, and A. T. S. Wee. *Spatially resolved electronic structures of atomically precise armchair graphene nanoribbons.* Scientific Reports **2**, 983 (2012).

[96] S. Wang, L. Talirz, C. A. Pignedoli, X. Feng, K. Müllen, R. Fasel, and P. Ruffieux. *Giant edge state splitting at atomically precise graphene zigzag edges.* Nature Communications **7**, 11507 (2016).

[97] P. Ruffieux, S. Wang, B. Yang, C. Sánchez-Sánchez, J. Liu, T. Dienel, L. Talirz, P. Shinde, C. A. Pignedoli, D. Passerone, T. Dumslaff, X. Feng, K. Muellen, and R. Fasel. *On-surface synthesis of graphene nanoribbons with zigzag edge topology.* Nature **531**, 489 (2016).

[98] A. V. Talyzin, I. V. Anoshkin, A. V. Krasheninnikov, R. M. Nieminen, A. G. Nasibulin, H. Jiang, and E. I. Kauppinen. *Synthesis of graphene nanoribbons encapsulated in single-walled carbon nanotubes.* Nano Letters **11**, 4352 (2011).

[99] C. Berger, Z. Song, T. Li, X. Li, A. Y. Ogbazghi, R. Feng, Z. Dai, A. N. Marchenkov, E. H. Conrad, P. N. First, and W. de Heer. *Ultrathin epitaxial graphite: 2D electron gas properties and a route toward graphene-based nanoelectronics.* The Journal of Physical Chemistry B **108**, 19912 (2004).

[100] M. Sprinkle, M. Ruan, Y. Hu, J. Hankinson, M. Rubio-Roy, B. Zhang, X. Wu, C. Berger, and W. A. De Heer. *Scalable templated growth of graphene nanoribbons on SiC.* Nature Nanotechnology **5**, 727 (2010).

[101] J. Baringhaus, M. Ruan, F. Edler, A. Tejeda, M. Sicot, A. Taleb-Ibrahimi, A.-P. Li, Z. Jiang, E. H. Conrad, C. Berger, C. Tegenkamp, and W. de Heer. *Exceptional ballistic transport in epitaxial graphene nanoribbons.* Nature **506**, 349 (2014).

[102] J. Aprojanz, S. R. Power, P. Bampoulis, S. Roche, A.-P. Jauho, H. J. Zandvliet, A. A. Zakharov, and C. Tegenkamp. *Ballistic tracks in graphene nanoribbons.* Nature Communications **9**, 4426 (2018).

[103] L. C. Campos, V. R. Manfrinato, J. D. Sanchez-Yamagishi, J. Kong, and P. Jarillo-Herrero. *Anisotropic etching and nanoribbon formation in single-layer graphene.* Nano Letters **9**, 2600 (2009).

[104] S. S. Datta, D. R. Strachan, S. M. Khamis, and A. C. Johnson. *Crystallographic etching of few-layer graphene.* Nano Letters **8**, 1912 (2008).

[105] Y. Li, M. Chen, M. Weinert, and L. Li. *Direct experimental determination of onset of electron–electron interactions in gap opening of zigzag graphene nanoribbons.* Nature Communications **5**, 4311 (2014).

[106] L. Ci, Z. Xu, L. Wang, W. Gao, F. Ding, K. F. Kelly, B. I. Yakobson, and P. M. Ajayan. *Controlled nanocutting of graphene.* Nano Research **1**, 116 (2008).

[107] C. Keep, S. Terry, and M. Wells. *Studies of the nickel-catalyzed hydrogenation of graphite.* Journal of Catalysis **66**, 451 (1980).

[108] P. Nemes-Incze, G. Magda, K. Kamarás, and L. P. Biró. *Crystallographically selective nanopatterning of graphene on SiO_2.* Nano Research **3**, 110 (2010).

[109] B. Krauss, P. Nemes-Incze, V. Skakalova, L. P. Biro, K. v. Klitzing, and J. H. Smet. *Raman scattering at pure graphene zigzag edges.* Nano Letters **10**, 4544 (2010).

[110] D. Geng, B. Wu, Y. Guo, B. Luo, Y. Xue, J. Chen, G. Yu, and Y. Liu. *Fractal etching of graphene.* Journal of the American Chemical Society **135**, 6431 (2013).

[111] W. Guo, B. Wu, Y. Li, L. Wang, J. Chen, B. Chen, Z. Zhang, L. Peng, S. Wang, and Y. Liu. *Governing rule for dynamic formation of grain boundaries in grown graphene.* ACS Nano **9**, 5792 (2015).

[112] Y. Zhang, Z. Li, P. Kim, L. Zhang, and C. Zhou. *Anisotropic hydrogen etching of chemical vapor deposited graphene.* ACS Nano **6**, 126 (2011).

[113] Y. Y. Stehle, X. Sang, R. R. Unocic, D. Voylov, R. K. Jackson, S. Smirnov, and I. Vlassiouk. *Anisotropic Etching of Hexagonal Boron Nitride and Graphene: Question of Edge Terminations.* Nano Letters **17**, 7306 (2017).

[114] Z. Chen, W. Zhang, C.-A. Palma, A. Lodi Rizzini, B. Liu, A. Abbas, N. Richter, L. Martini, X.-Y. Wang, N. Cavani, H. Lu, N. Mishra, C. Coletti, R. Berger, F. Klappenberger, A. Candini, M. Affronte, C. Zhou, V. de Renzi, U. del Pennino, J. Barth, H. Raeder, A. Narita, X. Feng, and K. Muellen. *Synthesis of graphene nanoribbons by ambient-pressure chemical vapor deposition and device integration.* Journal of the American Chemical Society **138**, 15488 (2016).

[115] S. Masubuchi, M. Ono, K. Yoshida, K. Hirakawa, and T. Machida. *Fabrication of graphene nanoribbon by local anodic oxidation lithography using atomic force microscope.* Applied Physics Letters **94**, 082107 (2009).

[116] B. McCarroll and D. McKee. *The reactivity of graphite surfaces with atoms and molecules of hydrogen, oxygen and nitrogen.* Carbon **9**, 301 (1971).

[117] R. Yang, L. Zhang, Y. Wang, Z. Shi, D. Shi, H. Gao, E. Wang, and G. Zhang. *An anisotropic etching effect in the graphene basal plane.* Advanced Materials **22**, 4014 (2010).

[118] Z. Shi, R. Yang, L. Zhang, Y. Wang, D. Liu, D. Shi, E. Wang, and G. Zhang. *Patterning graphene with zigzag edges by self-aligned anisotropic etching.* Advanced Materials **23**, 3061 (2011).

[119] G. Wang, S. Wu, T. Zhang, P. Chen, X. Lu, S. Wang, D. Wang, K. Watanabe, T. Taniguchi, D. Shi, R. Yang, and G. Zhang. *Patterning monolayer graphene with zigzag edges on hexagonal boron nitride by anisotropic etching.* Applied Physics Letters **109**, 053101 (2016).

[120] G. Diankov, M. Neumann, and D. Goldhaber-Gordon. *Extreme monolayer-selectivity of hydrogen-plasma reactions with graphene.* ACS Nano **7**, 1324 (2013).

[121] B. Ma, S. Ren, P. Wang, C. Jia, and X. Guo. *Precise control of graphene etching by remote hydrogen plasma.* Nano Research 1–6 (2013).

[122] D. Hug, S. Zihlmann, M. K. Rehmann, Y. B. Kalyoncu, T. N. Camenzind, L. Marot, K. Watanabe, T. Taniguchi, and D. M. Zumbühl. *Anisotropic etching of graphite and graphene in a remote hydrogen plasma.* npj 2D Materials and Applications **1**, 21 (2017).

[123] S. Wu, B. Liu, C. Shen, S. Li, X. Huang, X. Lu, P. Chen, G. Wang, D. Wang, M. Liao, J. Zhang, T. Zhang, S. Wang, W. Yang, R. Yang, D. Shi, K. Watanabe, T. Taniguchi, Y. Yao, W. Wang, and G. Zhang. *Magnetotransport Properties of Graphene Nanoribbons with Zigzag Edges.* Phys. Rev. Lett. **120**, 216601 (2018).

[124] A. Davydova, E. Despiau-Pujo, G. Cunge, and D. Graves. *Etching mechanisms of graphene nanoribbons in downstream H2 plasmas: insights from molecular dynamics simulations.* Journal of Physics D: Applied Physics **48**, 195202 (2015).

[125] L. Malard, M. Pimenta, G. Dresselhaus, and M. Dresselhaus. *Raman spectroscopy in graphene.* Physics Reports **473**, 51 (2009).

[126] Y. Y. Wang, Z. H. Ni, T. Yu, Z. X. Shen, H. M. Wang, Y. H. Wu, W. Chen, and A. T. Shen Wee. *Raman studies of monolayer graphene: the substrate effect.* The Journal of Physical Chemistry C **112**, 10637 (2008).

[127] A. C. Ferrari, J. Meyer, V. Scardaci, C. Casiraghi, M. Lazzeri, F. Mauri, S. Piscanec, D. Jiang, K. Novoselov, S. Roth, and A. Geim. *Raman spectrum of graphene and graphene layers.* Physical Review Letters **97**, 187401 (2006).

[128] L. Cançado, A. Reina, J. Kong, and M. Dresselhaus. *Geometrical approach for the study of G' band in the Raman spectrum of monolayer graphene, bilayer graphene, and bulk graphite.* Physical Review B **77**, 245408 (2008).

[129] D. Graf, F. Molitor, K. Ensslin, C. Stampfer, A. Jungen, C. Hierold, and L. Wirtz. *Spatially resolved Raman spectroscopy of single-and few-layer graphene.* Nano Letters **7**, 238 (2007).

[130] C. Casiraghi. *Doping dependence of the Raman peaks intensity of graphene close to the Dirac point.* Physical Review B **80**, 233407 (2009).

[131] A. C. Ferrari. *Raman spectroscopy of graphene and graphite: disorder, electron–phonon coupling, doping and nonadiabatic effects.* Solid state communications **143**, 47 (2007).

[132] L. Cancado, M. Pimenta, B. Neves, M. Dantas, and A. Jorio. *Influence of the atomic structure on the Raman spectra of graphite edges.* Physical Review Letters **93**, 247401 (2004).

[133] Y. You, Z. Ni, T. Yu, and Z. Shen. *Edge chirality determination of graphene by Raman spectroscopy.* Applied Physics Letters **93**, 163112 (2008).

[134] C. Casiraghi, A. Hartschuh, H. Qian, S. Piscanec, C. Georgi, A. Fasoli, K. Novoselov, D. Basko, and A. Ferrari. *Raman spectroscopy of graphene edges.* Nano Letters **9**, 1433 (2009).

[135] K. I. Sasaki, R. Saito, K. Wakabayashi, and T. Enoki. *Identifying the orientation of edge of graphene using G band Raman spectra.* Journal of the Physical Society of Japan **79**, 044603 (2010).

[136] C. Cong, T. Yu, and H. Wang. *Raman study on the G mode of graphene for determination of edge orientation.* ACS Nano **4**, 3175 (2010).

[137] C. P. Scheller, S. Heizmann, K. Bedner, D. Giss, M. Meschke, D. M. Zumbühl, J. D. Zimmerman, and A. C. Gossard. *Silver-epoxy microwave filters and thermalizers for millikelvin experiments.* Applied physics letters **104**, 211106 (2014).

[138] W. Wendler, T. Herrmannsdörfer, S. Rehmann, and F. Pobell. *Electronic and nuclear magnetism in PtFex at milli-, and nanokelvin temperatures.* EPL (Europhysics Letters) **38**, 619 (1997).

[139] T. A. Knuuttila, J. T. Tuoriniemi, K. Lefmann, K. Juntunen, F. Rasmussen, and K. Nummila. *Polarized nuclei in normal and superconducting rhodium.* Journal of Low Temperature Physics **123**, 65 (2001).

[140] G. Pickett. *Microkelvin physics.* Reports on Progress in Physics **51**, 1295 (1988).

[141] R. C. Richardson. *Experimental techniques in condensed matter physics at low temperatures* (CRC Press, 2018).

[142] J. Ekin. *Experimental techniques for low-temperature measurements: cryostat design, material properties and superconductor critical-current testing* (Oxford university press, 2006).

[143] G. Ventura and L. Risegari. *The art of cryogenics: low-temperature experimental techniques* (Elsevier, 2010).

[144] O. V. Lounasmaa. *Experimental principles and methods below 1K* (Academic Press, 1974).

[145] N. S. Lawson. *A simple heat switch for use at millikelvin temperatures.* Cryogenics **22**, 667 (1982).

[146] A. Zorin. *The thermocoax cable as the microwave frequency filter for single electron circuits.* Review of Scientific Instruments **66**, 4296 (1995).

[147] G. Batey, A. Casey, M. Cuthbert, A. Matthews, J. Saunders, and A. Shibahara. *A microkelvin cryogen-free experimental platform with integrated noise thermometry.* New Journal of Physics **15**, 113034 (2013).

[148] A. Casey, F. Arnold, L. V. Levitin, C. P. Lusher, J. Nyéki, J. Saunders, A. Shibahara, H. van der Vliet, B. Yager, D. Drung, T. Schurig, G. Batey, C. MN, and M. AJ. *Current sensing noise thermometry: a fast practical solution to low temperature measurement.* Journal of Low Temperature Physics **175**, 764 (2014).

[149] I. Todoshchenko, J.-P. Kaikkonen, R. Blaauwgeers, P. J. Hakonen, and A. Savin. *Dry demagnetization cryostat for sub-millikelvin helium experiments: Refrigeration and thermometry.* Review of Scientific Instruments **85**, 085106 (2014).

[150] L. Casparis, M. Meschke, D. Maradan, A. Clark, C. Scheller, K. Schwarzwälder, J. P. Pekola, and D. Zumbühl. *Metallic Coulomb blockade thermometry down to 10 mK and below.* Review of Scientific instruments **83**, 083903 (2012).

[151] D. Bradley, A. Guénault, D. Gunnarsson, R. Haley, S. Holt, A. Jones, Y. A. Pashkin, J. Penttilä, J. Prance, M. Prunnila, and L. Roschier. *On-chip magnetic cooling of a nanoelectronic device.* Scientific Reports **7**, 45566 (2017).

[152] A. Feshchenko. *Electron thermometry, refrigeration and heat transport in nanostructures at sub-kelvin temperatures.* Ph.D. thesis, Aalto University (2017).

[153] D. I. Bradley, R. E. George, D. Gunnarsson, R. P. Haley, H. Heikkinen, Y. A. Pashkin, J. Penttilä, J. R. Prance, M. Prunnila, L. Roschier, and M. Sarsby. *Nanoelectronic primary thermometry below 4 mK.* Nature Communications **7**, 10455 (2016).

[154] B. Trauzettel, D. V. Bulaev, D. Loss, and G. Burkard. *Spin qubits in graphene quantum dots.* Nature Physics **3**, 192 (2007).

[155] M. Pan, E. C. Girão, X. Jia, S. Bhaviripudi, Q. Li, J. Kong, V. Meunier, and M. S. Dresselhaus. *Topographic and Spectroscopic Characterization of Electronic Edge States in CVD Grown Graphene Nanoribbons.* Nano Letters **12**, 1928 (2012).

[156] X. Zhang, O. V. Yazyev, J. Feng, L. Xie, C. Tao, Y.-C. Chen, L. Jiao, Z. Pedramrazi, A. Zettl, S. G. Louie, H. Dai, and M. F. Crommie. *Experimentally Engineering the Edge Termination of Graphene Nanoribbons.* ACS Nano **7**, 198 (2013).

[157] G. Z. Magda, X. Jin, I. Hagymási, P. Vancsó, Z. Osváth, P. Nemes-Incze, C. Hwang, L. P. Biró, and L. Tapasztó. *Room-temperature magnetic order on zigzag edges of narrow graphene nanoribbons.* Nature **514**, 608 (2014).

[158] M. Han, B. Özyilmaz, Y. Zhang, and P. Kim. *Energy Band-Gap Engineering of Graphene Nanoribbons.* Physical Review Letters **98**, 206805 (2007).

[159] J. B. Oostinga, B. Sacepe, M. F. Craciun, and A. F. Morpurgo. *Magnetotransport through graphene nanoribbons.* Physical Review B **81**, 193408 (2010).

[160] X. Liu, J. Oostinga, A. Morpurgo, and L. Vandersypen. *Electrostatic confinement of electrons in graphene nanoribbons.* Physical Review B **80**, 121407 (2009).

[161] F. Molitor, C. Stampfer, J. GÃ¼ttinger, A. Jacobsen, T. Ihn, and K. Ensslin. *Energy and transport gaps in etched graphene nanoribbons.* Semiconductor Science and Technology **25**, 034002 (2010).

[162] F. Oberhuber, S. Blien, S. Heydrich, T. Yaghobian, Fatemeh Korn, C. Schüller, C. Strunk, D. Weiss, and J. Eroms. *Weak localization and Raman study of anisotropically etched graphene antidots.* Applied Physics Letters **103**, 143111 (2013).

[163] F. Oberhuber, S. Blien, F. Schupp, D. Weiss, and J. Eroms. *Anisotropic etching of graphene in inert and oxygen atmospheres.* Physica Status Solidi A **214**, 1600459 (2017).

[164] L. Xie, L. Jiao, and H. Dai. *Selective Etching of Graphene Edges by Hydrogen Plasma.* Journal of the American Chemical Society **132**, 14751 (2010).

[165] NGS Naturgraphit GmbH.

[166] R. K. Janev, D. Reiter, and U. Samm. *Collision Processes in Low-Temperature Hydrogen Plasmas* (Forschungszentrum Juelich GmbH, 2003).

[167] G. Dixon-Lewis, M. M. Sutton, and A. Williams. *The kinetics of hydrogen atom recombination.* Discussions of the Faraday Society **33**, 205 (1962).

[168] R. K. Grubbs and S. M. George. *Attenuation of hydrogen radicals traveling under flowing gas conditions through tubes of different materials.* Journal of Vacuum Science & Technology A: Vacuum, Surfaces, and Films **24**, 486 (2006).

[169] K. E. Shuler and K. J. Laidler. *The Kinetics of Heterogeneous Atom and Radical Reactions. I. The Recombination of Hydrogen Atoms on Surfaces.* The Journal of Chemical Physics **17**, 1212 (1949).

[170] Suprasil 310, Heraeus Quarzglas GmbH.

[171] Y. Zhang, V. W. Brar, C. Girit, A. Zettl, and M. F. Crommie. *Origin of spatial charge inhomogeneity in graphene.* Nature Physics **5**, 722 (2009).

[172] R. Decker, Y. Wang, V. W. Brar, W. Regan, H.-Z. Tsai, Q. Wu, W. Gannett, A. Zettl, and M. F. Crommie. *Local Electronic Properties of Graphene on a BN Substrate via Scanning Tunneling Microscopy.* Nano Letters **11**, 2291 (2011).

[173] J. Xue, J. Sanchez-Yamagishi, D. Bulmash, P. Jacquod, A. Deshpande, K. Watanabe, T. Taniguchi, P. Jarillo-Herrero, and B. J. LeRoy. *Scanning tunnelling microscopy and spectroscopy of ultra-flat graphene on hexagonal boron nitride.* Nature Materials **10**, 282 (2011).

[174] Y. C. Kim and M. Boudart. Langmuir **7**, 2999 (1991).

[175] T. Taniguchi and K. Watanabe. *Synthesis of high-purity boron nitride single crystals under high pressure by using Ba-BN solvent.* Journal of Crystal Growth **303**, 525 (2007).

[176] D. C. Elias, R. R. Nair, T. M. G. Mohiuddin, S. V. Morozov, P. Blake, M. P. Halsall, A. C. Ferrari, D. W. Boukhvalov, M. I. Katsnelson, and A. K. Geim. *Control of graphene's properties by reversible hydrogenation: evidence for graphane.* Science **323**, 610 (2009).

[177] J. Sofo, A. Chaudhari, and G. Barber. *Graphane: A two-dimensional hydrocarbon.* Phys. Rev. B **75**, 153401 (2007).

[178] B. Eren, D. Hug, L. Marot, R. Pawlak, M. Kisiel, R. Steiner, D. M. Zumbühl, and E. Meyer. *Pure hydrogen low-temperature plasma exposure of HOPG and graphene: Graphane formation?* Beilstein Journal of Nanotechnology **3**, 852 (2012).

[179] C. Woods, F. Withers, M. Zhu, Y. Cao, G. Yu, A. Kozikov, M. B. Shalom, S. Morozov, M. van Wijk, A. Fasolino, M. Katsnelson, K. Watanabe, T. Taniguchi, A. Geim, M. Novoselov, and N. KS. *Macroscopic self-reorientation of interacting two-dimensional crystals.* Nature Communications **7** (2016).

[180] D. Wang, G. Chen, C. Li, M. Cheng, W. Yang, S. Wu, G. Xie, J. Zhang, J. Zhao, X. Lu, P. Chen, G. Wang, J. Meng, J. Tang, R. Yang, C. He, D. Liu, D. Shi, K. Watanabe, T. Taniguchi, J. Feng, Y. Zhang, and G. Zhang. *Thermally Induced Graphene Rotation on Hexagonal Boron Nitride.* Phys. Rev. Lett. **116**, 126101 (2016).

[181] L. Zhang, D. A. Pejaković, B. Geng, and J. Marschall. *Surface modification of highly oriented pyrolytic graphite by reaction with atomic nitrogen at high temperatures.* Applied Surface Science **257**, 5647 (2011).

[182] M. Moisan and Z. Zakrzewski. *Plasma sources based on the propagation of electromagnetic surface waves.* Journal of Physics D: Applied Physics **24**, 1025 (1991).

[183] K. Sancier and H. Wise. *Diffusion coefficient measurements for gas mixture of atomic and molecular hydrogen* (Technical Report from Purdue Unic Lafayette in Project Squid Headquarters, 1969).

[184] S. Weissman and M. EA. *Estimation of the mutual diffusion coefficient of hydrogen atoms and molecules.* The Journal of Chemical Physics **36**, 794 (1962).

[185] R. Geick, C. Perry, and G. Rupprecht. *Normal modes in hexagonal boron nitride.* Physical Review **146**, 543 (1966).

[186] M. Begliarbekov, K. I. Sasaki, O. Sul, E.-H. Yang, and S. Strauf. *Optical control of edge chirality in graphene.* Nano Letters **11**, 4874 (2011).

[187] X. Zhang, O. V. Yazyev, J. Feng, L. Xie, C. Tao, Y.-C. Chen, L. Jiao, Z. Pedramrazi, A. Zettl, S. G. Louie, H. Dai, and M. Crommie. *Experimentally engineering the edge termination of graphene nanoribbons.* ACS Nano **7**, 198 (2012).

[188] D. Basko. *Boundary problems for Dirac electrons and edge-assisted Raman scattering in graphene.* Physical Review B **79**, 205428 (2009).

[189] D. S. Wastl, A. J. Weymouth, and F. J. Giessibl. *Optimizing atomic resolution of force microscopy in ambient conditions.* Physical Review B **87**, 245415 (2013).

[190] A. K. Gupta, T. J. Russin, H. R. Gutiérrez, and P. C. Eklund. *Probing graphene edges via Raman scattering.* ACS Nano **3**, 45 (2008).

[191] N. J. Couto, D. Costanzo, S. Engels, D.-K. Ki, K. Watanabe, T. Taniguchi, C. Stampfer, F. Guinea, and A. F. Morpurgo. *Random strain fluctuations as dominant disorder source for high-quality on-substrate graphene devices.* Physical Review X **4**, 041019 (2014).

[192] D. Bischoff, J. Güttinger, S. Dröscher, T. Ihn, K. Ensslin, and C. Stampfer. *Raman spectroscopy on etched graphene nanoribbons.* Journal of Applied Physics **109**, 073710 (2011).

[193] Y. N. Xu, D. Zhan, L. Liu, H. Suo, Z. H. Ni, T. T. Nguyen, C. Zhao, and Z. X. Shen. *Thermal Dynamics of Graphene Edges Investigated by Polarized Raman Spectroscopy.* ACS Nano **5**, 147 (2011).

[194] P. Koskinen, S. Malola, and H. Häkkinen. *Self-Passivating Edge Reconstructions of Graphene.* Phys. Rev. Lett. **101**, 115502 (2008).

[195] L. Campos, A. Young, K. Surakitbovorn, K. Watanabe, T. Taniguchi, and P. Jarillo-Herrero. *Quantum and classical confinement of resonant states in a trilayer graphene Fabry-Pérot interferometer.* Nature Communications **3**, 1239 (2012).

[196] C. Handschin, P. Makk, P. Rickhaus, R. Maurand, K. Watanabe, T. Taniguchi, K. Richter, M.-H. Liu, and C. Schoönenberger. *Giant valley-isospin conductance oscillations in ballistic graphene.* Nano Letters **17**, 5389 (2017).

[197] J. R. Wallbank, M. Mucha-Kruczyński, X. Chen, and V. I. Fal'ko. *Moiré superlattice effects in graphene/boron-nitride van der Waals heterostructures.* Annalen der Physik **527**, 359 (2015).

[198] S. Morita, F. Giessibl, E. Meyer, and R. Wiesendanger. *Noncontact atomic force microscopy* (Springer, 2015).

[199] K. He, A. W. Robertson, Y. Fan, C. S. Allen, Y.-C. Lin, K. Suenaga, A. I. Kirkland, and J. H. Warner. *Temperature Dependence of the Reconstruction of Zigzag Edges in Graphene.* ACS Nano **9**, 4786 (2015).

[200] D. Maradan. *Magnetic refrigeration for nanoelectronics on a cryogen-free platform.* Ph.D. thesis, University of Basel (2015).

[201] M. Palma. *Magnetic cooling and on-chip thermometry for nanoelectronics below 10 mK.* Ph.D. thesis, University of Basel (2017).

[202] J. Engert, J. Beyer, D. Drung, A. Kirste, and M. Peters. *A noise thermometer for practical thermometry at low temperatures.* International Journal of Thermophysics **28**, 1800 (2007).

[203] J. Engert, D. Heyer, J. Beyer, and H. Barthelmess. *Noise thermometry at low temperatures: MFFT measurements between 1.6 K and 1 mK.* In *Journal of Physics: Conference Series*, volume 400, 052003 (IOP Publishing, 2012).

[204] J. Beyer, D. Drung, A. Kirste, J. Engert, A. Netsch, A. Fleischmann, and C. Enss. *A magnetic-field-fluctuation thermometer for the mK range based on SQUID-magnetometry.* IEEE Transactions on Applied Superconductivity **17**, 760 (2007).

[205] D. Rothfuß, A. Reiser, A. Fleischmann, and C. Enss. *Noise thermometry at ultra low temperatures.* Applied Physics Letters **103**, 052605 (2013).

[206] M. Palma, D. Maradan, L. Casparis, T.-M. Liu, F. N. Froning, and D. M. Zumbühl. *Magnetic cooling for microkelvin nanoelectronics on a cryofree platform.* Review of Scientific Instruments **88**, 043902 (2017).

[207] A. Feshchenko, M. Meschke, D. Gunnarsson, M. Prunnila, L. Roschier, J. Penttilń, and J. Pekola. *Primary thermometry in the intermediate Coulomb blockade regime.* Journal of Low Temperature Physics **173**, 36 (2013).

[208] N. Yurttagul, M. Sarsby, and A. Geresdi. *Indium as a high cooling power nuclear refrigerator for quantum electronics.* arXiv:1811.03034v1 .

[209] K. Novoselov, A. Mishchenko, A. Carvalho, and A. C. Neto. *2D materials and van der Waals heterostructures.* Science **353**, aac9439 (2016).

[210] D. Bischoff, M. Eich, O. Zilberberg, C. Roessler, T. Ihn, and K. Ensslin. *Measurement back-action in stacked graphene quantum dots.* Nano Letters **15**, 6003 (2015).

[211] R. Willett, C. Nayak, K. Shtengel, L. Pfeiffer, and K. West. *Magnetic-field-tuned aharonov-bohm oscillations and evidence for non-abelian anyons at $\nu=5/2$.* Physical Review Letters **111**, 186401 (2013).

[212] R. L. Willett, L. N. Pfeiffer, and K. West. *Measurement of filling factor 5/2 quasiparticle interference with observation of charge e/4 and e/2 period oscillations.* Proceedings of the National Academy of Sciences **106**, 8853 (2009).

[213] R. L. Willett, L. N. Pfeiffer, and K. West. *Alternation and interchange of e/4 and e/2 period interference oscillations consistent with filling factor 5/2 non-Abelian quasiparticles.* Physical Review B **82**, 205301 (2010).

[214] J. Klinovaja and D. Loss. *Integer and fractional quantum Hall effect in a strip of stripes*. The European Physical Journal B **87**, 171 (2014).

[215] J. Klinovaja, Y. Tserkovnyak, and D. Loss. *Integer and fractional quantum anomalous Hall effect in a strip of stripes model*. Physical Review B **91**, 085426 (2015).

[216] Bluefors Cryogenics Oy, Finland.

[217] R. Stanway. *Vibration Control of Active Structures - An Introduction* (2004).

List of Figures

Curriculum Vitae

Yemliha Bilal Kalyoncu, from Istanbul, Turkey

25 March 1988	born in Istanbul, Turkey
1994 - 2002	Sarıyer Ilköğretim Okulu
2002 - 2006	Beyoğlu Anadolu High School
2006 - 2014	BSc and MSc in Physics at Boğaziçi University
2014 - 2018	PhD at University of Basel

Publications

- Y.B. Kalyoncu & Ö. Özatay. *A Three Dimensional Opto-magnetic Data Storage System and Method.* US Patent US9812202 B2. TPE, TR 2012 12865. TPE, TR 2012 15536.

- D. Hug, S. Zihlmann, M.K. Rehmann, Y.B. Kalyoncu, T.N. Camenzind, L. Marot, K. Watanabe, T. Taniguchi & D.M. Zumbühl. *Anisotropic Etching of Graphite and Graphene in a Remote Hydrogen Plasma.* npj 2D Materials and Applications **1**, 21 (2017)

- Y.B. Kalyoncu, M.K. Rehmann, M. Kisiel, N. Pascher, F.J. Giessibl, F. Müller, K. Watanabe, T. Taniguchi, E. Meyer, M.H. Liu & D.M. Zumbühl. *Characterization of Graphene Edges Defined with Hydrogen Plasma.* Manuscript in preparation